Photosynthesis of nanomaterials with optical resonances

Evgenia Kontoleta

Photosynthesis of nanomaterials with optical resonances

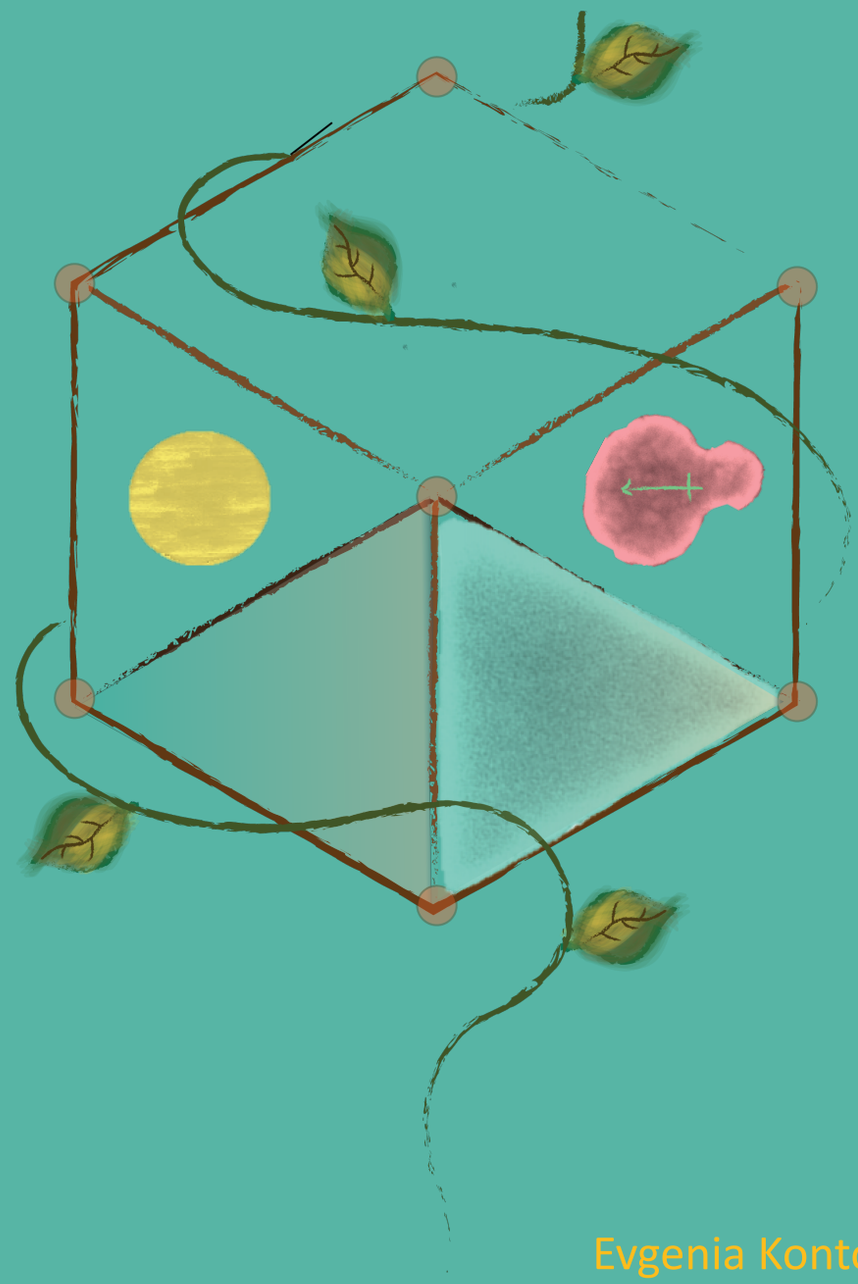

Evgenia Kontoleta

Photosynthesis of nanomaterials with optical resonances

Cover image: Artistic impression of a metal dipole concentrating light to synthesize new crystals, inspired by Tzanetos Kritselis.

Ph.D. Thesis, University of Amsterdam, December 2019

Photosynthesis of nanomaterials with optical resonances

Evgenia Kontoleta

ISBN: 978-94-92323-32-3

A digital version of this thesis can be downloaded from http://www.amolf.nl.

Photosynthesis of nanomaterials with optical resonances

Academisch Proefschrift

ter verkrijging van de graad van doctor
aan de Universiteit van Amsterdam
op gezag van de Rector Magnificus
prof. dr. ir. K. I. J. Maex
ten overstaan van een door het college voor promoties ingestelde commissie,
in het openbaar te verdedigen in de Agnietenkapel
op donderdag 5 december 2019, te 10:00 uur

door

Evgenia Kontoleta

geboren te Amarousio

Promotiecommissie

Promotor:	prof. dr. E. C. Garnett	Universiteit van Amsterdam
Copromotor:	prof. dr. A. Polman	Universiteit van Amsterdam
Overige leden:	prof. dr. A. F. Koenderink	Universiteit van Amsterdam
	prof. dr. J. N. H. Reek	Universiteit van Amsterdam
	prof. dr. P. C. M. Planken	Universiteit van Amsterdam
	prof. dr. W. A. Smith	TU Delft
	dr. A. Bieberle-Hütter	DIFFER Institute

Faculteit der Natuurwetenschappen, Wiskunde en Informatica.

The work described in this thesis was performed at AMOLF,
Science Park 104, 1098 XG Amsterdam, The Netherlands.

This work is part of the Dutch Research Council (NWO).

Ἀμαθέστερον πὼς εἰπὲ καὶ σαφέστερον.

Say something a little less educated
and more comprehensible.

Αριστοφάνης
Aristophanes

Contents

1

Introduction

We all witness light-matter interactions everyday in the most common things around us, such as the blue color of the sky. Rayleigh described how light interacts with particles that are small compared to the wavelength of light, developing a theory that ultimately explained the color of the sky.[1] Later, Gustav Mie solved Maxwell's equations for spherical particles with wavelength-scale diameters, thereby explaining how water droplets interact with electromagnetic radiation and form clouds.[2] Since then, many researchers have tried to control this interaction by making nanostructured materials with dimensions comparable to the wavelength of light. This has led to the field of nanophotonics, opening up new possibilities for a variety of applications such as optical communication, medical science, sensing and energy harvesting. [3, 4]

A tremendous amount of metal nanostructures made from different materials, with different shapes and sizes have already been synthesized with many different techniques such as electron-beam, nanosphere and nanoimprint lithography and colloidal synthesis.[5–8] While all these fabrication methods of nanomaterials have been extensively used, most of them are either expensive, time-consuming or cannot reach the resolution needed for the design of very small structures. Colloidal synthesis constitutes an exception since it is a very inexpensive method, with possibilities for the generation of nearly any shape or size of nanostructure.[9–13] Unfortunately though, colloidal synthesis lacks full control over the design of more hierarchical nanomaterials.[14] Light itself can be used as a tool for the synthesis of nanostructures through light-induced chemical reactions and provide new pathways of control over this design.

This thesis deals with how optical resonances, derived from light-matter interactions, can be used to drive localized chemistry for the synthesis of complicated nanomaterials. Such light driven synthesis is an artificial analogue of natural photosynthesis, where

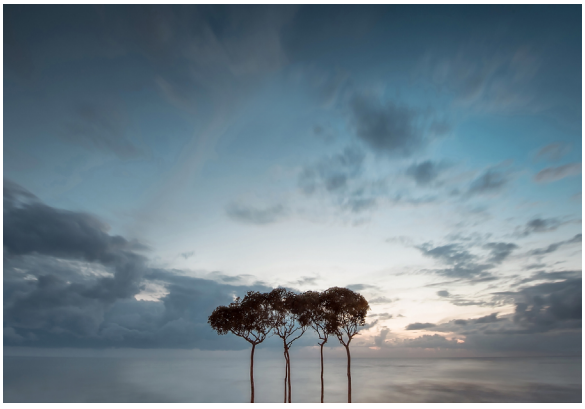

Figure 1.1. An example of Rayleigh and Mie scattering in nature, where the sky meets the sea in Zacharo, Ilias, Greece. Photo taken by Manousopoulos P.

plants produce a wide variety of natural products using sunlight. As in natural photosynthesis, our final goal is to create a custom factory that uses light to spontaneously form a wide variety of useful products.[15] Although nature more often uses chemical variables to create the hierarchy and structure, this thesis is more focused on understanding the role of the underlying nanostructures, their optical resonances and how light itself can be used as a reactant. It therefore begins with an explanation of the different types of resonances available in semiconducting and metallic nanomaterials, followed by how these resonances can lead to charge generation, ultimately driving nano-localized chemistry.

1.1 Optical resonances in nanostructures

An interesting aspect of light-matter interactions at the nanoscale is the appearance of optical resonances. An optical resonance occurs when light constructively interferes in a cavity (or inside a nanostructure) or when light stimulates and couples to electron charge oscillations on the surface of a nanostructure.[16] Optical resonances lead to storage of high amounts of optical energy in specific frequencies where strong absorption or scattering takes place. The resonant frequency depends mostly on the nature of the optical resonator (i.e. nanostructure's geometry and refractive index) and the refractive index of the surrounding medium. Mie's analytical solution to Maxwell's equations is the most commonly used mathematical description of the interaction of a spherical nanoparticle or an infinite cylinder, with a plane electromagnetic wave.[2] Mie's theory is valid for both dielectric and metal nanostructures, whose dimensions are comparable to that of the light's wavelength. Even though the description of optical resonances in metals and semiconductors can be achieved by the same theory, the origin of optical

resonances in metals and dielectrics is quite different, as discussed below.

1.1.1 Metals

Optical resonances in metal nanoparticles originate from their high density of free electrons, which can oscillate resonantly with an incident electric field. The response of the electron cloud to an external electric field can be described by the Drude model, where electrons follow Newton's law and act as an oscillating mass around the fixed positive core (Figure 1.2). The external electric field causes the displacement of the electron cloud from the positively charged core, while a restoring force (Coulomb force) drives back the negatively charged electron cloud to the electron deficient region of the structure causing the oscillation of the free electrons. These collective oscillations of the free electrons in metal nanostructures are called plasmons and an optical resonance (surface plasmon resonance, SPR) occurs when the plasmon natural frequency is equal to the frequency of the incident light.[17, 18] According to the Drude model, the permittivity of metal nanoparticles becomes negative for incident light frequencies higher than the SPR frequency. A negative value of permittivity means that the material does not allow electromagnetic wave propagation in its volume resulting in confinement of the electric field on the metal/dielectric interface. The localization of charges at the metal/dielectric interface arising from the surface plasmons can interact with the propagating electromagnetic field in the vicinity of the nanostructure and energy transfer from light to plasmons can take place.[19–21] Once this transfer has occurred, the plasmons can either decay by coupling back to the light field (radiation, also known as scattering) or by excitation of electrons into higher excited states (absorption).[22] The areas where this "focusing" of the electric near field of plasmonic nanoparticles occurs are called hot-spots, where the electric field enhancement can reach several order of magnitude in subwavelength volumes.

The SPR frequency and the intensity and spatial distribution of the hot-spots strongly depend on the charge distribution inside the metal nanostructure. The magnitude of the charge separation inside a nanosphere in response to an electric field, or in other words the ease with which it forms dipoles, is called polarizability. According to Mie theory, polarizability is affected by the refractive index of the metal and the surrounding dielectric medium and the geometry of the nanostructure. In nanoparticles with sizes in the subwavelength regime, the polarizability increases with an increase in the nanoparticle's size leading to a lower frequency of the electron cloud oscillations. The direct impact of the decrease in the plasmon frequency, is the shift of the SPR to longer wavelengths (redshift).[23] The refractive index of the surrounding medium of the nanoparticle also changes the interaction of the plasmons with the incident light, since this interaction is mainly happening at the meal/dielectric interface. As the refractive index of the dielectric medium increases, the frequency of the plasmons decreases, due to the increasing difficulty of their propagation, and the plasmons resonate with the incident electric field at smaller spectral frequencies (redshifted SPR). [24]

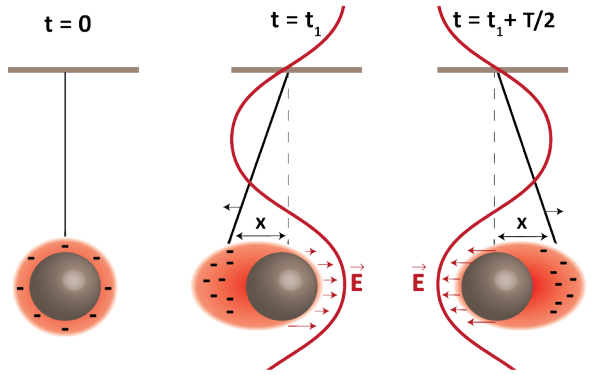

Figure 1.2. Drude model schematic representation. In a spherical metal nanosphere the electron cloud surrounds the positive nuclei of the metal atoms (t = 0). At time $t = t_1$, when the nanosphere starts interacting with an incident electromagnetic wave, the electron cloud starts oscillating and is displaced (x the elctron displacement) compared to the positive nuclei. After half a wavelength period from $t = t_1$ ($t = t_1 + T/2$), the electron cloud is displaced towards the opposite direction than $t = t_1$.

A change in the geometry of the nanostructure can also induce the excitation of more than one optical mode.[25] For instance, two SPR peaks appear from the excitation of a metal nanorod, related to polarization of the electric charges along its long (longitudinal mode) and short axis (transverse mode). It has been reported that the longitudinal mode of metal nanorods is more sensitive to a change of the aspect ratio of the nanostructure, than the transverse mode, and can be tuned from the visible to NIR. Hybridization of resonant modes in a nanoparticle assembly can also occur resulting in the accesibility of more than one resonant mode. For instance, two closely spaced oscillating systems, with similar resonant energies, can interact with each other and electromagnetic energy exchange takes place through mode coupling.[26, 27] Spatial and spectral overlap of the nanoparticles' individual elementary modes is necessary for the occurrence of mode hybridization. As a result, very strong electric field enhancement and charge accumulation (hot-spot) can be developed in the nanogap between the two nanostructures. Spectral changes of the resonant mode of each nanoparticle rely on the alteration of the restoring force of the electron cloud oscillation towards each direction, which can be enhanced or decreased due to its interaction with the oscillating electron cloud of the nearby nanoparticle. An increase (decrease) in the restoring force corresponds to a increase (decrease) in the resonant frequency, meaning a blueshifted (redshifted) resonance.

When the size of the nanostructure increases and becomes substantial compared to the wavelength, higher order modes can be supported by the nanostructure, which appear in

higher frequencies than the fundamental one (dipolar mode).[28, 29] The origin of these higher order modes comes from depolarization of the electrons inside the nanomaterial. The introduction of sharp features in a nanostructure, such as the case of nanocubes and nanotriangles, can also change the polarization of the electrons inside the nanomaterial and result in excitation of multipolar modes in the visible spectrum and extreme light confinement.[30–33]

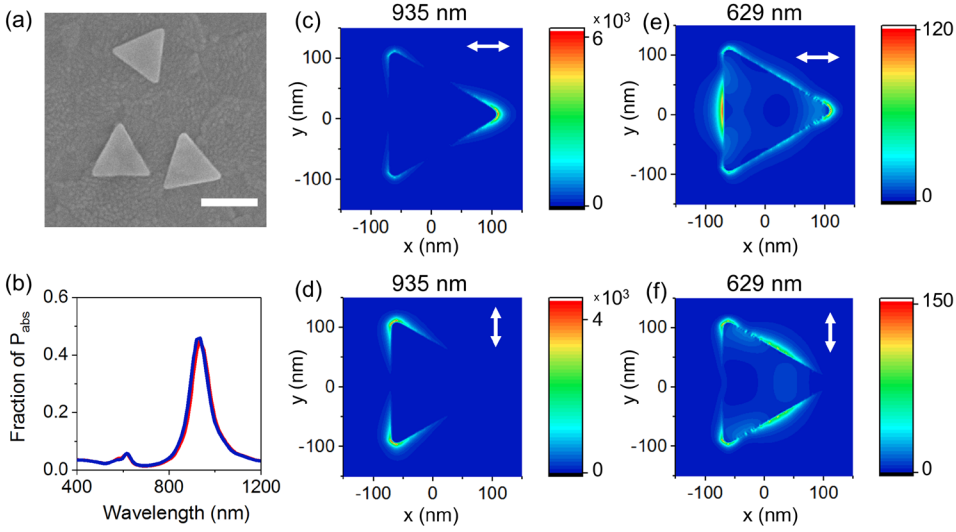

Figure 1.3. Tunable hot-spots in plasmonic nanostructures a) Scanning microscope image of Au nanotriangles with 200 nm edge and 8 nm thickness made with colloidal chemistry. Scale bar is 200 nm. b) Fraction of absorbed power retrieved from FDTD simulations for two different polarizations (in air), the electric field distribution ($|E^2| \,/\, |E_0^2|$) of which is depicted in c), d), e) and f) for the 2 different SPR wavelengths (935 and 629 nm). The electric field monitor is positioned at a 4 nm height (middle of the nanostructure) and the white arrows show the polarization of the incident electric field with intensity $|E_0^2|$.

Hot-carrier generation in metal nanostructures

After the excitation of plasmons in a metal nanostructure, the presence of imperfections in the structure, surface states or lattice vibrations lead to the dephasing of the collective oscillations of electrons. This dephasing can occur either radiatively (light scattering), with the emission of a photon at the same frequency as the excitation wavelength, or non-radiatively (Figure 1.4). The non-radiative decay of the plasmons mainly takes place through Landau damping, where energy quanta from the plasmons are re-

moved and transferred in the form of kinetic energy to conduction band electrons, exciting them to unoccupied energy states above the Fermi level. [34, 35] The generation of highly energetic charges with Landau damping occurs the first 1 - 100 fs after the plasmon excitation and a non-thermal distribution of electrons is created above the Fermi level of the metal. During the next few hundreds of femtoseconds (100 fs - 1 ps), the initial non-thermal distribution changes to a Fermi-Dirac like electron distribution via electron-electron scattering, where redistribution of energy takes place between higher and lower energy electrons. The Fermi-Dirac distribution consists of electrons with a temperature far above the lattice temperature. The electrons both in the non-thermal and the Fermi-Dirac distributions are called "hot" due to their high energy and not necessarily due to their high temperature (Fermi-Dirac distribution case). Additionally, energy is transferred from the electrons to the lattice of the nanostructure via electron-phonon interactions (1 - 10 ps) leading to an increase of the lattice's temperature and resulting in an equilibrium among the excited electrons. Finally, phonon-phonon interactions result in heat dissipation in the surroundings (100 ps - 10 ns). [20, 22, 36, 37]

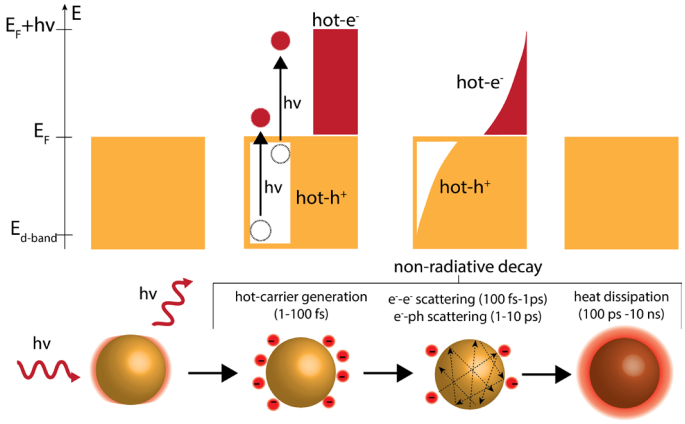

Figure 1.4. Plasmon decay. Bottom row: Schematic of plasmon decay in metal nanoparticles. Plasmons can decay either radiatevely, with the emission of a photon, or non-radiatively. The non-radiative emission takes place through Landau damping and hot-carriers are generated (1-100 fs), thermalization of carriers occurs through electron-electron (100 fs - 1 ps) and electron-phonon (1 - 10 ps) scattering creating a Fermi dirac distribution, to ultimately return to the equilibrium with heat dissipation to the surroundings (100 ps - 10 ns). Top row: The corresponding charge population as a function of their energy with respect to the Fermi level of the metal for every stage of the decay process, starting from the equilibrium.[34]

The electronic structure of metals allows mainly two transitions of electrons. The transitions from d-bands to the sp-band, called interband, and transitions within the

sp-band, called intraband.[38] In metal and specifically noble metal nanomaterials, d-bands (i.e. energy states which belong to atoms from the d-orbitals) are located 2 - 4 eV below the Fermi level (E_{d-band}, Figure 1.4).[39, 40] Transitions within the d-bands are not allowed since all of them are already filled with electrons. Electron excitation though within the sp-band is possible since it is only half-filled with electrons up to the metal's Fermi level (conduction band). As a result, depending on the photon energy absorbed by the metal nanoparticle and the position of the electronic states, different excitations either interband or intraband can occur. The maximum energy an electron can have according to the allowed transitions is equal to $Ef + hv$ (Figure 1.4), when excitation of electrons from the conduction band takes place (intraband). In gold the d-band lies 2.4 eV below the Fermi level, while in silver the energy needed for interband excitations is 3.7 eV. As a result, to excite electrons from the d-bands in silver a photon of at least 3.7 eV is needed, which corresponds to a wavelength of around 335 nm, so UV light excitation is necessary. In gold, interband excitations fall in the visible spectrum (below 517 nm), which explains the broadband absorption of Au nanostructures in this wavelength range. Electrons excited from the d-bands are not considered as hot because they reach energies close to that of the Fermi level (5.5 eV for gold) and as a result they are not highly-energetic ($E_{d-band} + hv \approx E_f$). Consequently, gold is considered as a material with a higher population of energetic holes than electrons under white light illumination, while silver has more uniform generation of both highly energetic holes and electrons.[41–43] Nevertheless, in this thesis we are mostly focusing on gold nanostructures, due to their high stability over oxidation, which is important for driving chemical reactions in the presence of an aqueous electrolyte. The investigated gold nanostructures though are excited far from their interband transitions ($E_{ph} < 2.4eV$) to ensure the predominant generation of hot-carriers.

Hot-carriers are mostly generated at the hot-spots of plasmonic nanostructures since these are the areas with the strongest field enhancement.[42] Nanostructures with sharp features or assemblies of nanoparticles exhibit the strongest field enhancements through the formation of hot-spots originating from the coupling of plasmon modes or the existence of multipolar modes. As a result, nanotriangles and nanocubes with sharp corners, bow-tie antennas and island-like nanoparticle assemblies are excellent candidates for high generation rates of hot-carriers.[36, 39, 44–46] The excitation wavelength strongly affects the generation rate of hot-carriers, since the amount of hot-carriers follows the absorption spectrum of the nanostructure, where the highest amount of hot-carriers is generated at the SPR. The electronic structure of the material in combination with the excitation wavelength can also affect the generation rates of hot-carriers as well as the hot-carrier energy distribution. In plasmonic nanostructures excited with photon energies where only intraband transitions take place, hot-electrons and hot-holes with continuous energy distribution (from the Fermi level up to the photon energy) are produced and this distribution is not so sensitive to the type of material used. On the contrary, when the excitation wavelength is within the interband spectral range, then the profile of hot-electron and hot-hole distributions is highly dependent on the material and its electronic

structure. According to literature, materials such as gold and copper generate a high population of highly energetic holes but a lower population of highly energetic electrons in the interband spectral range. In silver and aluminum though, there is no difference between the energy distribution profiles of hot-electrons and hot-holes.[40, 47, 48] The size of metal nanoparticles also affects the hot-carrier generation rate and profile (in the interband regime). As the size increases, the homogeneous unoccupied energy state profile of the nanoparticle results in a higher total amount of hot-carriers but with lower energy, compared to smaller sizes, due to the higher amount of available transitions.[43, 49, 50]

Hot-carrier extraction

Extraction of hot-carriers from a metal nanostructure usually takes place through a semiconductor (e.g. a metal oxide) placed in the close proximity of the metal.[51–53] The presence of the semiconductor introduces new decay paths for the hot-carriers delaying their thermalization. Instead of the fast thermalization of hot-electrons through electron-electron or electron-phonon scattering, hot-electrons (or hot-holes) after their photogeneration can be transferred to energy levels offered by the semiconductor. Band energy levels in semiconductor materials are not continuous as in the case of metals and as a result two main bands appear: the conduction and the valence band. The former consists of unoccupied energy states and the latter is fully occupied by electrons. As a result, the conduction band of the semiconductor can host hot-electrons and the valence band hot-holes. This transfer of hot-carriers to a semiconductor assists their separation from the metal structure and as a result avoids thermalization. As soon as hot carriers are injected to a semiconductor, they are converted to majority carriers, which have much longer lifetimes (e.g. > 1 μs in anatase TiO_2).[51, 54] In this thesis we are dealing with only hot-electron transfer in the conduction band of a nearby semiconductor at excitation energies lower than the bandgap energy of the semiconductor. Excitation above the bandgap of the semiconductor would result in recombination of hot-electrons injected in its conduction band with photogenerated holes from the excitation of the semiconductor.

A semiconductor can facilitate hot-electron extraction from either the non-thermal distribution (before electron-electron scattering starts) or the thermal-distribution (before electron-phonon interaction).[55] The type of hot-electrons extracted depends on the intrinsic characteristics of the metal, such as the hot-electron mean free path (the distance electrons can travel before they collide with other electrons) and the electron-electron scattering timescales.[43] The choice of the semiconductor is also very crucial to achieve enhanced hot-electron extraction rates.[56–58] The energy of the conduction band of the semiconductor has to be appropriate to allow for hot-electron transfer. Usually the formation of a Schottky junction is used for hot-electron extraction, where the Schottky barrier between the metal and the semiconductor allows for the transfer of hot-electrons from the metal to semiconductor only when the energy of the former is higher than that

of the Schottky barrier.[55, 59–62] The Schottky barrier facilitates the separation of hot-carriers from the metal by delaying their back transfer from the semiconductor to the metal. A commonly used semiconductor is titanium dioxide (TiO_2), mostly due to its wide bandgap (E_g = 3.2 eV, anatase phase), the high density of states in its conduction band and the availability of different methods for its synthesis or deposition. [63–65]

1.1.2 Semiconductors

Semiconductor nanomaterials can also interact resonantly with light and result in light confinement and enhanced absorption. The optical resonances of semiconductor nanostructures can be also tuned as in the case of metals, altering the geometrical characteristics of the nanostructures, the refractive index of the material and that of the non-absorbing surrounding medium. Herein, we are specifically discussing the case of vertical nanowires on a substrate, which have been extensively explored in literature especially for applications in photovoltaics due to absorption enhancement. Vertical nanowires can efficiently trap the incident light acting as waveguides and/or Fabry-Perot cavities. The light confinement profile along the length of vertical nanowires can be also tailored, providing a tunable landscape of absorption and charge generation useful for spatially controlled chemical reactions.

Resonances in vertical semiconductor nanowires emerge from the coupling of light to leaky waveguide modes supported by the nanowires. These leaky modes are actually electromagnetic confined modes, the excitation of which depends mostly on the dimensions of the structure and on light's polarization, wavelength and angle of incidence. Leaky mode profile in semiconductor nanowires can be obtained by solving the dispersion relation, which is derived by Maxwell's equations.[66, 67] In nanowires with subwavelength diameters, excited with an electric field perpendicular to their long axis, the lowest order leaky mode (HE_{11}) is mainly accessible. The incident wave will couple efficiently to the HE_{11} mode only when there is spatial overlap between the two and the mode can be still excited from free space. As a result, in a nanowire with a specific diameter excited at short wavelengths, the spatial overlap between the incident electromagnetic wave and the supported mode is small, since the leaky mode is tightly confined in the nanowire, leading to weak coupling. On the other extreme, longer wavelengths may not interact at all with the broader leaky mode in the nanowire resulting in evanescent waves in the surrounding medium. The maximum absorption should occur at the critical coupling condition, when the loss rate from the mode to free space is the same as the loss rate due to absorption.[68–74] Consequently, the spectral position of a resonance assosiated with the HE_{11} mode is highly dependent on the diameter of the nanostructure and it redshifts as the diameter increases (Figure 1.5b), resulting in tunable resonances ranging from the visible to the NIR. For much larger nanowire diameters (Figure 1.5b), higher order modes (HE_{12},HE_{13} etc.) can be supported by the nanostructure leading to more than one resonant peak.

Tuning of the spatial profile of the electric field, consequently also the absorption, in a

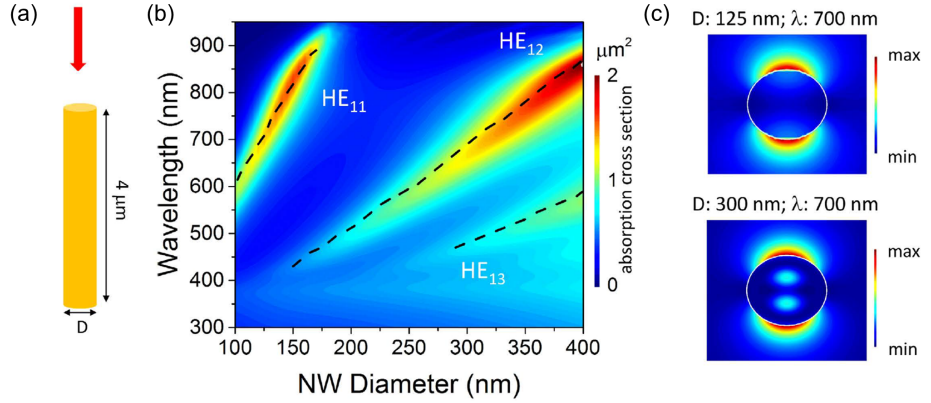

Figure 1.5. Leaky mode profile in vertical semiconductor nanowires. a) Schematic illustration of the illumination configuration studied: A single nanowire is illuminated with a plane wave propagating along a direction parallel to the axis of the nanowire. The nanowire height is 4 μm. b) Absorption cross section data for the nanowire as a function of its diameter and incident wavelength. The dashed lines are the maxima of product of overlap integral between incident field and field profile of the HE_{11}, HE_{12} and HE_{13} modes and the corresponding confinement factors. c) Electric field intensity profiles across the cross section of the nanowire at a wavelength of 700 nm for nanowire diameters of 125 nm and 300 nm. Reproduced with permission from reference [68].

vertical nanowire can be achieved through changes in the length of the nanostructure and introduction of tapering. In tapered nanowires, where the diameter of the nanostructure is changing along its length, light will couple to different HE_{11} leaky modes supported at different heights of the nanostructure.[75, 76] As a result, a change in the degree or direction of tapering can offer control over the absorption profile in the nanowire. The length of the vertical nanowire can also be a tuning parameter of the optical resonances and the resulting absorption, due to the fact that such type of nanostructures can also act as Fabry-Perot cavities.[77, 78] The Fabry-Perot behavior of vertical nanowires excited from the top interface originates from the trapping of light inside the nanostructure, due to the finite length of the nanostructure and the high refractive index contrast between the semiconductor material and the non-absorbing surrounding medium. In a typical Fabry-Perot cavity, light is trapped between two highly-reflective mirrors and resonances occur when light meets its own reflections, which have a phase equal to a positive integer multiple of 2π of that of the incident light. In the case of a nanowire, the incident light can be trapped between the top (air/semiconductor) and the bottom (semiconductor/substrate) interface and resonances can appear along its height. Absorption maxima on the nanowire correspond to areas where the interference of the incident light with its

own reflections is constructive and the spatial distribution of these absorption maxima depend on the length of the nanowire, i.e. cavity. The amount of round trips of the light inside the nanowire, before the complete attenuation of light, decrease as the length of the nanowire increases. In that way, the Fabry-Perot supported modes in long vertical nanowires will be quite weak and resonances corresponding to HE_{1m} modes (where m is the order of the mode) will be more prominent. The reflections of light inside the nanowire and consequently the resonance and absorption maxima are also affected by the refractive index contrast of the nanowire/substrate and nanowire/medium interfaces.

Charge generation in semiconductor nanostructures

In this thesis, the absorption profile of vertical semiconductor nanostructures is tuned by excitation of different optical resonances, in order to manipulate the charge generation along the axis of the nanostructures. Optical resonances are tuned to alter the absorption profile from the standard exponential decay seen with the Lambert-Beer law. By moving absorption maxima throughout the nanowire length, it is then possible to control where photocarriers are generated and therefore where a chemical reaction occurs for the formation of another nanomaterial. This enables lithography-free patterning along the length of vertical nanowires, with a spatial resolution on the order of the wavelength of light in the material. As a result, the nanostructures can be designed appropriately to support specific optical resonances to maximize absorption of light and/or spatially tune the absorption profile on their volume and its proximity. [69, 79, 80]

The absorption profile in a bulk semiconductor follows Beer-Lambert law, where the absorption is exponentially decaying as a function of the distance from the surface of the material. The spatial tuning of the absorption profile in a bulk material is very limited and it mostly depends on the absorption coefficient and the refractive index of the material, which in this case is considered constant for a specific wavelength. On the other hand, the absorption profile in a vertical semiconductor nanowire can be changed due to the supported optical resonances.[81–83] The effective refractive index, which is the ratio of the light's phase delay in the waveguide (nanowire) to that in vacuum, is different than the refractive index of the respective bulk material and it also changes for each of the supported modes in the nanowire. The effective refractive index along the length of a nanowire is altered due to the appearance of optical maxima and minima corresponding to an excited supported mode. At optical maxima, the effective refractive index is related to the supported mode while at optical minima is similar to the refractive index of air. As a result, an absorption spatial distribution along the nanowire's length can be created and tuned by exciting different resonant modes. [71]

The absorption of a photon by a semiconductor can take place when the energy of the former is equal or larger than the band gap energy (E_g) of the semiconductor. The absorption of the photon will excite an electron from the valence band of the semiconductor to its conduction band.[84, 85] If the energy of the photon is larger than E_g then the electron excitation will take place in higher unoccupied energy states and then it

will thermalize through electron-electron and electron-phonon scattering to the bottom of the conduction band. As soon as the electron and hole are separated in the conduction and valence band respectively, they are free to move, be collected and generate electricity and participate in chemical reactions. Extraction of charges with energy in excess of E_g has been also reported, but extraction efficiencies of these "hot" carriers are very low due to their short lifetime and fast thermalization (few hundreds of ps) through electron-electron and electron-phonon interactions.[86–88] Herein we are not dealing with "hot" carrier extraction from semiconductor nanomaterials, since the lifetime of the excitons (around 1 μs) is already long enough for driving chemical reactions.

1.2 Driving light-induced chemical reactions with nanomaterials

Optical resonances and localized charge generation in nanomaterials can be used to drive chemical reactions in confined volumes, at the hot-spots of nanostructures. In that way, spatially controlled chemical reactions with nanoscale resolution can be used for synthesis of new materials on the optically excited nanostructures. As a result, light combined with colloidal synthesis of nanostructures with controlled shape and size, can constitute a tool for fabrication of complicated nanomaterials. Electrochemistry and specifically photoelectrochemistry principles are used here for manipulation of chemical reactions with light.

1.2.1 Redox reactions

Chemical reactions which include charge transfer with a change in the oxidation state of an ion/molecule are called redox (reduction/oxidation) reactions. In redox reactions, one substance gains electrons (i.e. is reduced), while another substance loses electrons (or gains holes, i.e. is oxidized). According to the electroneutrality principle, where the unbalance of charges in bulk matter is prohibited, for every electron removed from an ion/molecule an electron has to be added to another one. As a result, a redox reaction can be described by two parts, half-reactions, where one describes the oxidation and the other one the reduction in a system and always take place simultaneously. It is possible to physically separate the half-reactions, while ensuring electroneutrality, in a device called an electrochemical cell. Usually, such a system consists of two electrodes (anode and cathode), an electrolyte and an external circuit. The oxidation half-reaction occurs at the anode, reduction half-reaction occurs at the cathode and electron flow from one electrode to another is achieved through the external circuit. The electrolyte as an ionic medium compensates the electron flow in the system with ionic transfer and ensures electroneutrality.[89]

The ease with which a redox half reaction occurs is called redox potential, is measured in volts and shows how easy a chemical species gains electrons. The redox potential on

the vacuum scale is analogous to the Fermi level of a semiconductor, as it represents the energy at which electrons are added to or removed from the system. Redox potentials are conventionally presented with respect to the standard hydrogen electrode (SHE), which is a reference electrode where the reversible H_2 generation half-reaction takes place on the surface of a Pt electrode. The redox potential of a SHE reference electrode is set to zero (- 4.5 eV on the vacuum scale), since it is considered constant at any temperature under standard conditions (1 bar, 1M of electrolyte).[90, 91] Any other redox potential can be represented as the potential difference from the SHE potential, where the more positive this difference is, the easier a chemical species receives electrons and the more negative, the higher its tendency to lose electrons. Conventionally, the sign of redox potentials on the SHE scale is opposite than that of the vacuum (i.e. more positive redox potential is more negative on vacuum scale, Figure 1.6). This reference half reaction can be also included in an electrochemical cell in the form of a third electrode (reference electrode) to actively measure the redox potential of a half-reaction. In this thesis a silver chloride reference electrode is used due to its stability and miniaturization ability. In the SHE scale Ag/AgCl electrode has a redox potential of 0.197 V (Figure 1.6).

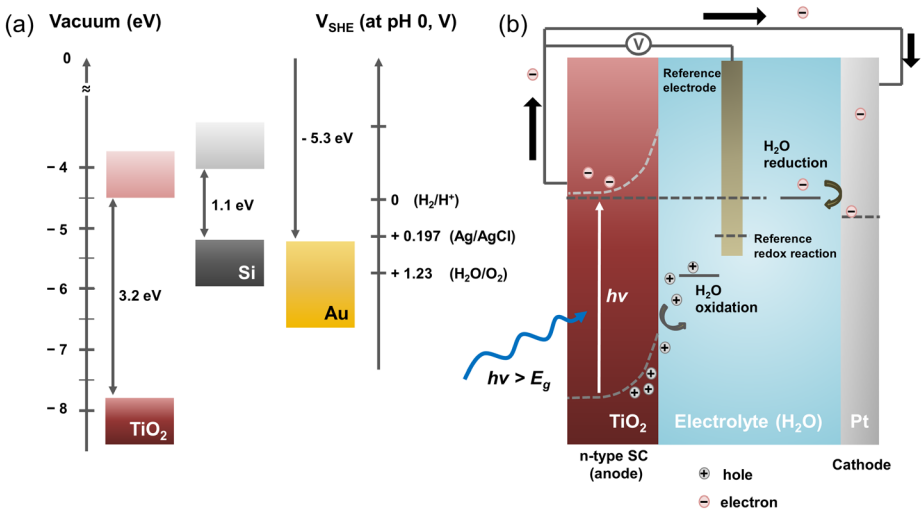

Figure 1.6. Redox potentials and photoelectrochemical cell. a) Energy band levels of TiO_2 and Si and Fermi level of Au on the vacuum scale. Also, water oxidation and reduction potentials and reference electrode (Ag/AgCl) redox potential on SHE scale, where 0 V corresponds to - 4.5 eV on the vacuum scale. b) Water splitting in a three-electrode photoelectrochemical cell, with TiO_2 as the anode electrode (working electrode), a reference electrode (Ag/AgCl) and a metal (Pt) counter electrode in contact with the electrolyte (H_2O).

An electronic device has to be added to an electrochemical cell in order to make the connections between the three electrodes (anode, cathode, reference), measure redox potentials of either the anode or the cathode with respect to the reference electrode, record the current flow in the cell as well as provide additional energy to a reaction when it is needed (nonspontaneous redox reaction). Such a device/instrument is called potentiostat and controls the potential between the reference electrode and the anode (or cathode), which is called working electrode and involves the reduction (or oxidation) half-reaction. This potential control is achieved by sending current to the other electrode (counter electrode). A potential between the reference electrode and the working electrode can be applied when a half-reaction cannot occur spontaneously on the working electrode and extra work has to be provided. This extra potential needed to start detecting current flow as the result of the half-reaction occurring is the redox potential of the reaction under these specific conditions measured. [92, 93]

1.2.2 Light-driven redox reactions

The working electrode in a 3-electrode electrochemical cell can consist of materials which can absorb light (photoelectrodes), convert photons to charges and then either directly to electricity and/or to chemical species through redox reactions. If a redox reaction is nonspontaneous then instead of providing the extra energy needed by applying a potential through the external circuit, illumination of the photoelectrodes can provide the voltage bias. It is important the materials chosen as photoelectrodes absorb photons and generate electrons with energy equal or higher than the redox potential of the desired reaction.[69, 92, 94, 95]

Semiconductor nanostructures

In semiconductor photoelectrodes, absorption of a photon with energy $hv > E_{band-gap}$ leads to the excitation of an electron from the valence band to the conduction band, resulting in generation of free charges with the same energy with the photon. The photogenerated charges can reach the semiconductor/electrolyte interface, meet the molecular species and either reduce or oxidize if hv is sufficient, i.e. the redox potential of the chemical reaction lies within the bandgap of the semiconductor (Figure 1.6). During the immersion of a semiconductor in an electrolyte with redox species, band bending will occur in order to reach an equilibrium between the Fermi level of the semiconductor and the redox potential of the electrolyte. This band bending is responsible for the charge separation which drives the redox reaction. Many semiconductors have bandgaps with sufficient energy to drive redox reactions and some of the most commonly used are TiO_2, a-Fe_2O_3, WO_3 and ZnO.[90] Recently silicon nanomaterials attracted attention as promising photoelectrodes mostly due to the facile nanostructuring, material abundance, tunable electrical properties through doping and the highly investigated optical and electrical properties in the field of photovoltaics.[96, 97]

There are several examples of light-driven redox reactions mediated by semiconductor nanostructures such as water splitting, CO_2 reduction, water purification and ammonia synthesis from nitrogen reduction.[98–100] Spatially selective deposition of other nanomaterials on semiconductor nanostructures was also achieved through photo-induced redox reactions.[90] Selective deposition of different metals and metal oxides on different facets of bismuth vanadate nanostructures was demonstrated, showing that each of those facets corresponds to injection areas of either photogenerated electrons or holes.[95, 101]

Metal nanostructures

Metal nanostructures have drawn the attention in light-driven redox reactions due to the extreme electric field enhancement in subwavelength volumes (hot-spots), their tunable absorption across the whole visible spectrum and the generation of highly energetic carriers.[51, 102] Spatially selective chemical reactions for material overgrowth or deposition of another nanomaterial on the hot-spots of plasmonic nanomaterials have been already conducted. Silver nanoplate overgrowth associated with hot-electron participation was one of the very first demonstrations that chemical reactions can be conducted localized and at the hot-spots of plasmonic nanoparticles. Ever since, more examples came to prove that hot-electron mediated chemistry can be controlled spatially and spectrally. Overgrowth of gold nanoprisms, platinum nanoparticle formation on hot-spots of single gold nanorods and reduction of diazonium salts on gold nanotriangles are some of these examples.[103]

Photogenerated highly-energetic carriers can be extracted from plasmonic metal nanostructures to drive chemical reactions, but even with a Schottky junction assisting with charge separation quantum efficiencies are typically very low.[104] These low efficiencies originate from electron-hole recombination before the reaction occurs. For instance, a hot-electron after its injection to the conduction band of a semiconductor will reach the semiconductor interface to find adsorbed molecular species and reduce them. The timescales of common redox reactions are 1 μs - 1 ms, usually longer than the recombination time of the electron in the conduction band with the hot-hole remaining in the metal. This means electron-hole recombination can occur and the rate of the reaction can be limited. The reaction rates though depend also on the time that a molecule will "spend" at the semiconductor/electrolyte interface and if indeed adsorption of molecules on the semiconductor or metal surface will take place or not.[105, 106] The surface of the semiconductor and the nature of the chemical bonds can affect the adsorption of a molecular species.

There are two primary methods for reducing recombination of electrons and holes and increasing the quantum efficiency in metals. The first approach includes the addition of a cocatalyst nanomaterial to the plasmonic nanostructure. A cocatalyst is a material which does not have good optical properties for efficient light trapping and absorption, but acts as a good catalyst in combination with a light absorbing material. The presence of such a material can increase the kinetics of the chemical reaction facilitating lower en-

ergy surface states for molecules to adsorb and/or desorb, resulting in chemical reaction rates faster than electron-hole recombination timescales. Bimetallic heterostructures including both the plasmonic and the cocatalyst nanomaterial have been synthesized in literature and explored in different redox reactions. The second approach to decrease electron-hole recombination in a plasmonic photocatalyst is to add an electron or hole scavenger to the electrolyte. A hole (electron) scavenger is a molecular species with a small enough reduction potential to be oxidized (reduced) faster than electron-hole recombination occurs. In that way, a hot-carrier has the time to participate in a chemical reaction, while the respective hot-carrier is scavenged away by participating in a much "easier" redox reaction.[107, 108]

In literature, both the hot-carriers and the increase of the local temperature (after the complete thermalization of the hot-carriers) in plasmonic nanomaterials have been used for light-driven redox reactions. The distinction though between these two plasmonic mechanisms has raised a big debate in the field, specifically around the contribution of each of them in a chemical reaction. In plasmonic heating, the increase in temperature leads to an increase in the reaction rate for endothermic reactions. However, such an effect does not require optical excitation of hot carriers and can instead be achieved by traditional heating methods. Additionally, the spatial sensitivity is often lost due to rapid heat conduction. On the other hand, hot carrier induced chemical reactions have demonstrated enhanced selectivity over chemical products and linear and superlinear dependence of the reaction rate on the incident light's intensity in contrast to traditional thermal catalysis. As a result, lower light intensities are needed to achieve high reaction rates with hot-carriers than with a temperature increase. A comparison of the two different mechanisms on rhodium (Rh) plasmonic nanoparticles used for methane (CH_4) generation from CO_2 hydrogenation, showed that hot-electrons can selectively produce methane in contrast to thermal catalysis which resulted in a combination of chemical products (CH_4 and CO) at comparable rates.[109] The selectivity over specific chemical products originates from the hot-carrier injection to specific molecular orbitals responsible for the occurrence of a specific chemical reaction. In reality, it is very difficult and maybe impossible to completely separate these two mechanisms: thermal and hot-carrier-induced redox reactions in plasmonic nanomaterials. In the end, it is believed that a synergistic effect is behind the enhanced chemical reaction rates with plasmonic photocatalysts compared to just thermal activation of chemical reactions. Efforts to separate these two mechanisms are just beginning to appear, but further work is needed to clarify their exact contribution in different plasmonic nanostructures. [110–112]

1.3 Motivation and outline

The aim of this thesis is to explore if optical resonances in metal and semiconductor nanostructures can be used as a nanophotonics tool for driving spatially resolved chemical reactions for the formation of new nanomaterials.

In **Chapter 2** we fabricate vertical silicon nanowires with different tapering angles and first we explore their optical resonances and the absorption profile along their height with FDTD simulations. We demonstrate the appearance of absorption maxima along the height for 3 different types of silicon nanostructures: nanowires, nanocones and inverted nanocones and we use them for selective deposition of Pt nanoparticles. Excitation of the nanostructures at two different wavelengths, in presence of a Pt salt, reveals the formation of metallic Pt nanoparticles as the result of the Pt salt reduction by the photogenerated charges in silicon. The location of the photodeposited Pt is correlated with the absorption maxima for the 3 different types of vertical silicon nanowires.

In **Chapter 3** we turn our focus to plasmonic nanoparticles. We fabricate photocathodes, made of gold nano-islands and coated with a thin TiO_2 layer and we excite them at their surface plasmon resonance in order to investigate their ability to generate hot-electrons. We demonstrate through photoelectrochemical measurements that the photogenerated hot-electrons can drive redox reactions and reduce a Pt salt to metallic Pt cocatalyst nanoparticles. We also explore if this method of positioning the cocatalyst nanomaterial on the surface of the plasmonic photocathodes leads to a higher photocatalytic activity than a random system.

In **Chapter 4** we investigate if the same gold nano-islands in a slightly different configuration can be also used for the generation of hot-holes. By illuminating the plasmonic nanostructures at their surface plasmon resonance, we explore the hot-hole assisted oxidation of a manganese salt on the surface of the nanostructures. Both of the hot-carriers are also used at the same time for simultaneous deposition of more than one nanomaterial. We demonstrate that hot-electrons and hot-holes can also act at the same time and drive with the same plasmonic nanostructrues more than one chemical-reaction for deposition of different nanomaterials.

Overall, this thesis provides evidence that manipulation of light at the nanoscale can open new pathways for the efficient design of complicated nanostructures, which cannot be made with any other available nanofabrication method.

2

Localized photodeposition of catalysts using nanophotonic resonances in silicon photocathodes

Nanostructured semiconductors feature resonant optical modes that confine light absorption in specific areas called "hot-spots". These areas can be used for localized extraction of the photo-generated charges, which in turn could drive chemical reactions for synthesis of catalytic materials. In this work, we use these nanophotonic hot-spots in vertical silicon nanowires to locally deposit platinum nanoparticles in a photoelectrochemical system. The tapering angle of the silicon nan-owires as well as the excitation wavelength are used to control the location of the hot-spots together with the deposition sites of the platinum catalyst. A combination of finite difference time domain (FDTD) simulations with scanning electron microscopy image analysis showed a reasonable correlation between the simulated hot-spots and the actual experimental localization and quantity of platinum atoms. This nanophotonic approach of driving chemical reactions at the nanoscale using the optical properties of the photoelectrode, can be very promising for the design of lithography-free and efficient hierarchical nanostructures for solar fuels generation.

2.1 Introduction

The relentless rise of CO_2 levels in the atmosphere as well as the growth of the world's population, remind us of the importance of finding new, clean pathways to cover our energy needs. Fuel generation from renewable energy resources could be one of the "clean" approaches for meeting our energy requirements. Although, sunlight is the most abundant source of green energy, its long-term storage is required, due to daily and yearly fluctuations. The most promising medium for stable, high-density storage is in the form of chemical energy, such as H_2 or organic compounds, by using photochemical fuel generators.[97, 113–115]

In the center of a photochemical fuel generator are the photoelectrodes, where light absorption and conversion to chemical energy take place. The photoelectrodes are in contact with an electrolyte which is the primary source of fuel together with the sunlight. In such a system, light absorption by the electrodes leads to creation of electron-hole pairs, which after their separation participate in chemical reactions in the electrolyte to make fuels, such as water splitting for H_2 generation.[95, 116] Carefully designed photoelectrodes are necessary for low-cost and high efficiency, which are both needed to make solar fuels competitive with fossil fuels as an energy carrier. Nanostructuring the main photoactive material, e.g. a semiconductor, has proven to be a promising method for increasing solar fuel generation efficiency.[117, 118] The higher surface to volume ratio in nanostructured semiconductors ensures the use of less material, reduces the requirements on current density and often increases light absorption. This increased light absorption comes from optical resonances in nanomaterials, which have been studied extensively in both metallic (plasmonic) and dielectric material systems.[77, 119–122] One hallmark of resonant absorption is the appearance of localized "hot spots". In particular, semiconducting nanostructures can sustain Mie-like leaky modes due to their high-refractive index and the occurrence of multiple internal light reflections from the boundaries of the structure.[119, 123] However, in vertical nanowires with normal incidence illumination, Mie modes cannot be excited and instead coupling to waveguide modes (e.g. the HE_{11}) and subsequent Fabry-Perot cavity interference plays the dominant role in creating these hot-spots.[78, 124] The highly concentrated electric fields at the hot-spots lead to elevated concentrations of photogenerated charge carriers that can be used to drive solar fuel reactions.[20, 125–127] Additionally, photochemical fuel generators require a catalyst, such as platinum, to lower the overpotential to drive the chemical reaction.[95, 114, 128–132] The catalyst would be ideally located at the semiconductor-solution interface, directly at the location of the hot-spots.

Placing the catalyst exclusively at the hot-spots would reduce both the catalyst loading (lowering the cost) and the average time between charge generation and chemical reaction (increasing the efficiency). However, current catalysts are simply randomly placed on semiconductor photoelectrodes with an optimized average density.[128, 132, 133] Photodeposition of the catalytic material, with the photogenerated charges from

excited semiconductors, has been also achieved but without a good control on the deposition sites.[134–139] An exception is the work of Li et al.[135], where charge separation was achieved at different crystal facets of $BiVO_4$ nanocrystals for selective photodeposition of metal and metal oxide catalytic nanoparticles. Nevertheless, this method for the moment is limited to this specific material and structure.

Here we present a different approach where localized nanophotonic resonances in semiconductors are used to place catalyst particles exactly where they are needed. We show that the location of catalyst deposition on vertical silicon nanowires can be tuned by adjusting their shape (tapering angle) or changing the excitation wavelength. The experimentally observed deposition profiles match reasonably well with optical simulations of the photogenerated charge carrier distribution for each shape and wavelength. Most notably, deposition profiles far from those expected from a simple Beer-Lambert law have been obtained, in contrast to previous related work on silicon microwires.[140, 141] Our results provide the first step for rationally designed catalyst positioning using the underlying resonant properties of nanoscale photocatalysts, tunable simply by altering the shape, size or excitation wavelength. The extensive literature on such nanophotonic tuning makes this an exciting approach for lithography-free, nanoscale catalyst positioning control.[142–146]

We have chosen vertical silicon nanowires as a model nanophotonic system because of their ease of fabrication, known optical constants and broad spectral absorption range. In presence of a Pt-catalyst precursor (H_2PtCl_6) in a 3-electrode photoelectrochemical system (Figure 2.1), photogenerated electrons reach the surface of the silicon nanowires, reducing the precursor to form metallic platinum nanoparticles (Pt^0). The position of the Pt deposition can be controlled by adjusting the tapering angle or the incident wavelength. The platinum photodeposition results are observed with a scanning electron microscope (SEM) and compared with the output of finite difference time domain (FDTD) simulations, which reveal the photogenerated carrier density distribution within the silicon nanostructures.

2.2 Results

2.2.1 Fabrication of silicon nanostructures and calculation of their optical modes

Silicon nanostructures were fabricated by etching a p-type silicon substrate using a combination of Cl_2 and HBr/O_2 plasmas, where 110 nm diameter SiO_2 spheres were used as an etch mask. Tuning the ratio of the HBr/O_2 plasmas allowed for vertical nanowires with variable sidewall tapering angle (see details in Methods section and Figure 2.5). Vertical nanocones (height $\approx$ 720 nm, top diameter $\approx$ 60 nm , bottom diameter $\approx$ 160 nm, angle $\approx$ 15°), inverted nanocones (height $\approx$ 1 μm, top diameter $\approx$ 70 nm, base diameter $\approx$ 120 nm and smallest diameter $\approx$ 60 nm) and nanowires (height $\approx$

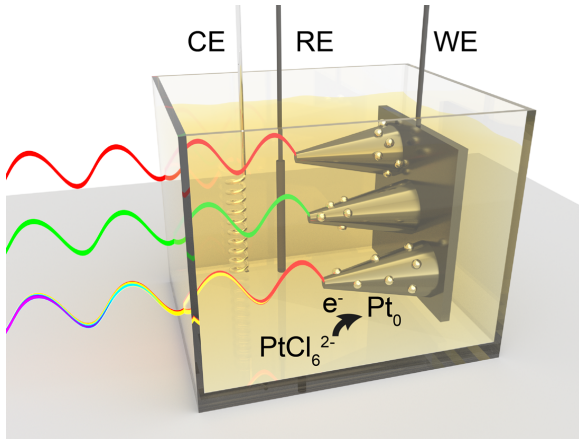

Figure 2.1. Schematic illustration of the photoelectrochemical deposition of metallic Pt on silicon nanostructures from hexachloroplatinate ($PtCl_6^{2-}$) in a three-electrode photoelectrochemical cell with counter electrode (CE), reference electrode (RE), and working electrode (WE). The location of catalyst deposition can be tuned by adjusting the excitation wavelength from red to green to white, or (not shown) the nanostructure shape.

790 nm, diameter ≈ 80 nm) were fabricated here and subsequently used to tune the distribution of photogenerated carriers (Figure 2.2). An 18 nm amorphous TiO_2 layer was conformally deposited on the silicon nanostructures using atomic layer deposition (ALD). This layer assists with charge separation, stabilizes the silicon surface and helps passivate traps states, leading to well-known improvements in photoelectrochemical performance.[147–149] The amorphous TiO_2 layer was further annealed at 350 °C for 3h to form crystalline anatase TiO_2, which led to improved performance. The final TiO_2 layers were characterized with x-ray diffraction (XRD) (Figure 2.6) and ellipsometry (Figure 2.7) to verify their quality. Both the XRD pattern and optical constants (n & k values) matched literature values for thin anatase TiO_2 films.[150]

The photocarrier density distribution under monochromatic illumination (532 or 638 nm) in the Si-TiO_2 nanostructures was simulated using the FDTD method. It was assumed that every absorbed photon was converted to an electron-hole pair and only the optical effects were taken into account in the simulations. The dimensions of the average silicon nanostructures extracted from SEM images were used for the simulations, while the n & k values measured with ellipsometry were used for the TiO_2 coating. Every structure was simulated on a thick silicon substrate, also coated with 18 nm TiO_2 , and the surrounding refractive index was set to 1.33 to resemble the aqueous conditions of the reaction environment. The simulations show the cross-sectional absorbed power profiles (normalized to the maximum value per plot) of the 3 different silicon nanostructures, for excitation at 532 nm (Figure 2.2b) and 638 nm (Figure 2.2c). The location of the hot-

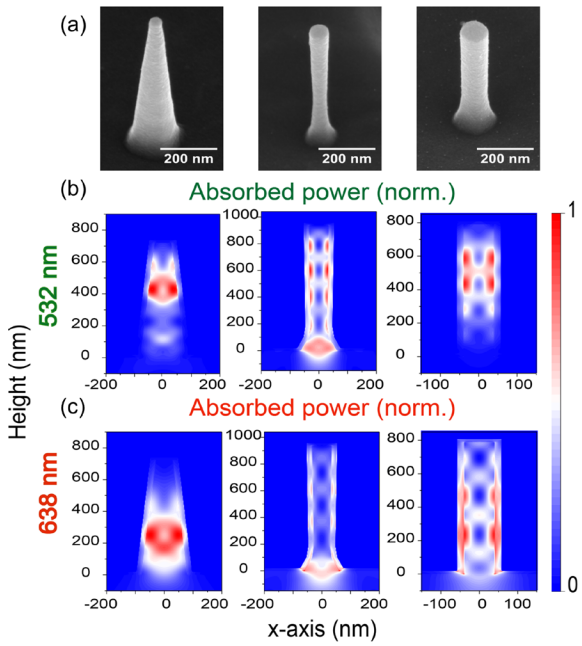

Figure 2.2. a) SEM images of a silicon nanocone (left), an inverted nanocone (middle) and a nanowire (right) coated with an 18 nm TiO_2 layer. The tapering angle was controlled by varying the Cl_2 and HBr/O_2 flow rates during plasma etching b) and c) FDTD simulations of absorbed power in each nanostructure at 532 nm (b) and 638 nm (c) normalized to the maximum value.

spots depend on the excitation wavelength and the shape of the nanostructure. Silicon nanocones confine light mostly on the top of the structure at 532 nm (Figure 2.2b) in contrast to an excitation at 638 nm, where most of the light is absorbed in the bottom of the cone (Figure 2.2c). In the case of inverted nanocones, light is concentrated primarily at the bottom for both wavelengths, although at 532 nm there are also additional hot-spots along the height. In silicon nanowires, hot-spots are present on the top and the middle of the structure for 532 nm but for excitation at 638 nm, more hot-spots appear. Overall, the results of these simulations confirm the presence of distinct hot-spots in the nanostructures and enable us to investigate whether the simulated hot-spots match the location of the deposited catalytic material after illumination.

2.2.2 Photodeposition of platinum

A three-electrode photoelectrochemical cell, electrically connected with a potentiostat, was used for deposition of the platinum catalyst on the nanostructures. The sample

served as the working electrode (WE) with a platinum wire counter electrode (CE) and Ag/AgCl reference electrode (RE) (Figure 2.1). During a typical photo-electrodeposition experiment, the sample was mounted in direct contact with a Pt-precursor electrolyte (4 mM H_2PtCl_6, pH 11) and the current flow to the working electrode was recorded as a function of time at a constant electrochemical potential, i.e. chronoamperometry mode. The samples had an open-circuit voltage potential of around −0.1 V (vs Ag/AgCl) and were biased by 700 mV to a more reducing potential of −0.8 V (vs Ag/AgCl) during deposition, to efficiently extract the photogenerated charges from the Si nanostructures into the electrolyte and enhance the kinetics of the reaction. The flat-band potential of TiO_2 at pH 11 is above the conduction band edge of p-type silicon, so TiO_2 acts as an electron blocking layer here.[95, 151, 152] Therefore, the presence of TiO_2 offers a control over the potential we could apply to selectively promote photodeposition while avoiding electrodeposition, In the absence of a TiO_2 layer the recorded dark current is much higher than the corresponding photocurrent (Figure 2.8a), which means that the electrons reaching the electrolyte by biasing the samples dominate over the photo-generated ones. SEM images (Figure 2.9) showed homogenous formation of platinum nanoparticles both on the Si nanostructures and on the substrate, when the samples were illuminated without the TiO_2 layer but still in biased conditions. The final potential value (−0.8 V) for photo-electrodeposition of platinum nanoparticles in the presence of a TiO_2 layer was chosen for the high current ratio under illumination versus dark conditions (Figure 2.10). Even more negative potentials than −0.8 V could be used here, but it was not necessary since the kinetics of the reaction were fast enough to drive the photo-electrodeposition in few seconds. Typically, the current was 75-200 times greater in illuminated than in dark conditions. As shown in Figure 2.3b, during the first 20 sec of a typical photo-electrodeposition experiment using 532 nm light, the laser beam was blocked and the current was recorded. As soon as the laser beam hit the sample, a current increase was observed due to the contribution of the photogenerated charges. After an electrical charge of around 1.35 mC was passed to the illuminated sample, the laser beam was blocked again and the measurement was stopped.

The area of the laser beam (0.06 mm^2 for 532 nm and 0.35 mm^2 for 638 nm beam) was much smaller than the surface of the samples in contact with the electrolyte (0.3 cm^2), which allowed straightforward identification of the illuminated area and discrimination of platinum deposition in light and dark conditions in the same experiment (Figure 2.11). SEM images (Figure 2.3a and Figure 2.12) taken from the illuminated region revealed the presence of new nanoparticles on the silicon nanostructures and substrate. These were not observed far from the illuminated region (Figure 2.13), which confirmed that the irradiation had caused nanoparticle formation. Energy-dispersive x-ray spectrometry (EDS) mapping clearly confirmed the presence of platinum, when an individual newly formed particle was analyzed (Figure 2.3d and Figure 2.3e). Furthermore, the oxidation state of platinum was investigated with x-ray photoelectron spectroscopy (XPS) on a sample with a higher amount of photo-electrodeposited platinum ($\sim$ 2 mC). The observed platinum $4f_{7/2}$ and $4f_{5/2}$ binding energy peaks corresponded very well to those

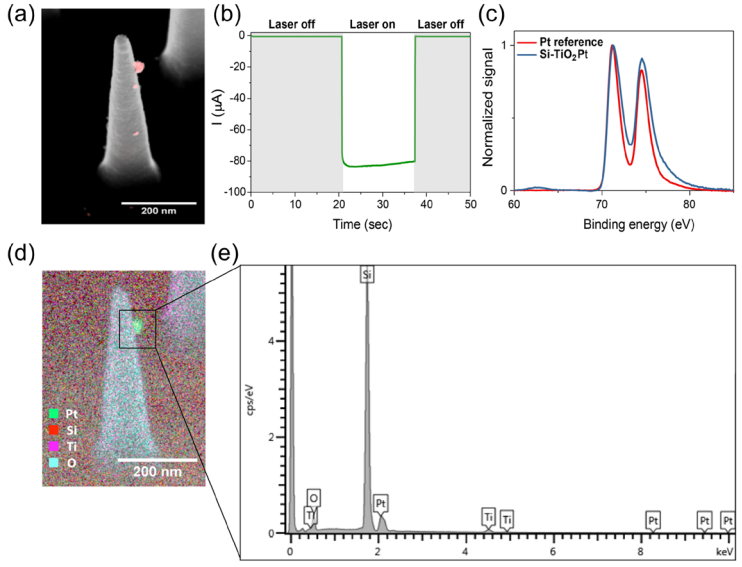

Figure 2.3. a) An overlay image of a back scattered electron (red; in-lens mirror detector) and secondary electron (grey; through-the-lens detector) SEM image of a silicon nanocone after photo-electrodeposition of platinum. b) Current versus time plot during a photo-electrodeposition experiment of silicon nanocones excited at 532 nm (laser on), at −0.8 V applied potential in an aqueous solution of H_2PtCl_6 (pH 11). c) X-ray photoemission spectrum of photo-electrodeposited platinum on silicon nanostructures (blue) compared with the spectrum of a metallic Pt reference material (red). d) EDS elemental map where each color indicates a different element: Pt (green), Si (red), Ti (purple) and O (cyan). e) Elemental map retrieved from an individual deposited particle (100 pA beam current, 10 kV acceleration beam voltage).

of a metallic Pt reference material (Figure 2.3c). Overall, these results demonstrate that light can be used as an external stimulus for the catalytic material (Pt^0) formation on Si nanostructures.

2.2.3 Correlation of hot-spots and Pt deposition sites

Next, a comparison was made of the Pt deposition sites and the simulated optical hot-spots of the Si nanostructures with an SEM image analysis approach, as follows. First, preliminary chronoamperometric experiments were conducted to indicate the conditions, in which we could easily identify the location of the platinum particles on each nanostructure without the total overgrowth of the latter. A total amount of around 1 mC was needed to achieve well separated Pt particles with a diameter of 11 nm, which typically

corresponded to 15 – 20 sec of illumination at 532 or 638 nm with a light intensity of 1.2 W/cm^2 or 0.35 W/cm^2, respectively. The size of the deposited platinum nanoparticles was selected only for particle identification purposes and further optimization of the photo-electrodeposition process is necessary for fabrication of efficient photocatalytic samples. For each Si nanostructure morphology, overlays of secondary-electron and backscattered-electron (collected with an in-lens mirror detector) SEM images were acquired. This overlay method facilitates the identification of platinum nanoparticles based on the high electron backscattering efficiency of this heavy element (Figure 2.4a, Figure 2.14, Figure 2.15 and Figure 2.16). Images were collected from 100 individual nanostructures of each morphology, while exclusively considering structures with dimensions within half a standard deviation of the average structure. Furthermore, platinum particles with a diameter below 6 nm were excluded, as they could also originate from electrodeposition (Figure 2.13). The volume of each Pt nanoparticle was estimated and converted to the corresponding number of platinum atoms. Finally, histograms were made to visualize the amount of deposition as a function of Si nanostructure height (Figure 2.4b and Figure 2.4c). The results are presented together with the simulated integrated absorbed power (normalized to the maximum value per plot) along the height of every structure at 532 and 638 nm.

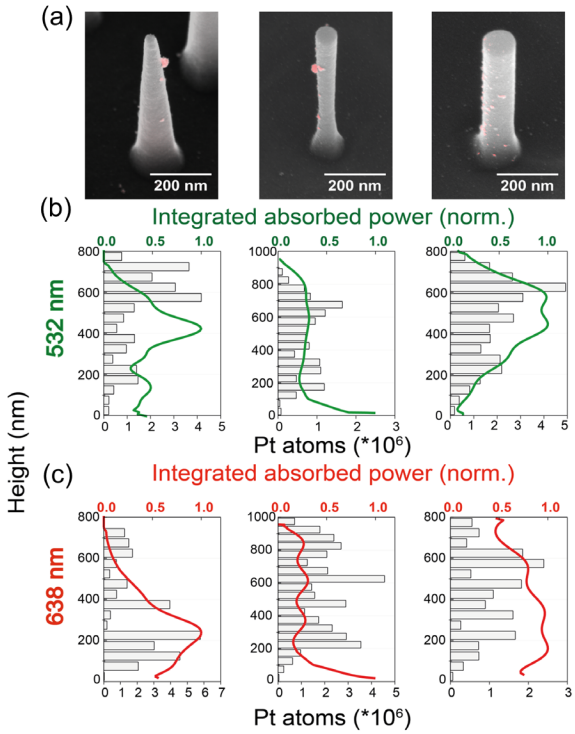

Figure 2.4. a) Overlay images of a back scattered electron (red) and secondary electron (grey) SEM images after photo-electrodeposition of platinum on a silicon nanocone (left), inverted nanocone (middle), and nanowire (right). b and c) Total amount of platinum atoms deposited (grey bars) along the height of each silicon structure for excitation at 532 nm (b) and 638 nm (c). Each graph includes the accumulated values of 100 structures. Green and red solid lines correspond to the integrated absorbed power (normalized to the maximum value) as a function of height at 532 nm and 638 nm, respectively.

Comparison of the platinum deposition distribution on the silicon nanostructures and the integrated absorbed power profiles, reveals that they match reasonably. Specifically, for silicon nanocones a correlation of the platinum deposition sites and the optical modes is shown for both of the excitation wavelengths with some deviations. At 532 nm, the two peaks of the platinum distribution are slightly shifted towards larger heights, while at 638 nm deposition of platinum is also observed in locations not expected from the absorbed power simulations, i.e. on the top of the nanostructure. In the case of inverted nanocones, the platinum deposition profiles seem to follow the ones of the integrated absorbed power. However, simulations showed that most of the light is absorbed on

the bottom of the nanostructure, where no platinum is observed in the experiments. In contrast, deposition of the catalytic material occurs primarily at a height of around 200 – 300 nm from the bottom. This discrepancy may be explained by the fact that both nanocones and inverted nanocones exhibit structural diameter differences along their height, which could lead to differences in carrier collection efficiency if the diffusion length is on the order of, or smaller than, the diameter. Such variations in carrier collection efficiency would naturally alter the final deposition distribution in a manner qualitatively consistent with our observations. Finally, silicon nanowires excited at 532 nm concentrate the incident light mostly on the top–middle of the structure, corresponding well with the platinum deposition analysis. For 638 nm excitation, the same structures exhibited multiple deposition sites along their height, which is also correlated to the integrated absorbed power peaks. Instead of formation of new small particles of platinum on the silicon nanostructures, overgrowth of the already deposited ones was noticed from the SEM images (Figure 2.14, Figure 2.15 and Figure 2.16). This effect could be explained by the fact that platinum nanoparticles act as electron-trapping centers on the surface of TiO_2.[153, 154] After the formation of the very first platinum nanoparticles, photogenerated electrons from silicon nanostructures are transferred to TiO_2 and in sequence to the already-formed platinum. The Schottky barrier between TiO_2 and platinum nanoparticles does not allow the "back" transfer of electrons so charge separation is promoted, which allows further reduction of hexachloroplatinate to Pt^0 on one of the existing platinum nanoparticles rather than in new locations. As a result, the initial platinum nanoparticle formation may alter the final deposition profile from the simulated one by prohibiting the deposition on other parts of the nanostructrure. As mentioned earlier, an external electric field is applied to the samples for more efficient extraction of the photo-generated charges. This electric field is not taken into account in the simulated distribution of the charges along the height of the Si nanostructures (Figure 2.2) and it is one more factor which could affect the localization of the photo-electrodeposition. The platinum deposition could also be broadened compared to the simulated profile due to our method of measuring the height of each particle, which extracts 3D distances from a 2D image. Noise could also be introduced by the TiO_2 layer itself. Although TiO_2 has a shorter electron diffusion length compared to silicon [155, 156], the TiO_2 surface could also have randomly distributed surface sites with higher catalytic activity, leading to preferential deposition, or traps that capture carriers preventing deposition.

2.3 Conclusions

In summary, we show that the optical modes of silicon nanostructures can be used for lithography-free patterning of catalytic nanoparticles. Tuning of the photoelectrochemical formation of platinum nanoparticles along the height of silicon nanostructures was achieved, by changing either the shape (tapering angle) of the silicon nanostructures or

the excitation wavelength (red or green light). This method utilizing the optical modes of semiconducting nanostructures to pattern catalytic materials with nanoscale control can be a very promising method for an easy and low-cost fabrication of efficient photoelectrodes. It provides a lot of flexibility on the materials involved and on the design of the final structure. Further research should be focused on improving the positioning precision and implementing the approach in a state-of-the art photoelectrode/catalyst system in order to demonstrate the potential for solar fuel production enhancement.

2.4 Supporting information

2.4.1 General

Chemical were purchased from major chemical suppliers and used as received. Scanning electron microscopy (SEM) was performed on a FEI Verios 460 with a typical acceleration beam voltage of 5 kV and 100 pA beam current. Secondary electron images were collected with a through-the-lens detector (TLD) and backscattered electron images were collected with an in-lens mirror detector. Energy dispersive x-ray spectrometry (EDS) was performed with an Oxford Instruments device with an acceleration beam voltage of 10 kV and beam current of 100 pA. X-ray diffraction was done with a Bruker D2 Phaser with Cu Kα-radiation (wavelength = 1.5418 Å).

2.4.2 Simulations

Lumerical FDTD Solutions was used for simulations of single silicon nanostructures on a 3.5 x 3.5 x 2 μm silicon substrate. Absorbed power simulations were conducted with an 18 nm TiO_2 layer, with refractive index values (n and k) retrieved from ellipsometry (Figure 2.7). An example of the simulations environment can be found in Figure 2.11 where the inverted nanocone case is presented. The structures were excited with a plane wave source with wavelengths 400-1100 nm and the absorbed power was retrieved from an absorption per unit volume monitor with wavelength selection option. The refractive index of the surrounding medium was set to 1.33. The mesh size during the FDTD simulations was equal to 2 x 2 x 2 nm for all the structures. Fabrication of silicon nanocones, inverted nanocones and vertical nanowires Silicon p-type samples (Active Business Company GmbH, <100> orientation) 12×12 mm, with 1-10 Ω*cm resistivity, were used as substrates for the fabrication of the 3 different types of silicon nanostructures. First, the samples were cleaned with soap and consecutively rinsed with copious amounts of water, acetone and isopropanol. After that, the samples were submerged in hot acid piranha (120 °C, 3:1 concentrated H_2SO_4:30% H_2O_2) for 20 min and rinsed with deionized water. Then 2-3 μL of 110 nm diameter SiO_2 spheres dispersed in ethanol were dropcast on the clean silicon samples and annealed for 1 min at 60 °C on a hot plate. The samples were etched with a combination of plasmas (PlasmaPro 100

Cobra ICP Etch). First Cl_2 (20 sec, 50 sccm, HF forward power 40 W, 7 mTorr) was used for removal of the native oxide and then HBr/O_2 (5 min for nanocones and 11 min for nanowires and inverted nanocones, HF forward power 30 W, 7 mTorr) etched silicon to the desired structures. Before the etching steps an oxygen cleaning step was used (1 min and 30 sec, 50 sccm O_2, HF forward power 60 W, ICP forward power 100 W, 6 mTorr). The temperature used for all the steps of the plasma etching was 20 °C. The ratio of $HBr:O_2$ was very crucial for the control of the shape of the silicon structures. For the nanocones a ratio of 48.2:1.8 sccm ($HBr:O_2$) was chosen, 49.5:0.5 for inverted nanocones and for stand-up nanowires 49:1. The ICP forward power during the Cl_2 and the $HBr:O_2$ etching was 750 W for silicon nanocones and nanowires, and 600 W for inverted nanocones. After the etching the samples were treated with 7 vol % HF solution for the removal of the SiO_2 formed during the etching procedure, rinsed with water, dipped in hot acid piranha for 20 min and rinsed one more time with water. The last step (hot acid piranha) proved necessary to obtain a smooth coating of the structures with TiO_2, probably due to the increase of the hydrophilicity.

2.4.3 Formation of TiO_2 using atomic layer deposition (ALD)

A home built-up atomic layer deposition system was used for the deposition of thin and compact TiO_2 layers on the silicon nanostructures. For 18 nm TiO_2 layers, subsequent injection of MilliQ (18.2 MΩ-cm) H_2O and 99.995 % $TiCl_4$ (for 10 ms each) took place in a vacuum chamber with a delay of 18 sec between each injection. The samples were heated by a copper stage at 100 °C. The base pressure of the system was $< 5 \times 10^{-2}$ mbar. The pressure during deposition was adjusted to 1.1 mbar using an N_2 purging flow to remove the formed gases and excess precursors. Post annealing of the samples in a tube oven, in air, at 350 °C for 3 h with a ramp of 11 °C/min was needed for formation of anatase TiO_2 (Figure 2.6).

2.4.4 Photoelectrochemical deposition

For the deposition of platinum nanoparticles a photoelectrochemical cell (Zahner Scientific Instruments, PECC-1, slightly modified) made from Teflon was used (Figure 2.12). The cell has 3 inputs for the 3 different electrodes (working, reference and counter). Only a small area (0.3 cm^2) of the working electrode (i.e. sample) was in contact with the electrolyte, which was illuminated through a quartz window. The electrolyte consisted of an aqueous solution of chloroplatinic acid (4 mM) and Na_2SO_4 (0.1 M), while the pH was adjusted to 11 with 2 M NaOH. The back contact of the sample consisted of 4 nm of chromium (Cr) and 50 nm of gold (Au) deposited with a double target sputter coater (Leica EM ACE600).The electrical connections of the sample with the potentiostat (BioLogic Science Instruments, SP-200) were made using conductive aluminum tape (Advance Tapes AT521) adhered on the back metal contact of the sample, which was not in contact with the elec-trolyte.

2.4.5 X-ray photoemission spectroscopy (XPS)

X-ray photoemission spectroscopy (XPS) was performed in a home-built ultrahigh vacuum chamber, operating at a base pressure below 5×10^{-9} mbar. A XM1200 monochromatic x-ray source (Al α-K line, Scienta Omicron) was used for x-ray excitation of the sample under a 45° angle. Photoemitted electrons were collected using a HIPP-3 analyzer (Scienta Omicron). A polished platinum pellet (99.99 %, Kurt J. Lesker Company) was used for acquiring a Pt reference spectrum. Spectra were charge corrected using the binding energy of 1s carbon (284.8 eV).

2.4.6 Supplementary figures

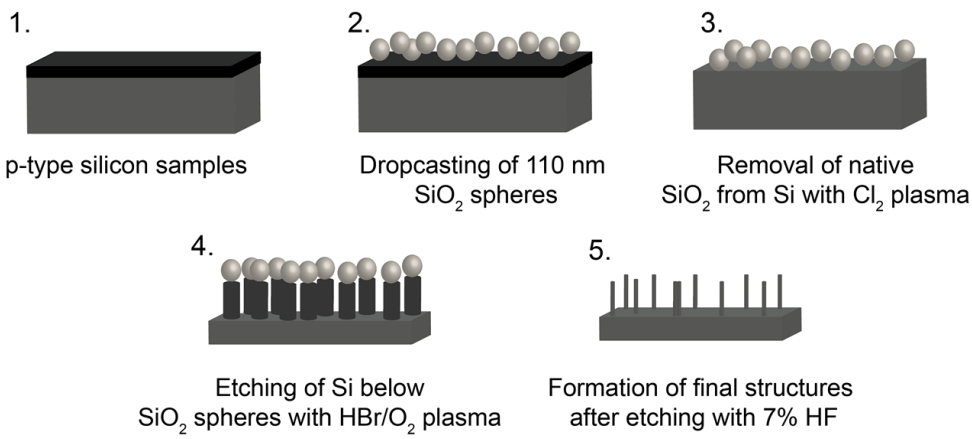

Figure 2.5. Description of the process steps for the preparation of silicon nanostructures with plasma etching.

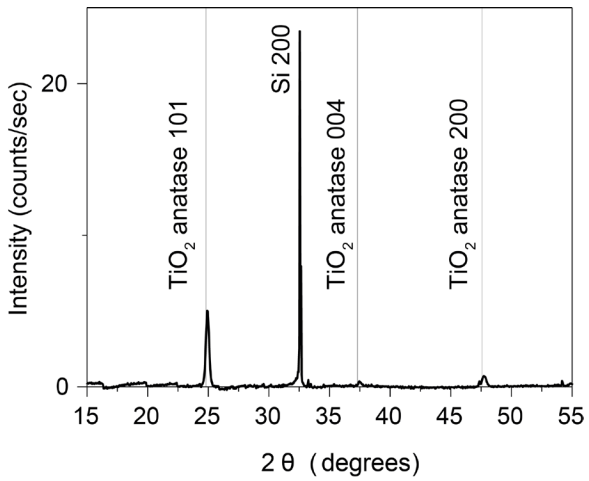

Figure 2.6. XRD data from an annealed TiO_2 layer of around 54 nm on a p-type silicon substrate. Anatase reference peaks (JCPDS Card no. 21-1272) shown as grey lines.

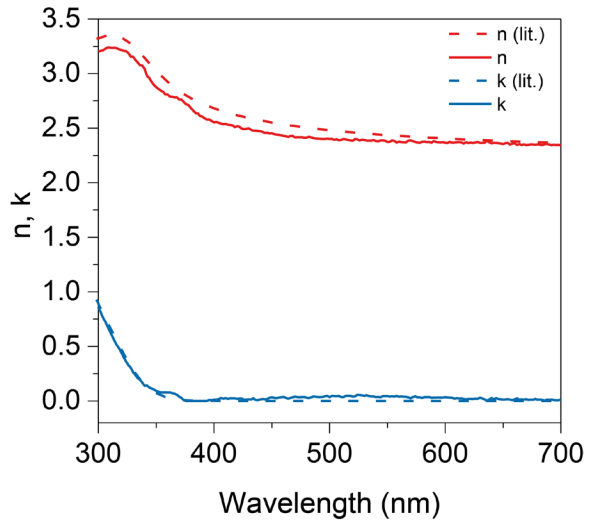

Figure 2.7. Optical constants retrieved from ellipsometry measurements on 18 nm TiO_2 prepared with ALD on a flat p-type silicon substrate and subsequent annealing for 3 h at 350 °C.[150]

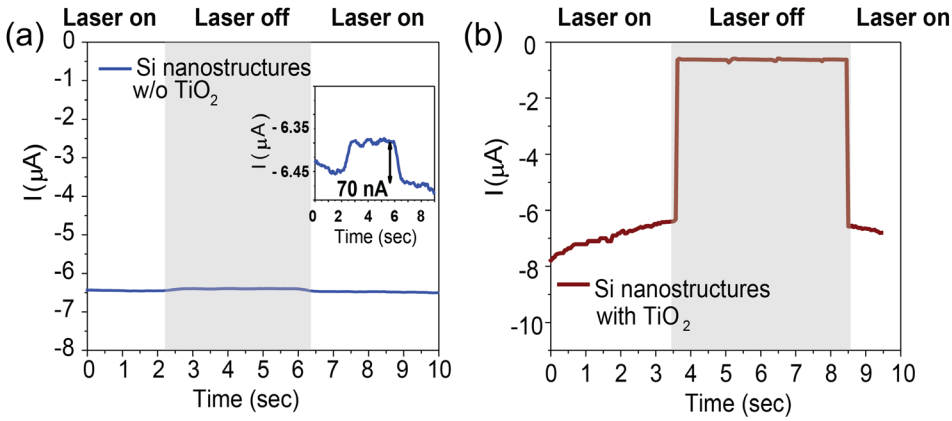

Figure 2.8. Chronoamperometry measurements of a silicon nanocone sample at an applied potential of −0.5V vs Ag/AgCl and illuminated at 532 nm (when "Laser on") a) uncoated, the inset image indicates a zoom-in view of the graph to emphasize the photocurrent of the sample (70 nA) and b) coated with a 18 nm TiO_2 layer.

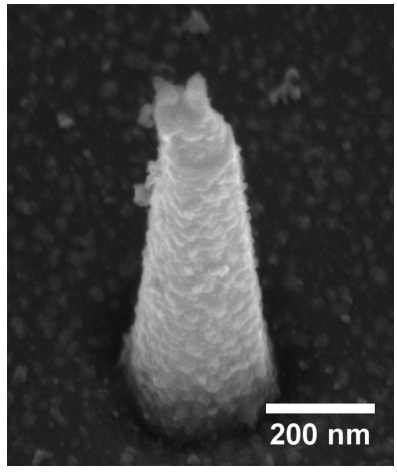

Figure 2.9. SEM image of a silicon nanocone after photo-electrodeposition at 532 nm without TiO_2 coating and fully covered with platinum nanoparticles.

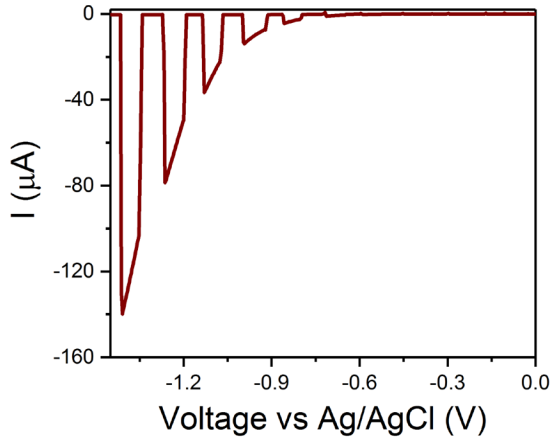

Figure 2.10. Current versus applied potential (vs Ag/AgCl reference electrode) plot of a silicon nanocones sample, coated with 18 nm TiO_2 and excited at 638 nm, with a light beam chopper to show the difference between the dark current and the photocurrent. The excitation took place in presence of H_2PtCl_6 (pH 11, 4 mM). The scan rate was 50 mV/sec. The coverage of this sample with Si nanostructures is different than the one of Figure 3b and this also explains the much less photocurrent observed here ($\sim$ 4 μA) at -0.8V. The more the coverage of the samples, i.e. the higher the amount of nanostructures excited, the higher the photocurrent.

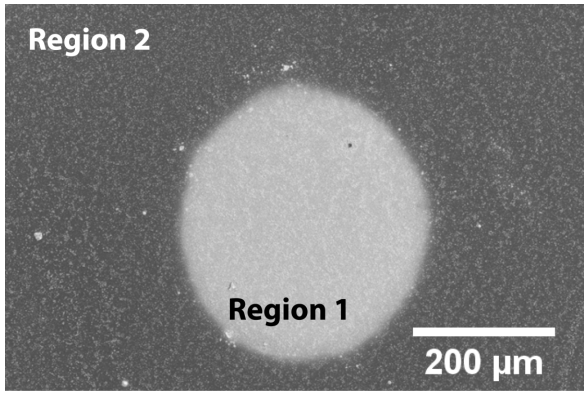

Figure 2.11. SEM image of the illumination spot (Region 1; λ_{exc} = 532 nm) on a silicon nanostructures sample. Region 2 is outside of the illumination area and only the small electrodeposited nanoparticles (<6 nm, see main text) were identified there. Both regions (Region 1 and 2) were in contact with the electrolyte and the bright area corresponds to the diameter of the laser beam as well as to the area where platinum particles are deposited.

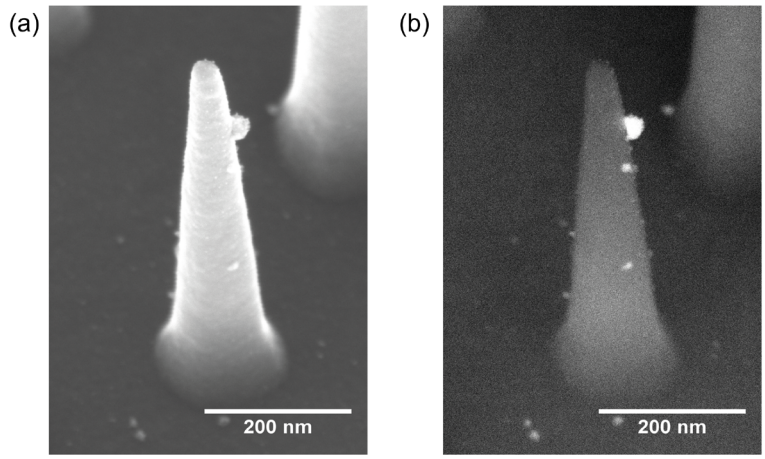

Figure 2.12. Secondary electron (a; through-the-lens detector) and backscattered electron (b; in-lens mirror detector) SEM images for a silicon nanocone after photoelectrodeposition of platinum from the illuminated region (Region 1 from Figure 2.11).

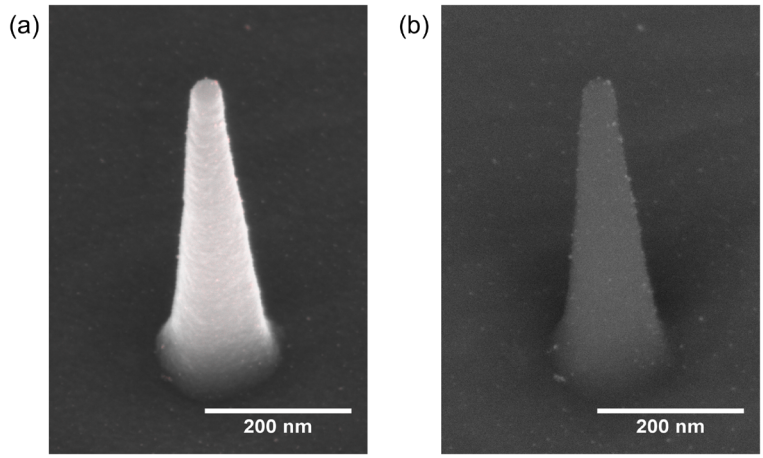

Figure 2.13. Secondary electron (a; through-the-lens detector) and backscattered electron (b; in-lens mirror detector) SEM images for a silicon nanoconeout the illuminated region. Only few and very small nanoparticles (diameter (D) $\sim$ 6 nm) are observed outside of the illumination spot (Region 2 from Figure 2.11), which are the result of electrodeposition.

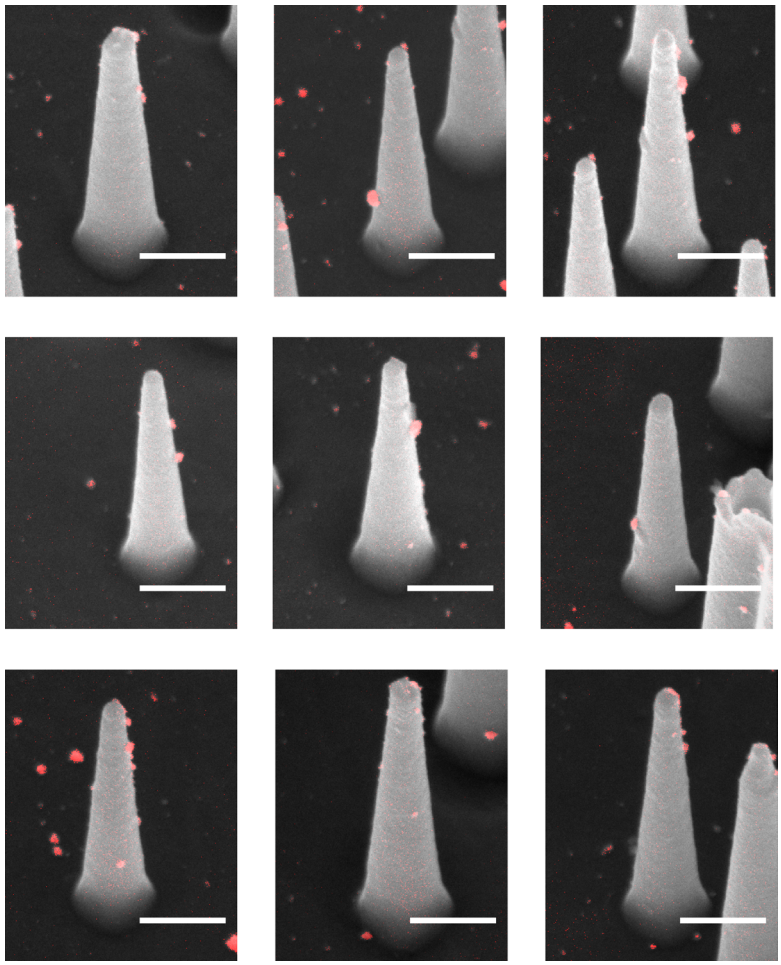

Figure 2.14. Overlays of secondary electron (grey color; through-the-lens detector) and backscattered electron (red color; in-lens mirror detector) SEM images of silicon nanocones after photo-electrodeposition of platinum nanoparticles at 532 nm. Scale bar = 200 nm.

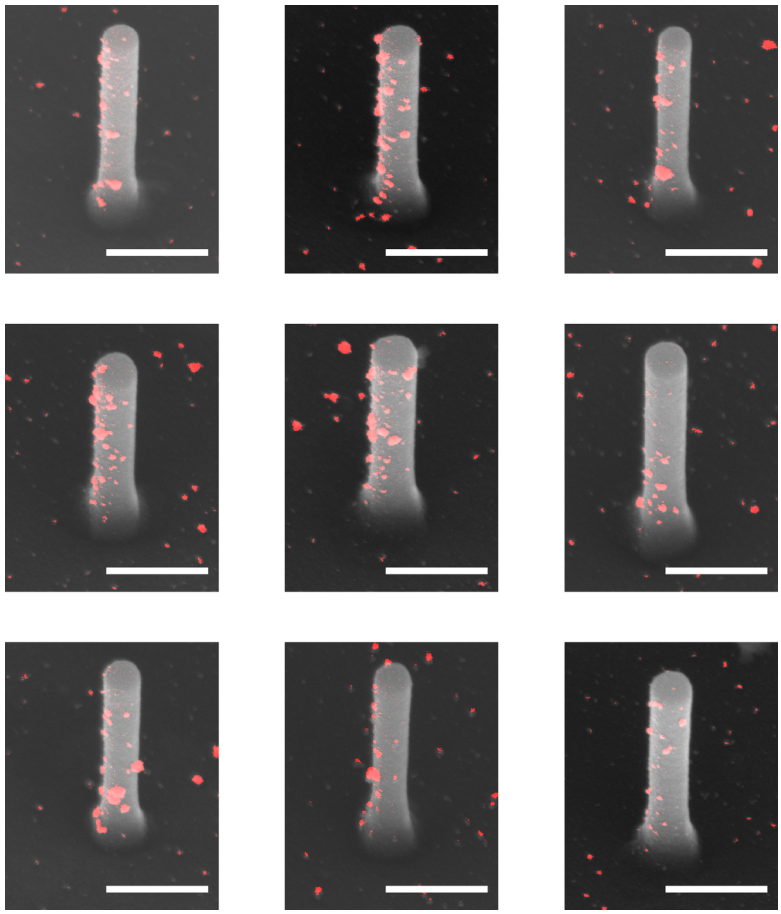

Figure 2.15. Overlays of secondary electron (grey color; through-the-lens detector) and backscattered electron (red color; in-lens mirror detector) SEM images of silicon nanowires after photo-electrodeposition of platinum nanoparticles at 532 nm. Scale bar = 200 nm.

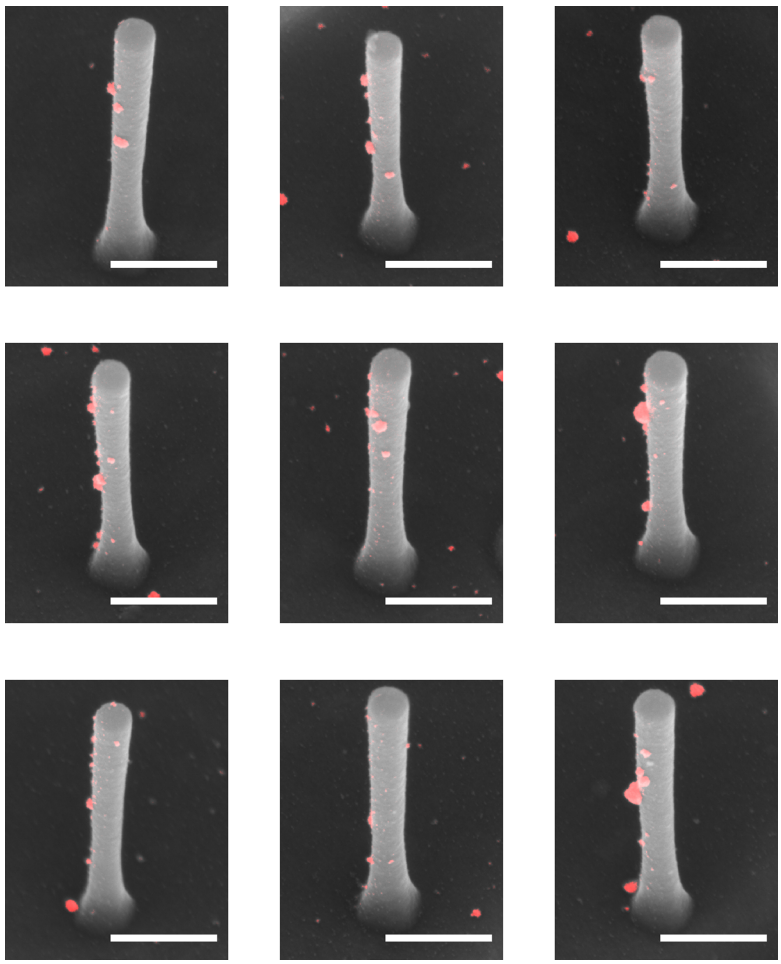

Figure 2.16. Overlays of secondary electron (grey color; through-the-lens detector) and backscattered electron (red color; in-lens mirror detector) SEM images of silicon inverted nanocones after photo-electrodeposition of platinum nanoparticles at 532 nm. Scale bar = 200 nm.

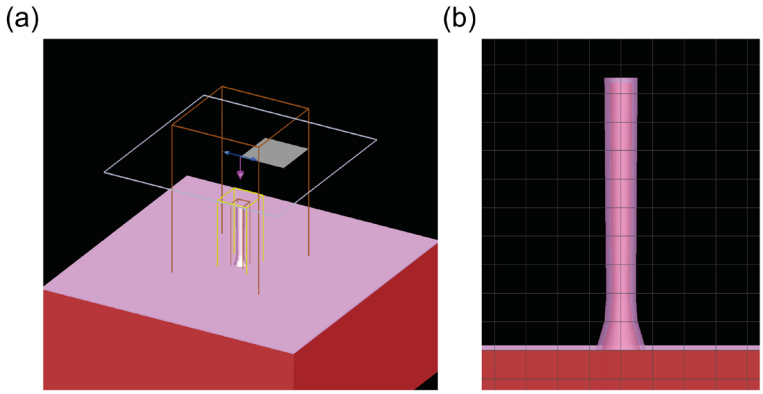

Figure 2.17. a) Simulating schematic diagram of the FDTD simulations for a silicon nanocone coated with 18 nm TiO_2 (shown with pink color) on a silicon substrate excited with a plane wave source (blue/pink arrows). The absorbed power per volume monitor is indicated as a yellow box. b) Zoom in on the simulated silicon nanostructure. The construction of the shape of the inverted nanocone, is the result of a combination of 3 components (3 cones) so as the shape and the dimensions of the structure to correspond to the average ones of the inverted nanocones examined on the samples.

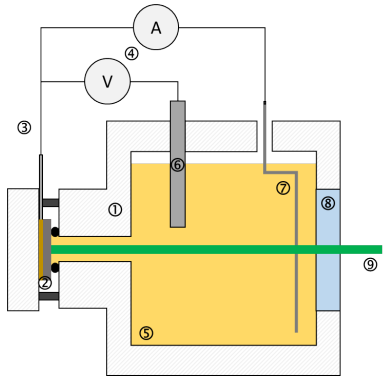

Figure 2.18. Detailed setup for electrodeposition of Pt on silicon nanostructures. 1) Photoelectrochemical cell made from PTFE, 2) Sample (silicon) with Au/Cr back contact, 3) Electrical connection of the back contact of the sample with the potentiostat and the reference electrode through a conductive aluminum tape, 4) Electrical connection of the back contact of the sample with the counter Pt electrode through the potentiostat, 5) Electrolyte (H_2PtCl_6 in 0.1 M Na_2SO_4), 6) Reference Ag/AgCl electrode, 7) Counter electrode (Platinum wire), 8) Quartz window, 9) Laser beam (532 nm).

3

Self-optimized catalysts: Hot-electron driven photosynthesis of catalytic photocathodes

Photogenerated hot-electrons from plasmonic nanostructures are very promising for photocatalysis, mostly due to their potential for enhanced chemical selectivity. Here, we present a self-optimized fabrication method of plasmonic photocathodes using hot-electron chemistry, for enhanced photocatalytic efficiencies. Plasmonic Au/TiO_2 nano-islands are excited at their surface plasmon resonance to generate hot-electrons in an aqueous bath containing a platinum (cocatalyst) precursor. Hot-electrons drive the deposition of Pt cocatalyst nanoparticles, without any nanoparticle functionalization and negligible applied bias, close to the hot-spots of the plasmonic nanoislands. The presence of TiO_2 is crucial for achieving higher chemical reaction rates. The $Au/TiO_2/Pt$ photocathodes synthesized using hot-electron chemistry show photocatalytic activity up to 2 times higher than a control made with random electrodeposited Pt nanoparticles. This light-driven positioning of the cocatalyst close to the same positions where hot electrons are most efficiently generated and transferred represents a novel and simple method for synthesizing complex, self-optimized photocatalytic nanostructures with improved efficiency and selectivity.

3.1 Introduction

Plasmonic nanoparticles can offer alternative pathways for driving chemical reactions compared to common semiconductors. The light-controlled selectivity over chemical products on plasmonic nanoparticles make them interesting for photocatalysis.[109, 157–159] The different reactivity from standard thermal catalysis is thought to arise from highly energetic, "hot" electron-hole pairs formed upon plasmonic excitation and decay.[20, 127, 160] Excitation of the plasmonic nanoparticle at the resonant wavelength results in the collective coherent oscillation of conduction band electrons with a concomitant enhancement of the electric field at specific hotspots. At these hotspots, the plasmon excitation can decay via Landau damping and thereby excites a single electron to create a highly-energetic electron-hole pair which is initially out of thermal equilibrium with the surroundings, i.e. "hot".[51, 161, 162] Hot carriers from plasmonic nanoparticles have so far been used for reduction of chemisorbed p-nitrothiophenol[161] or aryl diazonium salts,[163] oxidation of citrate,[164] hydrogen production,[165–168] and conversion of CO_2 to formic acid.[169]

Plasmon driven photoelectrochemical reactions seem very promising, but the recorded efficiencies are still too low for practical use. This low efficiency is mostly due to the short hot-carrier lifetime (<3 ps for Au or Ag nanoparticles).[107, 170, 171] Higher efficiencies have been reached by bringing the metal nanostructures in contact with an appropriately chosen semiconducting layer, allowing for rapid hot electron extraction and reduced recombination via a Schottky barrier.[51, 58, 168, 171–175] Similarly, hot holes can be extracted with a hole-transfer layer such as nickel oxide,[167] to leave the electrons on the structure. However, hot carrier extraction alone is often not sufficient; cocatalytic nanoparticles are necessary to achieve high efficiencies in almost all photoelectrochemical processes. Ideally this cocatalyst has the lowest possible loading, both to reduce the amount of costly precious metals such as platinum and rhodium, as well as to minimize reflection and parasitic absorption of incident light. Furthermore, it should be optimal to localize the cocatalyst only near the plasmonic hotspots, where hot electrons are generated most efficiently and catalysis is driven most favorably.[176–179] Nevertheless, there are few practical, low-cost and efficient techniques to position a cocatalyst with such nanoscale precision. For instance, Mubeen et al.[168] demonstrated fully autonomous plasmonic water splitting with an Au nanorod device with two individually deposited cocatalysts. However, the fabrication techniques dictated the localization of both cocatalyst, which does not necessarily imply an optimal spatial configuration, i.e. the hotspots and cocatalyst sites are potentially mismatched.

Here we propose a self-optimized fabrication strategy, where hot-electrons are used both for the localized deposition of cocatalyst nanoparticles and the subsequent photocatalysis (Figure 3.1). Our approach removes the need for lithographic patterning of either the plasmonic nanoparticles or cocatalyst, while simultaneously allowing for the ideal spatial distribution at any given loading. We used random Au plasmonic

nano-islands on ITO coated with TiO_2 as the plasmonically active substrate. Both the deposition of Pt cocatalyst nanoparticles from solution and the subsequent photocatalysis were conducted under 638 nm illumination (within the plasmonic absorption peak). By comparing the photocatalytic performance of our self-optimized photodeposition method to that from random electrodeposition (with identical loading and dark current characteristics), we see up to a factor of 2 increase in efficiency of photocatalysis.

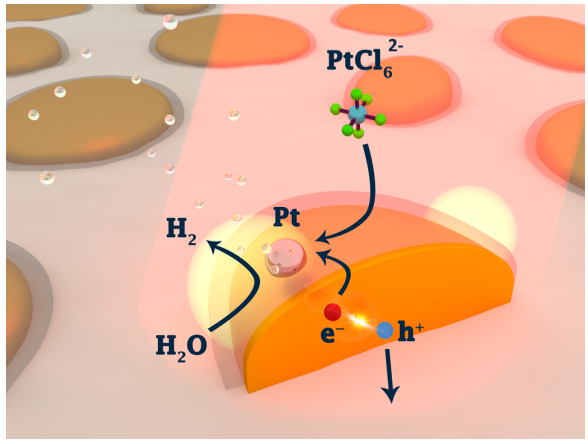

Figure 3.1. Schematic illustration of the self-optimized catalysts. i) Hot-electrons and hot-holes are created in Au/TiO_2 nano-islands after excitation at 638 nm, ii) hot-electrons reduce hexachloroplatinate at the plasmonic hot-spots (light yellow areas) to form platinum nanoparticles (cocatalyst) and iii) hot-electrons reach the newly formed platinum nanoparticles and accelerate hydrogen production at the same excitation wavelength.

3.2 Results and discussion

Plasmonic Au nano-islands were prepared on ITO-covered glass slides with the aim of using them as absorbing platforms for the selective hot-electron driven deposition of the cocatalytic nanoparticles. It has already been shown that this type of sample is photocatalytic and can also support hot-spots.[46, 167] Briefly, an 8 nm gold film was sputtered-coated on ITO substrates and subsequently annealed at 300 °C for 1 hour to spontaneously form Au nano-islands (Figure 3.2a). The nano-islands were coated with a thin TiO_2 layer with atomic layer deposition (ALD), which acts as a hot-electron filter prohibiting recombination of the photogenerated charges in the metal by providing a high density of electron-accepting states.[180] X-ray diffraction (XRD) showed that the TiO_2 layer had crystallized in the anatase phase (Figure 3.8) after annealing, which

has been shown to be favorable for accepting hot electrons compared to rutile or amorphous TiO_2.[181] SEM images (Figure 3.2a) and AFM maps (Figure 2b) showed final structures (Au/TiO_2) with a mean largest diameter of 151 ± 56 nm and a mean height of 44 ± 8 nm (Figure 3.9). Overlays of secondary electron and backscattered electron SEM images (Figure 3.2c and Figure 3.10) revealed the presence of a 18 ± 2 nm TiO_2 layer around the gold nano-islands the thickness of which was further confirmed by size distribution measurements before and after the ALD step (Figure 3.2d and Figure 3.11) and ellipsometry data (Figure 3.7). The chosen TiO_2 thickness arose from preliminary results for optimization of the photocurrent of our system (see below).

Absorption spectra showed a strong plasmonic peak of the Au/TiO_2 structures centered between 640 – 700 nm, depending on small sample thickness differences (Figure 3.2e), which is an ideal wavelength range for the generation of hot electrons, as plasmonic excitations below 600 nm are strongly dampened by interband transitions in bulk Au.Au.[182, 183] The size distribution of the nano-structures could strongly affect the surface plasmon resonance of the final samples and could be easily tuned by altering the thickness of the sputter-coated Au film. The size distribution chosen here gave a resonance far from the interband transition wavelength region but still in a high electron energy range. A redshift and a broadening of the absorption peak of the Au nano-islands was observed (Figure 3.12) after the addition of TiO_2, which can be attributed to the higher embedding refractive index and possibly also to increased interparticle coupling.[46, 184] The TiO_2 layer has negligible optical absorption at 638 nm with an onset of bandgap absorption in the ultraviolet, as expected (Figure 3.7). When deposited on ITO there is some parasitic absorption, but this is far below ($\sim$ 9 times) that of the plasmonic nano-islands (Figure 3.12) and does not contribute significantly to photocurrent (Figure 3.13). The Au-TiO_2 nano-islands were easily prepared on bulk scale and were suitable for studying hot-electron photoreactions with red light.

The ability of Au/TiO_2 nano-islands to generate hot-e^- which can drive a chemical reaction for the synthesis of cocatalytic nanoparticles was investigated. The nano-islands were excited by a 638 nm laser beam (0.5 W/cm^2) in a three-electrode photoelectrochemical cell under potentiostatic control using a Ag/AgCl reference electrode. The current flow from the sample (working electrode) to a platinum wire (counter electrode), was recorded in presence of an aqueous platinum precursor (0.04 mM H_2PtCl_6 in 0.1 M Na_2SO_4, pH 3, deoxygenated). At open circuit voltage conditions (OCV = 470-580 mV vs RHE), very little photocurrent was observed but sweeping the potential to more negative values increased the Pt photodeposition rate (Figure 3.13c). 3.3a shows a typical current density vs time curve of the Au/TiO_2 nano-islands both under 638 nm light illumination (laser on) and in the dark (laser off) at 450 mV vs. RHE. While the dark current was negligible throughout the whole measurement, the photocurrent gradually increased as a function of time (t = 30-55 s and 55-65 s, Figure 3.3a). Furthermore, almost no photocurrent (16 nA/cm^2, 40-1000 times lower than Au/TiO_2 samples) was recorded from bare TiO_2 (Figure 3.13), indicating that the photoactivity comes from plasmonic absorption in the Au and hot-electron photoreduction. In our approach, cur-

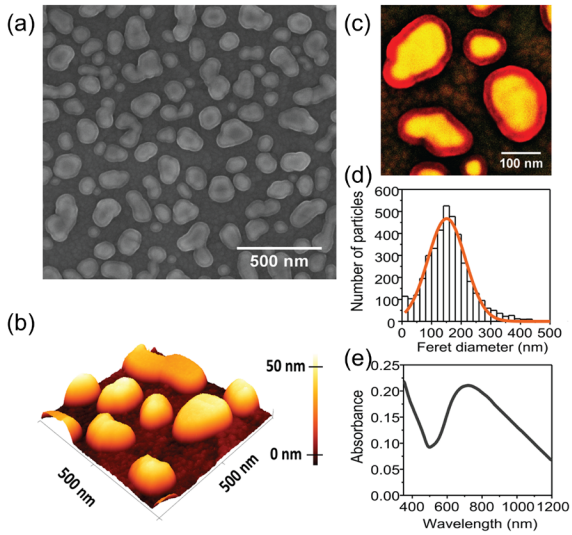

Figure 3.2. Characterization of Au/TiO_2 nano-islands on ITO/glass substrate. a) SEM image, b) AFM map, c) overlay of backscattered (yellow) and secondary electron (red) images where the strong contrast between TiO_2 and Au nano-islands originates from the lack of electron backscatter by the lighter elements of the TiO_2 shell, d) size distribution of Au/TiO_2 nano-islands after SEM imaging analysis with a fitting Gaussian curve (orange solid line) and e) absorbance spectrum.

rent measurements are retrieved from the whole photoelectrode, a bulk method that has already been used as evidence for hot-electron flow.[167, 168, 185] Single nanoparticle photocurrent measurements have also confirmed that the presence of photocurrent at the surface plasmon resonance of the nanostructure is related to the flow of hot-carriers.[186]

SEM images showed that after an electrical charge of 125 $\mu C/cm^2$ was passed to the sample, new nanoparticles appeared on the Au/TiO_2 samples (bright clusters, Figure 3.3b). The newly formed nanoparticles corresponded to a mixture of Pt(II)/Pt(IV) salts/oxides according to XPS (Figure 3.14) and EDX measurements (Figure 3.15), so they were further reduced by a "photoconditioning" step and using again hot-electron chemistry. During this step, the platinum containing electrolyte was exchanged with an aqueous phosphate buffer to avoid further deposition of Pt species and the sample was irradiated for 25 s at 638 nm (0.5 W/cm^2) at an applied potential of -250 mV vs. RHE (Figure 3.16). After the photoconditioning procedure, the observed platinum $4f_{7/2}$ and $4f_{5/2}$ binding energy peaks matched a metallic Pt reference (Figure 3.3c), indicating that the reduced particles consisted mainly of metallic platinum, favorable for catalyzing many chemical reactions.[187] The fact that the initial photoreaction did not produce any metallic Pt may be ascribed to Pt^{4+} kinetically outcompeting Pt^{2+}

species for hot electrons. However, photoconditioning at the same potential as the initial photodeposition step (450 mV) did not result in Pt^0 nanoparticles. This indicates that it is the extra potential that is crucial for the full reduction of Pt species. Apparently, hot electrons that have been injected in the TiO_2 conduction band do not possess sufficient reducing power to fully reduce hexachloroplatinate to metallic platinum. These results mirror those from Xi et al.[188] who have shown that the electrochemical reduction of hexachloroplatinate leads to mixed valence materials. More reducing potentials (than −250 mV vs. RHE) were avoided during the photoconditioning step, because then the distinction between hot electron mechanism and bare electrochemical reduction of Pt species would be difficult. As a result, the photocurrent measured in the Au/TiO_2 nano-islands could eventually be correlated with the deposition of Pt nanoparticles.

We thus examined the correlation of the photocurrent generation (i.e. the hot-electron production) with the absorptance of the Au plasmonic nano-islands. Au nano-islands coated with TiO_2 were excited at different wavelengths (440-760 nm, with 20 nm step) with a supercontinuum laser, while the current was recorded (Figure 3.17) in presence of hexachloroplatinate. The Incident Photon to Current Efficiency (IPCE) was calculated (see SI for more information) for every excitation wavelength and plotted together with the absorptance spectrum of the same sample as a function of the wavelength (Figure 3.18). The results show that there is a good correlation between the absorptance of the Au nano-islands and the IPCE values, except for in the blue region (440-500 nm). Seemingly, photogenerated electrons resulting from interband transitions (high energy electrons) barely participate in the photoreduction of hexachloroplatinate. This is reasonable since these electrons are excited from d band levels to energy levels close to or below the Fermi-level of Au.[171] These electrons therefore do not have enough energy to surpass the Au/TiO_2 Schottky barrier and contribute to the generation of photocurrent. So, apparently only hot-electrons with energy high enough to be injected to the conduction band of TiO_2 can reach the hexachloroplatinate molecules and reduce them to Pt species.

The plasmonic excitation of Au nano-islands clearly leads to Pt nanoparticle formation, but in order to further confirm this occurs via a hot-electron mechanism, we have conducted several control experiments. The most obvious alternative explanation is a simple heating effect. The large increase in photocurrent after the addition of TiO_2 (Figure The plasmonic excitation of Au nano-islands clearly leads to Pt nanoparticle formation, but in order to further confirm this occurs via a hot-electron mechanism, we have conducted several control experiments. The most obvious alternative explanation is a simple heating effect. The large increase in photocurrent after the addition of TiO_2 (Figure 3.3a and Figure 3.13), as well as the correlation between the absorptance and IPCE spectra (Figure 3.18) already point toward a hot-electron rather than thermal mechanism. Hot-electrons with energy high enough to overcome the Schottky barrier are transferred into the TiO_2 layer, where the barrier reduces the chances of back-transfer and recombination, increasing the efficiency of Pt formation (Figure 3.3d). The improved yield of Pt with the addition of TiO_2 alone cannot completely rule out a thermal

effect, since hexachloroplatinate molecules bind much better to the TiO_2 surface than on Au, which allows for suitable electron acceptors being always present as the hot electron arrives at the TiO_2/H_2O interface.[181] However, the better surface binding cannot explain the correlation between the absorption and IPCE spectra described above. Additionally, the photocurrent showed a linear dependence on laser intensity over a range of two orders of magnitude (Figure 3.19), consistent with a hot-electron mechanism and inconsistent with laser heating.[160, 185] The temperature on the surface of the sample was measured with a FLIR thermal camera (Figure 3.20) during irradiation at 638 nm (0.5 W/cm^2) and reached up to 30 °C. As a follow up control test, we conducted dark heating experiments and saw no Pt nanoparticle formation at 40 °C even after 20 minutes (Figure 3.21), showing that thermal decomposition is not playing a role in our experiments.

The observed photocurrent density increase as a function of time during the photoelectrodeposition of Pt on the Au/TiO_2 nano-islands (Figure 3.3a) can be explained by the presence of the first atoms of Pt formed on the surface of TiO_2 acting as electron-sinks and enhancing the reaction rate.[154] The sudden current transient ("spikes" at 30 and around 55 sec, Figure 3.3a) every time the laser is switched on could be the result of charge recombination at the electrode/electrolyte interface. As a function of time the amplitude of the current transients seems decreased ($\sim$ 55 sec) and this could be correlated with the presence of the first Pt atoms, which reduce the charge recombination and improve the separation of the hot-electrons from the hot-holes.[189] The correlation between plasmonic hot-spots and Pt deposition sites was unfortunately very challenging to be investigated because the hot-spots were not very well-defined; FDTD simulations of the three-dimensional AFM-deduced structures (without Pt deposits) showed that the hot-spots on this type of nanostructures are generally spread out across large distances around the nanoparticle edges (Figure 3.22 and Figure 3.23). In Figure 3.3b, some Pt nanoparticles form in areas between the Au nano-islands, where according to FDTD simulations no plasmonic hot-spots appear and the enhancement of the absorbed power is mostly observed on the Au nano-islands (Figure 3.22 and Figure 3.23). This indicates that hot-electrons injected into the TiO_2 layer can diffuse and form Pt nanoparticles somewhat removed from the plasmonic hot-spots, in contrast with previous reports where TiO_2 was not used.[190] Nevertheless, even in the case that hot-electrons are reaching the electrolyte and reduce hexachloroplatinate further from the actual hot-spots, the positioning of the cocatalyst can be still considered as optimal for the photocathode as a whole. Hot-electrons are created and then diffusing until they meet a site that supports an efficient transfer to the photoelectrode surface. After further illumination of the $Au/TiO_2/Pt$ photocathodes the new photogenerated hot-electrons will probably follow the same path as the first time to the electrolyte but now meeting the cocatalyst nanoparticles first. In that way the whole process is not limited by the exact characteristics of the TiO_2 film but lets any imperfections "work" in its favor.

To illustrate the photocatalytic behavior of the hot-electron driven prepared photocathodes ($Au/TiO_2/Pt_{photo}$), we performed current density versus potential (CV) scans

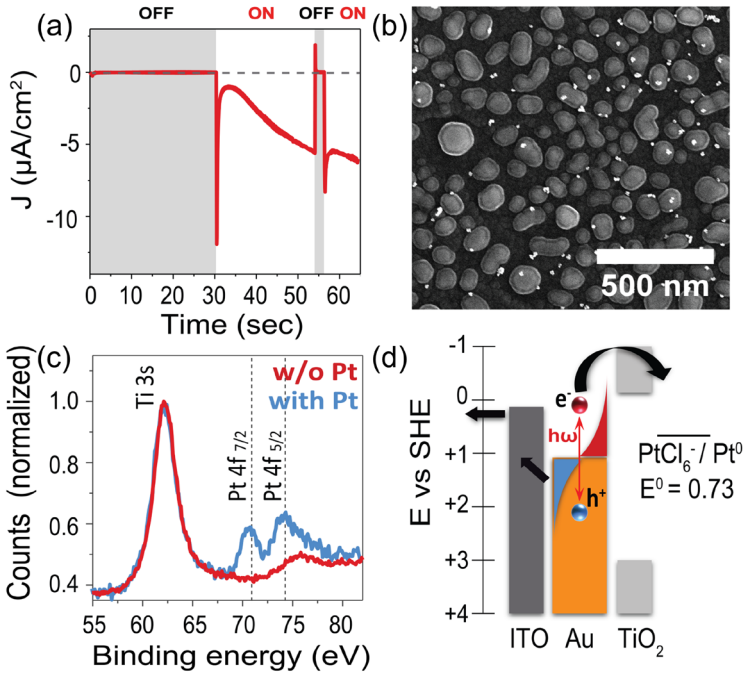

Figure 3.3. a) Current density vs time plot of Au/TiO_2 nano-islands in presence of hexachloroplatinate (pH 3, 0.04 mM in 0.1 M Na_2SO_4 aqueous solution, 450 mV vs. RHE), b) SEM image of Pt nanoparticles on Au/TiO_2 nano-islands after illumination of the latter at 638 nm (0.5 W/cm^2) in hexachloroplatinate and recording of 125 $\mu C/cm^2$ of electrical charge from the sample, c) X-Ray photoemission spectrum of the samples before (light blue line) and after photoelectrodeposition of Pt nanoparticles (red line). Dashed lines indicate literature values for metallic Pt $4f_{7/2}$ and $4f_{5/2}$ binding energies.[191] d) Simplified band diagram of Au/TiO_2 nano-islands on ITO and flow of hot electrons and holes during the photo-electrodeposition process.

in presence of an aqueous phosphate buffer (0.1 M, pH 7, de-oxygenated). The current flow of the $Au/TiO_2/Pt_{photo}$ samples was recorded under chopped illumination at 638 nm while sweeping the electrochemical potential of the working electrode to more negative (reducing) values (Figure 3.4a and Figure 3.4b, blue solid line). The CV scan shows an increase of the current density under illumination (laser on), which becomes higher towards more negative potentials. The dark current (laser off) remains negligible (130 times lower than the photocurrent) until an applied potential of around −0.35 V vs RHE, where it starts increasing rapidly. The difference between onset potential of photo and dark current can be explained by the Schottky barrier between Au and TiO_2. The more negative the applied potential, the smaller the Au/TiO_2 Schottky barrier, due to

the shift of the Fermi level of Au towards the vacuum level and the conduction band of TiO_2.[192] In absence of light, the Au/TiO_2 Schottky barrier does not allow electrons to flow from Au to TiO_2 and drive the chemical reaction, so almost no current is recorded until the Fermi level of Au equalizes with the conduction band of TiO_2 at -0.3V vs RHE. Assuming a Fermi-Dirac hot-electron distribution in the Au nanoparticles under illumination,[20] more electrons will have high enough energy for transfer to the TiO_2, increasing the photocurrent. Control measurements were also conducted on bare TiO_2 as well as Au/TiO_2 to investigate performance without the cocatalyst and plasmonic light absorber, respectively. CV scans on both of these configurations (Figure 3.4a and Figure 3.4b, black and green solid line respectively) revealed that the recorded photocurrent was 1000 and 30 times lower, for TiO_2 (4 nA) and Au/TiO_2 (140 nA) respectively, than for the $Au/TiO_2/Pt_{photo}$ samples at 0 V versus RHE. This proves that both the plasmonic absorber and cocatalyst play key roles in the photocatalytic behavior. Considering the potential onset of the photoreduction reaction and the species available in solution, water reduction to hydrogen is the most likely photochemical reaction product.

In order to test the self-optimized behavior of our approach, we investigated if our method of preparing photocathodes with hot-electron injection performs better in photocatalysis than a common electrodeposition method of depositing the cocatalyst (see SI for more details) under the same conditions. In order to warrant a valid comparison, we carefully controlled the electrodeposition conditions to achieve samples with an identical amount of platinum, with the same morphology and oxidation state, verified by ICP-MS, XPS and SEM (Table 3.2, Figure 3.24, Figure 3.4c and Figure 3.4d). CV scans (Figure 3.4a and Figure 3.4b, blue and red solid lines) showed that when we let the plasmonic nanostructures decide where the cocatalyst will be deposited (i.e. hot-electron deposition, $Au/TiO_2/Pt_{photo}$), the photocurrent density was higher (up to 2 times) than when the cocatalyst was randomly electrodeposited ($Au/TiO_2/Pt_{electro}$), especially at small applied potentials. This suggests that the localization of the cocatalyst close to the hot-spots of the plasmonic photocathodes, where the hot-electrons reach the photocathode/electrolyte interface, promotes the chemical reaction. The positioning of the cocatalyst exactly on the pathway of the photogenerated hot-electrons towards the electrolyte could contribute to the better utilization of the hot-electrons participating in the chemical reaction. In case of a random cocatalyst distribution on the plasmonic photocathodes, the hot-electrons will have to diffuse further than their original path to find the cocatalyst. During this additional diffusion the probability of their recombination with the respective hot-holes, remaining in the gold, is increased. The potential dependence of the photocurrent varied somewhat from sample to sample (Figure 3.4a, Figure 3.25 and Figure 3.26), suggesting that the hot electron energy distribution is sensitive to the exact Au nano-island geometry and/or differences on the TiO_2 surface. Therefore only samples which had exactly the same amount of deposited platinum (retrieved from XPS data) and the same dark current (see CV scans for photo-electrodeposited and electrodeposited samples, Figure 3.25 and Figure 3.26) were compared. Further work trying to use this potential distribution to map out hot electron energy distributions is

ongoing.

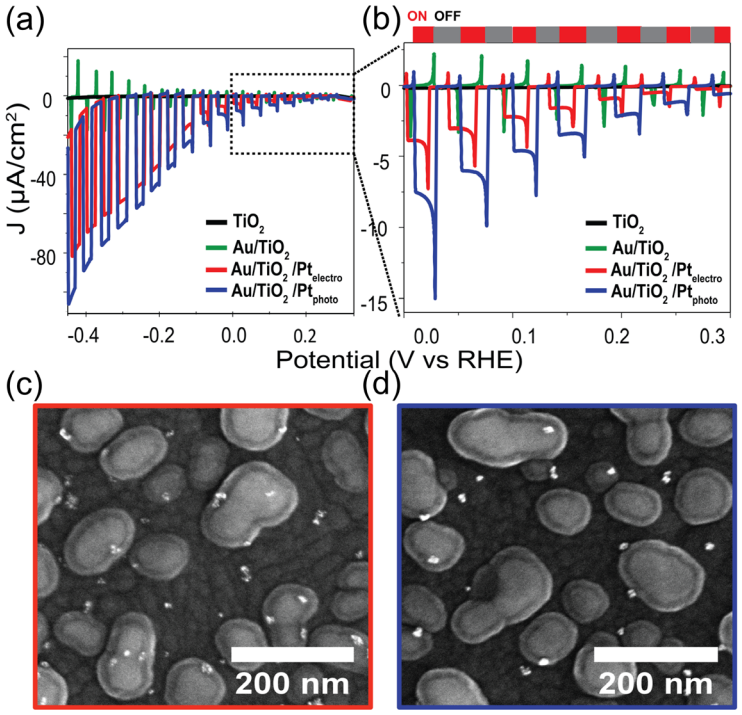

Figure 3.4. a) Current density vs potential plots of TiO_2 (black solid line), Au/TiO_2 nano-islands (green solid line), Au/TiO_2 nano-islands with randomly electrodeposited Pt nanoparticles ($Au/TiO_2/Pt_{electro}$, red solid line) and localized photoelectrodeposited Pt ($Au/TiO_2/Pt_{photo}$, blue solid line) in pH 7 phosphate buffer under chopped 638 nm illumination (0.5 W/cm^2). b) Zoom-in of plot a) at low applied potentials (0.0-0.3 V vs RHE). c) and d) SEM images of $Au/TiO_2/Pt_{electro}$ and $Au/TiO_2/Pt_{photo}$ photocathodes respectively.

3.3 Conclusions

In summary, we demonstrate a lithography-free method for creating plasmonic photocathodes with cocatalyst nanoparticles placed selectively at hot-electron generation sites. The plasmonic hot-spots on Au/TiO_2 nano-islands were used both to localize the Pt nanoparticle cocatalyst and to do photocatalysis. The presence of TiO_2 proved es-

sential for reducing recombination of hot carriers and led to higher photocurrent values. Besides providing a good hot-electron filter, the TiO_2 may also enhance binding of the Pt precursor molecules on its surface. We also showed that photocathodes with cocatalyst deposited using hot-electrons have better photocatalytic performance than those made with randomly placed electrodeposited Pt. This self-optimized photoelectrode strategy, where plasmonic nanostructures themselves determine the cocatalyst position, is a very promising route for simple fabrication of complex photocatalytic nanostructures that could lead to enhanced plasmonic solar fuel production.

3.4 Supporting information

3.4.1 General

Chemicals were purchased from major chemical suppliers and used as received. Sample characterization was done with Scanning Electron Microscopy (FEI Verios 460, acceleration beam voltage 5 kV, beam current 100 pA), X-Ray Diffraction (Bruker D2 Phaser, Cu Kα-radiation, wavelength = 1.5418 Å) and Atomic Force Microscopy (Veeco Dimension 3100 AFM). X-ray photoemission spectroscopy (XPS) was performed in a home-built ultrahigh vacuum chamber, operating at a base pressure below 5×10^{-9} mbar. A XM1200 monochromatic x-ray source (Al α-K line, Scienta Omicron) was used for x-ray excitation of the sample under a 45° angle. Photo-emitted electrons were collected using a HIPP-3 analyser (Scienta Omicron). Spectra were charge corrected using the binding energy of 1s carbon (284.8 eV). A UV/Vis/NIR spectrophotometer (PerkinElmer, L750) was used for acquiring the absorbance spectra.

3.4.2 Preparation of Au nano-islands

Plasmonic Au nano-islands were prepared on ITO-covered glass slides (Figure 3.5) following a literature procedure.[167] 15 × 15 mm indium tin oxide (ITO) substrates (150 nm on glass) were cleaned with detergent, rinsed with demineralized water, acetone, isopropanol and dried in a stream of N_2. The substrates were placed in a sputter coater (Leica EM ACE600), where 8 nm of Au were sputtered with a rate of 0.35 nm/s, measured with a quartz crystal thickness monitor during sputtering. After deposition of the thin Au layer, the samples were placed in a tube oven, which was brought to 300 °C with 9.2 °C/min and kept at constant temperature for 1 h and subsequently allowed to cool down to room temperature. Atomic layer deposition of TiO_2 on Au nano-islands Atomic-layer deposition (ALD) of TiO_2 on Au nano-islands was conducted in a custom thermal ALD system developed in-house at 100 °C. The base pressure of the system was 0.03 – 0.07 mbar and during deposition the pressure was kept at 1.1 mbar with an influx of N_2. Each cycle of TiO_2 deposition consisted of injecting a 10 ms pulse of $TiCl_4$ vapor, waiting for 18 s, injecting a 10 ms pulse of H_2O vapor, and waiting another 18

s. The deposition rate was 0.4 Å per cycle. The TiO_2 thickness on Au nano-islands was estimated by depositing TiO_2 in parallel on a Si substrate and measuring the layer thickness by ellipsometry using a dielectric model of TiO_2 and native SiO_2 on a Si substrate. Typically, 300 cycles of TiO_2 (18 nm) were deposited on the Au nano-islands. For purpose of electrical connection (see below), a 2 mm strip of the substrates was masked with Kapton tape during ALD.

3.4.3 Photoelectrodeposition of Pt on Au/TiO_2 nano-islands

Photoelectrodeposition of platinum on Au/TiO_2 nano-island substrates was conducted in a three-electrode photoelectrochemical cell (PEC) connected to a potentiostat (Biologic, SP-200) (Figure 3.6). The Au/TiO_2 substrate (working electrode) was electrically connected to the potentiostat with a conductive aluminium tape (Advance Tapes AT521) on the top 2 mm of the substrate. A rubber ring (Ø 8 mm) was placed centrally on the Au/TiO_2 working electrode and this assembly was clamped tightly on a 6 mm hole on the outside of the electrochemical cell. Only the central 6 mm was thus in contact with the electrolyte. A leakless miniature Ag/AgCl electrode (Mengel Engineering ED-ET072) was used as reference electrode and a Pt wire was used as counter electrode. The electrolyte was prepared with 100 mM Na_2SO_4 and 4 mM H_2PtCl_6 in MilliQ water (18.2 MΩ.cm) and adjusted to pH 3.0 – 3.4 with aliquots of NaOH (2 M). The electrolyte was prepared at least 48 h in advance to allow hydrolysis of H_2PtCl_6, which has been found important for the deposition of Pt on TiO_2.[188] The PEC was filled with 8 mL electrolyte and the sample was illuminated from the back without interacting first with the electrolyte with a laser beam (0.5 W/cm^2). Meanwhile, the potential of the working electrode was kept constant (chronoamperometry mode), typically at + 0.25 V vs Ag/AgCl. After photoelectrodeposition, samples were rinsed with H_2O and dried with N_2.

3.4.4 Wavelength dependence measurements

Wavelength dependence measurements on Au/TiO_2 photocathodes were conducted in presence of hexachloroplatinate under the same conditions as the photoelectrodeposition of Pt using now a different light source (supercontinuum laser, Fianium WL-SC-390-3), which was made monochromatic using an acousto-optical tunable filter (AOTF-Crystal Technologies). The signal was read out from the potentiostat (Biologic, SP-200) after lock-in amplification (Stanford Research Systems SR830), while the transmission of the AOTF was digitally modulated at 70 Hz. The potential of the working electrode was kept constant (chronoamperometry mode), at + 0.25 V vs Ag/AgCl. The current measurement was started in the dark (beam was blocked manually) and every 20 sec was alternated between a different excitation wavelength and the dark.

3.4.5 IPCE calculation

The Incident Photon to Current Efficiency (IPCE) was calculated as follows:

$$IPCE(\%) = \frac{j_{\mathrm{ph}}(mA/cm^2) * 1241(V * nm)}{P(mW/cm^2) * \lambda(nm)} * 100$$

, where j_{ph}(mA/cm^2) is the average photocurrent retrieved from the Figure 3.17 for each wavelength, 1241 (V × nm) represents a multiplication of h (Planck's constant) and c (the speed of light) divided by q (the electron charge), P (mW/cm^2) is the power intensity of each wavelength measured with a Si photodiode power sensor (Thorlabs S120C, see Table 3.1 for more information, with surface area of the photoelectrode equal to 0.28 cm^2) and λ (nm) is the wavelength. The IPCE vs wavelength curve is compared with the absorptance spectrum of the same sample in Figure 3.18.

3.4.6 Electrodeposition of Pt nanoparticles

Random deposition of platinum nanoparticles was performed on the Au/TiO_2 photocathodes in presence of hexachloroplatinate (H_2PtCl_6, pH 3), using a pulsed electrodeposition method introduced by Liu et al.[193] Specifically, we used differential pulsed amperometry to control the sequence and the duration of the pulses sent to the sample. In absence of light, first a -0.6 V vs RHE potential was applied to the sample for 5 s. In sequence, the potential was changed to 0.6 V vs RHE and kept at this value for 25 s. This total period of 30 s is considered one cycle and the amount of deposited Pt was controlled by the number of cycles.

3.4.7 Photoconditioning

During this step, −0.25 V vs RHE were applied to the Pt/Au/TiO_2 samples in the 3-electrode photoelectrochemical cell in presence of a de-oxygenated (purged for 1 h with N_2) phosphate buffer (pH 7, 0.1 M). The duration of the photoconditioning step was 45 sec; the first 20 sec the sample was kept in the dark, followed by 25 sec of illumination with a 638 nm beam (0.5 W/cm^2).

3.4.8 Photocatalysis measurements on Au/TiO_2/Pt photocathodes

Photocatalysis measurements of the Au/TiO_2/Pt photocathodes were conducted in the same three-electrode photoelectrochemical cell as the photoelectrodeposition of Pt nanoparticles, but with a different electrolyte (phosphate buffer, pH 7, purged with nitrogen for 1 hour). The current flow from the samples was measured as a function of the potential with a scan rate of 20 mV/s, under 638 nm (0.5 W/cm^2) chopped illumination, with a chopping frequency of 25 Hz.

3.4.9 FDTD simulations of Au/TiO_2 nano-islands

Finite Difference Time Domain (FDTD) simulations were performed using the 3D Maxwell solver software package Lumerical. An AFM height map of Au/TiO_2 nano-islands (2x2 µm) was imported as a surface, which functioned as the TiO_2 layer. Optical constants retrieved by ellipsometry (Figure 3.7) were used for this layer. The bare Au nano-islands layer was retrieved from the same AFM height map by importing it in the 3D simulation program Blender and using the displacement modifier algorithm to mimic subtraction of the 18 nm conformal TiO_2 layer. The resulting Au nano-island height map was exported, interpolated to uniform x-y spacing using Origin Software, and imported in Lumerical as surface to function as the Au layer. Finally, an ITO substrate was added to complete the sample geometry. The background index was water (n = 1.33). The simulation space additionally consisted of a 2.3×2.3×0.5 µm (l×w×h) FDTD box with perfectly matched layer boundary conditions and a 4×4 nm mesh size, a 2.1×2.1×0.4 µm plane wave source at 638 nm, and a 1.8×1.8×0.2 µm advanced power absorption monitor. Here the power absorption is proportional to the electric field intensity and the imaginary part of the permittivity and is given in fraction of absorbed power per m^3 ($Pabs/m^3$).

3.4.10 Inductively coupled plasma mass spectrometry measurements

The preparation of the samples for the inductively coupled plasma mass spectrometry (ICP-MS) measurements took place via the transfer of the glass/ITO/Au/TiO_2/Pt samples in the liquid phase. Each sample was immersed in 1 ml of an aqua regia solution, HNO_3 ($\geqslant$ 65 %, puriss. p.a.) :HCl (37 %) (1:3), for 5.5 h at 60 °C until the glass substrate was completely transparent. The aqua regia solution was then left to cool down overnight. The transfer of the solution was being done carefully to a centrifuge tube, where it was further diluted with MilliQ water (18.2 MΩ.cm) in a total volume of 10 ml.

3.4.11 Supplementary figures

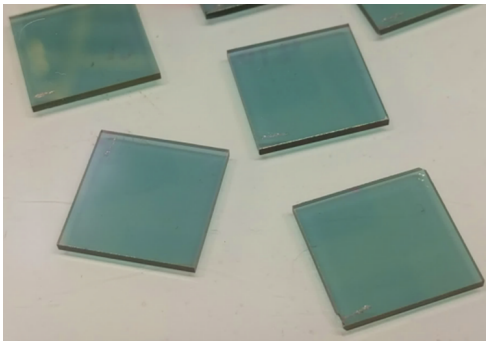

Figure 3.5. Photograph of Au nano-islands on glass/ITO.

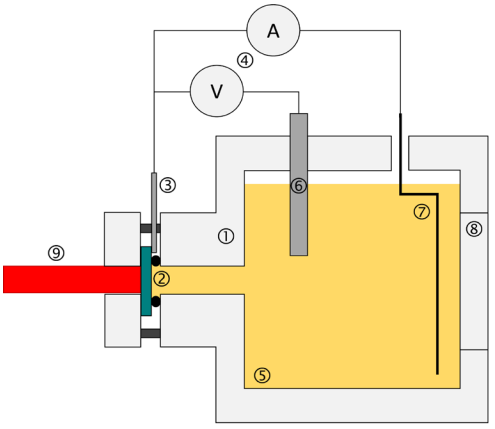

Figure 3.6. Photoelectrochemical setup used for deposition of Pt: Teflon cell (1), Au-TiO_2 substrate as working electrode (2), conductive aluminum tape (3), potentiostat connections (4), electrolyte (5), reference electrode (6), counter electrode (7), quartz window (8), and laser beam (9).

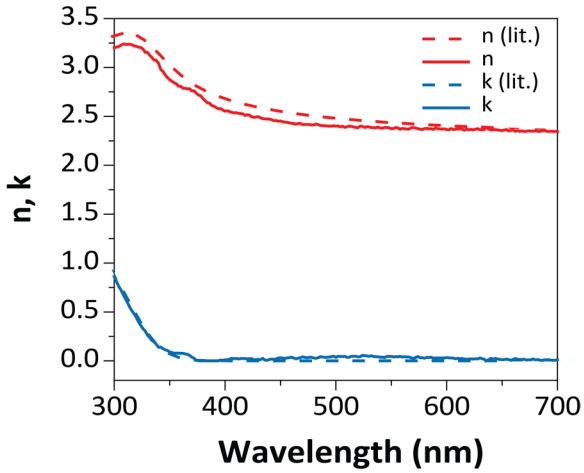

Figure 3.7. Optical constants (n,k) of the TiO_2 layer on a Si substrate, retrieved by ellipsometry measurements.

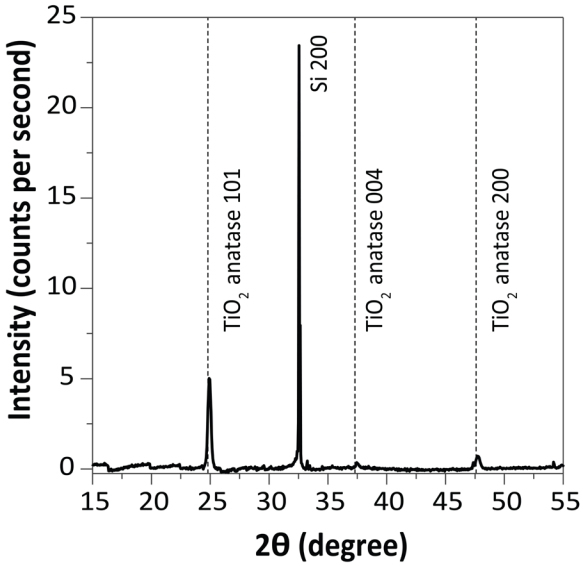

Figure 3.8. XRD spectrum of TiO_2 layer deposited with ALD on a Si substrate. Dashed lines show the position of the diffraction peaks of the TiO_2 anatase phase.[194]

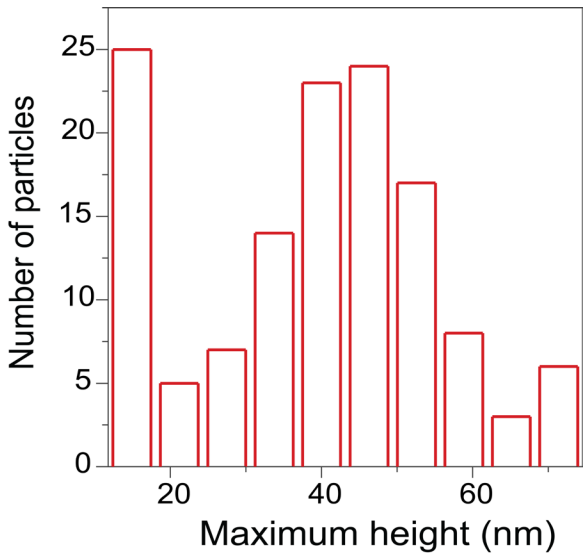

Figure 3.9. Maximum height distribution derived from AFM measurements for Au nano-islands covered with TiO_2.

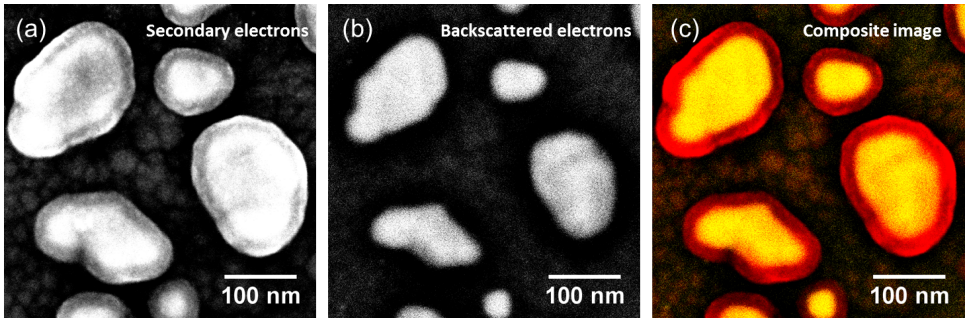

Figure 3.10. a) Secondary, b) backscattered and an overlay SEM image of a) and b) depicting the Au nano-islands coated with a TiO_2 layer on glass/ITO.

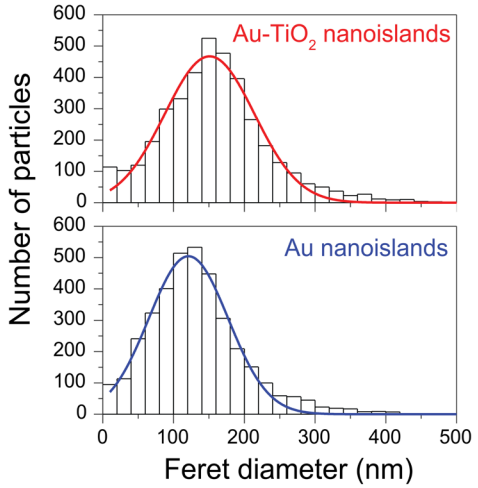

Figure 3.11. Particle distribution curves derived from SEM image analysis before (blue bottom curve) and after (red top curve) TiO_2 deposition.

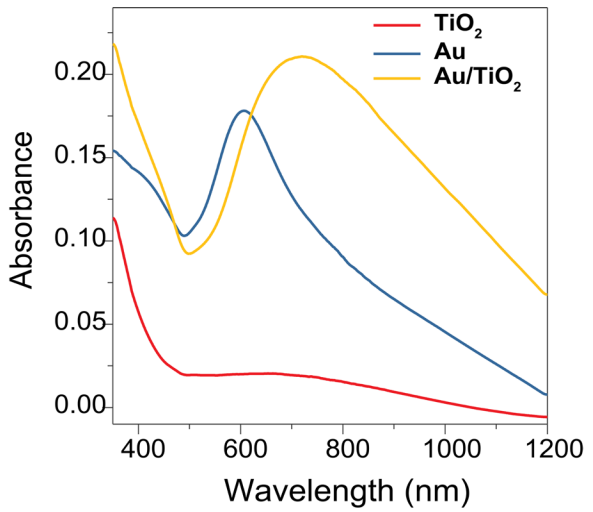

Figure 3.12. Absorption spectra of Au nano-islands with (yellow line) and without (blue line) TiO_2 and bare TiO_2 (red line) on ITO/glass. The absorbance of ITO/glass has been subtracted from the spectra presented here.

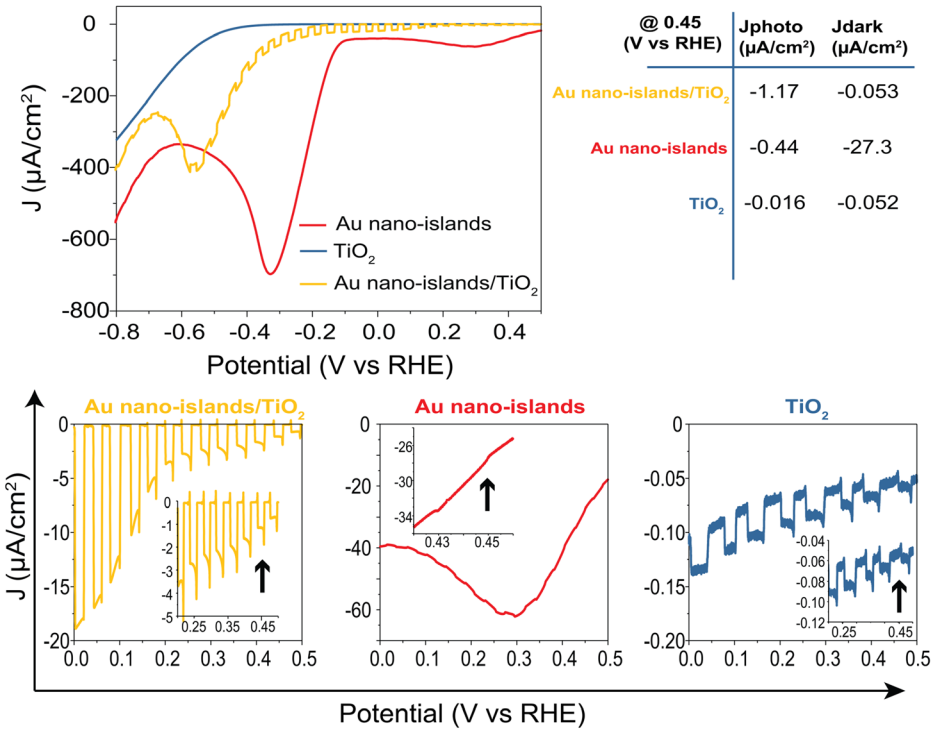

@ 0.45 (V vs RHE)	Jphoto (μA/cm²)	Jdark (μA/cm²)
Au nano-islands/TiO_2	-1.17	-0.053
Au nano-islands	-0.44	-27.3
TiO_2	-0.016	-0.052

Figure 3.13. Photocurrent density vs applied potential scans of bare TiO_2 (blue solid line), un-coated Au nano-islands (red solid line) and Au nano-islands coated with 18 nm TiO_2 in hexachloroplatinate (pH 3, 0.04 mM, in 0.1 M Na_2SO_4 aqueous solution) under chopped 638 nm illumination (0.5 W/cm^2), b) Table of photocurrent and dark-current values, derived from plot (a), at applied potential 0.45 V vs RHE, which is the potential used for the hot-e driven deposition of platinum nanoparticles, c), d) and e) Zoom-in images of plot (a) for Au nano-islands/TiO_2, Au nano-islands and bare TiO_2 respectively.

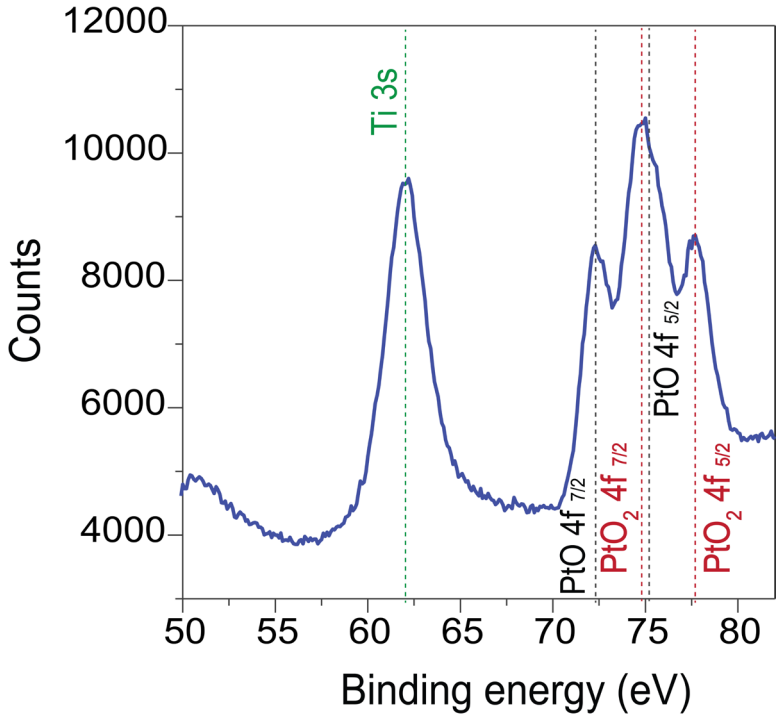

Figure 3.14. XPS spectrum of Au/TiO_2 nano-islands with photodeposited Pt nanoparticles before photoconditioning at -0.25 V vs RHE. The dashed lines correspond to the 3s, $4f_{7/2}$ and $4f_{5/2}$ binding energies of Ti (green color), Pt(II) (black color) and Pt(IV) (red color).[191] The XPS spectrum after photoconditioning can be find in the main text (Figure 3c). In the same figure is clear that most of the Pt oxides were converted to metallic Pt, which allowed for a fair comparison between the samples prepared with hot-electron deposition and electrodeposition of the cocatalyst.

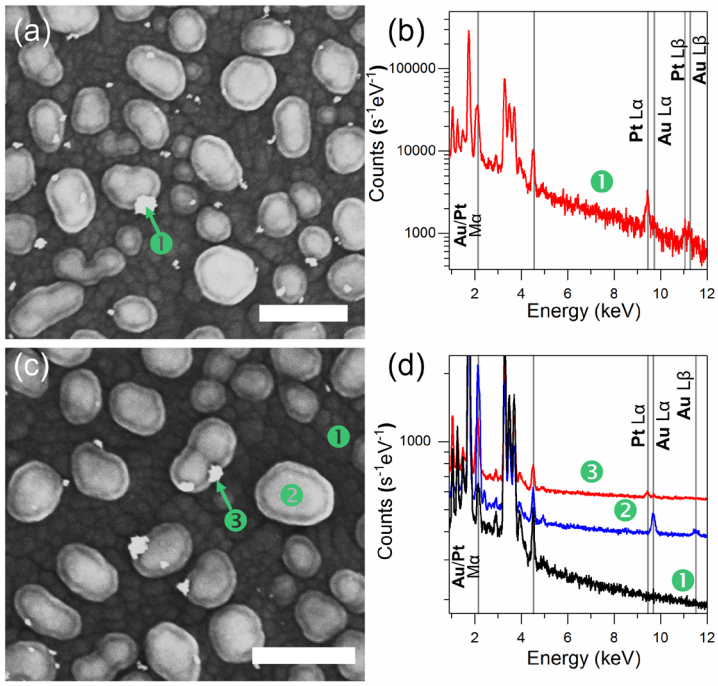

Figure 3.15. a) and c) SEM images of 2 different regions of the same sample of Au/TiO_2 nano-islands on glass/ITO after an electrical charge of 125 $\mu C/cm^2$ was passed to the sample in presence of hexachloroplatinate (pH 3, 0.04 mM, in 0.1 M Na_2SO_4 aqueous solution) under 638 nm illumination (0.5 W/cm^2). b) and d) the EDX measurements of regions a) and c) respectively, where each curve is associated with a number which corresponds to the exact spot investigated and depicted in the SEM images. Solid grey lines correspond to the x-ray emission peaks of Pt, Au and Ti.

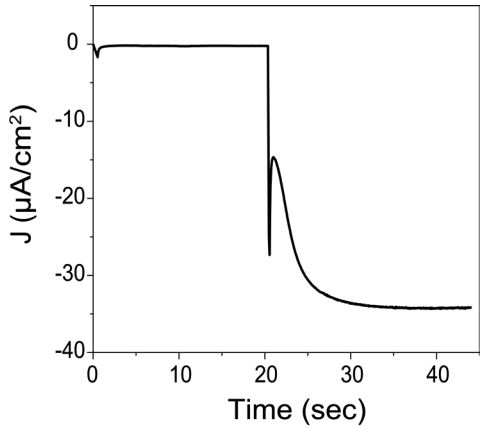

Figure 3.16. Photoconditioning curve (current density vs time) of Au/TiO_2 samples for conversion of the Pt oxides to metallic platinum, in pH 7 phosphate buffer, at -0.25V applied potential, where the first 20 sec the sample was kept in the dark while the following 45 sec the 638 nm laser beam (0.5 W/cm^2) hits the sample. The photocurrent is increasing gradually and then remains constant after full conversion of platinum oxides to metallic platinum.

Wavelength (nm)	**Power (μW)**
440	22
460	23
480	32
500	47
520	51
540	71
560	105
580	149
600	199
620	203
640	269
660	395
680	492
700	435
720	291
740	171
760	48

Table 3.1. The different wavelengths (nm) used to excite the Au/TiO_2 photocathodes for the IPCE measurements (Figures S11 and S12) and their respective power (μW).

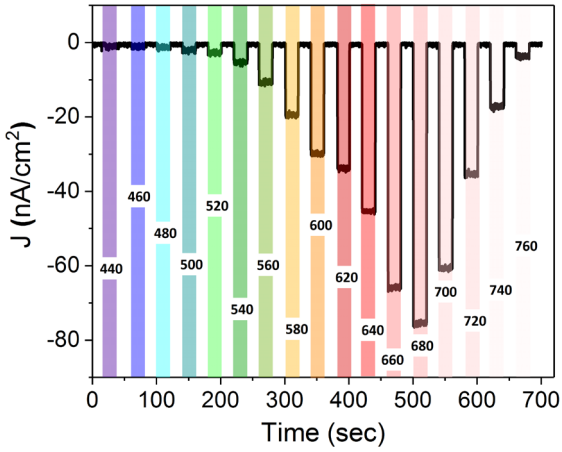

Figure 3.17. Photocurrent density vs time at different excitation wavelengths of a Au/TiO_2 sample in presence of hexachloroplatinate (pH 3, 0.04 mM, in 0.1 M Na_2SO_4 aqueous solution) at applied potential 0.45 V vs RHE. The width of each of the colored bars corresponds to the time where a different excitation wavelength was used. The respective excitation wavelength (nm) is also depicted on each of the colored bars.

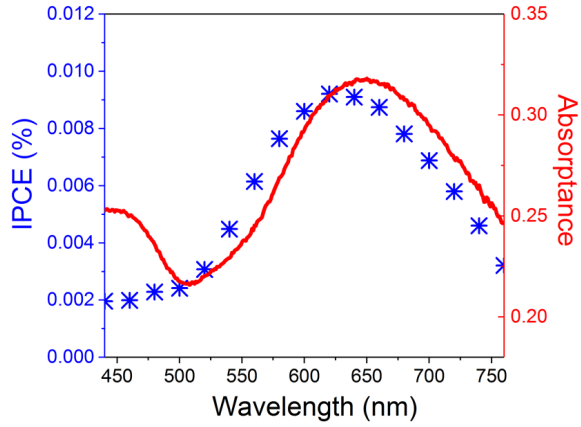

Figure 3.18. Incident Photon to Current Efficiency (IPCE, blue data points) vs wavelength of Au/TiO_2 photocathode in presence of hexachloroplatinate (pH 3, 0.04 mM, in 0.1 M Na_2SO_4 aqueous solution) and absorptance vs wavelength (red solid line) of the same sample before the IPCE measurement.

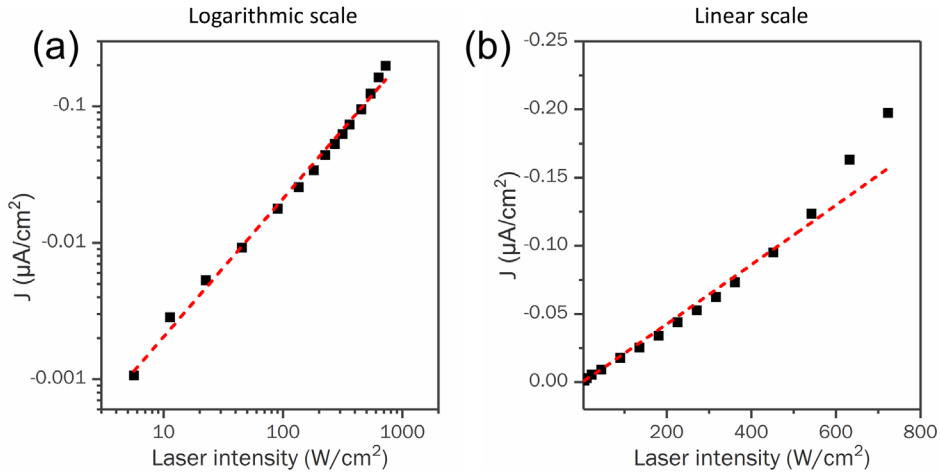

Figure 3.19. Photocurrent density vs 638 nm laser intensity of Au/TiO_2 in presence of hexachloroplatinate (pH 3, 0.04 mM, in 0.1 M Na_2SO_4 aqueous solution) in logarithmic (a) and linear (b) scale. Our photodeposition and photocatalysis experiments were conducted at an intensity of 0.5 W/cm^2.

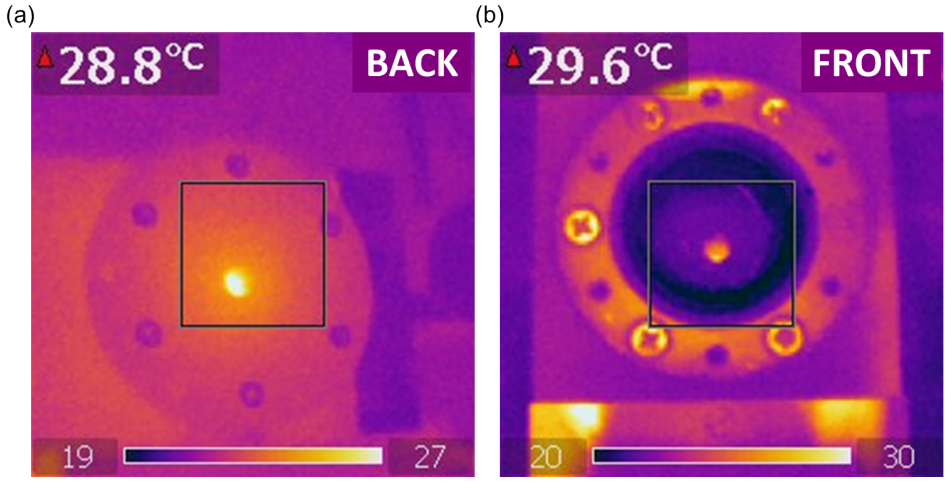

Figure 3.20. Image from thermal camera from a) the back side of the sample (sample in contact with hexachloroplatinate) and , b) the front side of the sample (the quartz window was removed in this case and the sample was in contact with air).

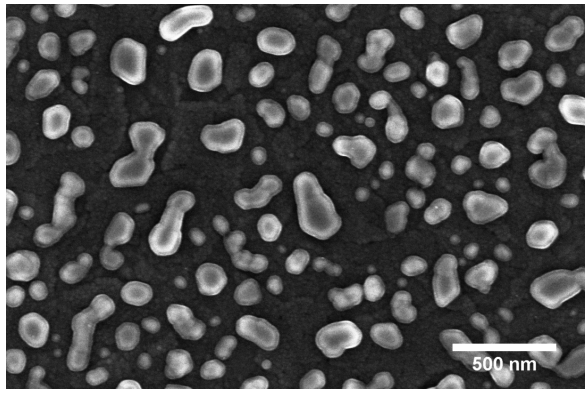

Figure 3.21. SEM image of Au nano-islands coated with 18 nm TiO_2 on ITO/glass. The sample was immersed in H_2PtCl_6 solution (pH 3, 0.04 mM, 0.1M Na_2SO_4) for 20 min, while the solution was heated up to 40°.

	Deposited amount of Pt (nano grams)	**Deposition method**
Data set # 1 (Figure 3.4a & 3.4b, 3.24)	19.4	Hot-e^- assisted ($Au/TiO_2/Pt_{photo}$)
	17.3	Electrodeposition ($Au/TiO_2/Pt_{electro}$)
Data set # 2 (Figure 3.25)	22	Hot-e^- assisted ($Au/TiO_2/Pt_{photo}$)
	35.8	Electrodeposition ($Au/TiO_2/Pt_{electro}$)
Data set # 3 (Figure 3.26)	25.1	Hot-e^- assisted ($Au/TiO_2/Pt_{photo}$)
	25.6	Electrodeposition ($Au/TiO_2/Pt_{electro}$)

Table 3.2. The total amount of deposited Pt on glass/Au/TiO_2 samples, in nano grams, retrieved from ICP-MS measurements; Samples prepared with the 2 different methods: hot-electron assisted deposition (photo) and electrodeposition (electro) are compared. Data sets #1, #2 and #3 correspond to 3 different groups of samples, whose photoelectrochemical performance was compared (see Figures 3.4a & 3.4b in the main text, Figure 3.25 and Figure 3.26 respectively).

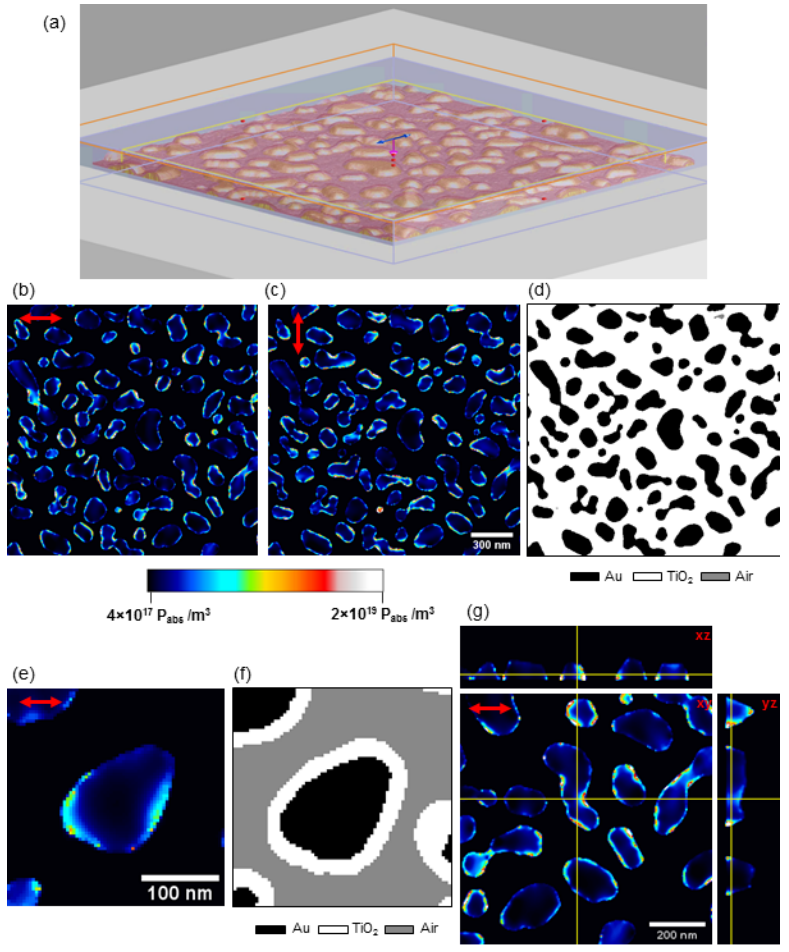

Figure 3.22. FDTD simulations on Au/TiO_2 nanoislands for 638 nm excitation. Experimental details given above. a) Schematic 3D representation of the simulation space in Lumerical, with an ITO substrate (white), Au nano-islands (yellow), and a 18 nm conformal TiO_2 layer (red transparent). b-d) Cross sections of the absorbed power (in fraction of absorbed power/m3) at 10 nm above the ITO substrate surface for light injection polarized along the x-axis (b) and along the y-axis (c), and a material map (d). e) Cross section of the absorbed power in a single Au/TiO_2 nanoisland at 22 nm above the ITO substrate. The corresponding material map is shown in panel (f). Note the lack of absorbed power in the TiO_2 shell. g) Orthogonal projections along the yellow lines for a 500x500 nm absorbed power map at 10 nm above the ITO substrate.

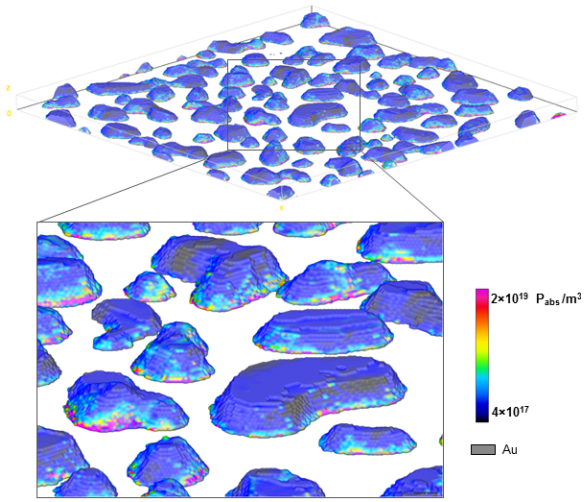

Figure 3.23. Three-dimensional simulation view of the absorbed power in a section of Au-TiO_2 nanoislands (2×2 µm square), made using the Volume Viewer in ImageJ v1.52 in volume mode and with tricubic sharp interpolation. For clarity, the fraction of absorbed power volume (in blue to red color gradient) is overlaid on top of the nanoisland bodies (in grey). The voxel size is 5×5×5 nm. We observe that most of the absorbed power is near the base of structures and that the absorption hotspots are localized all around each particle (i.e. not very well localized).

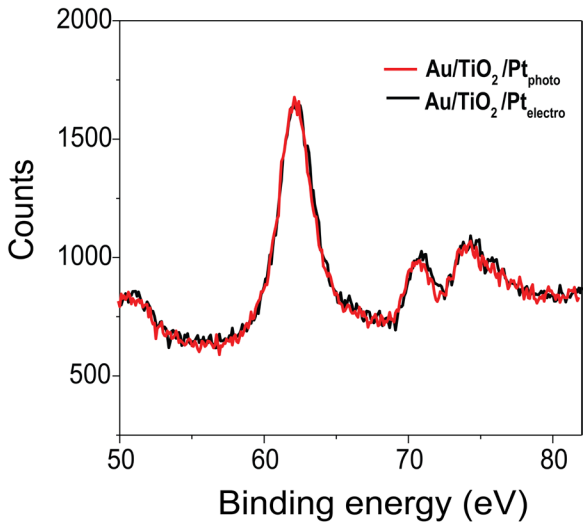

Figure 3.24. XPS spectra of $Au/TiO_2/Pt$ samples presented and compared in Figure 4, prepared with hot-electron driven chemistry (red line) and with electrodeposition (black line). XPS peak with a binding energy of around 62 eV corresponds to Ti 3s and peaks at 71 eV and 74.3 eV to Pt $4f_{7/2}$ and Pt $4f_{5/2}$ respectively.

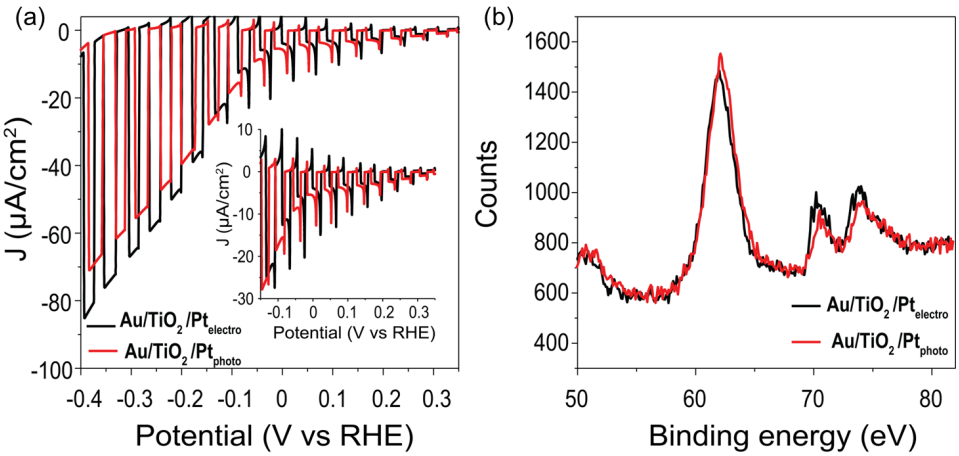

Figure 3.25. Data set #2 of the photocatalytic performance comparison of two $Au/TiO_2/Pt$ samples prepared with hot-electron driven chemistry (red line) and electro-deposition (black line), a) current density vs applied potential and b) XPS spectra. XPS peak with a binding energy of around 62 eV corresponds to Ti 3s and peaks at 71 eV and 74.3 eV to Pt $4f_{7/2}$ and Pt $4f_{5/2}$ respectively. In this data set the deposited amount of Pt is higher on the sample made with electrodeposition (according also to ICP-MS measurements), which could explain why in higher applied potentials the same sample performs better than the sample made with photo-electrodeposition.

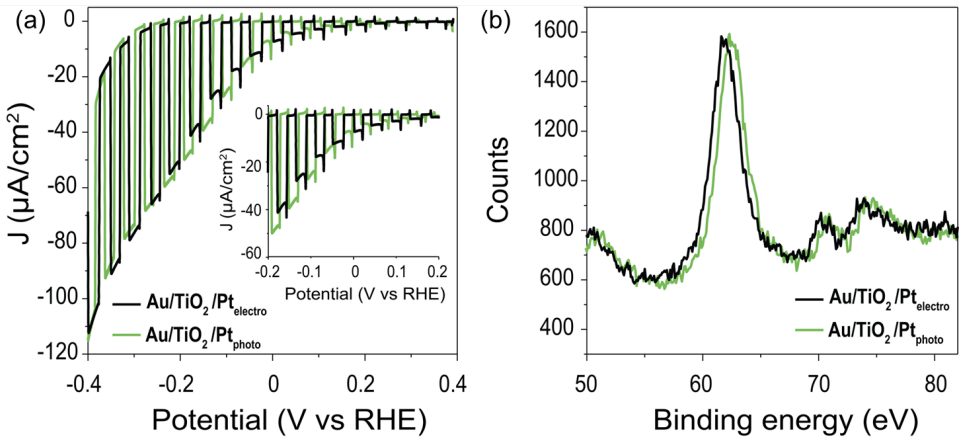

Figure 3.26. Data set #3 of the photocatalytic performance comparison of two $Au/TiO_2/Pt$ samples prepared with hot-electron driven chemistry (green line) and electro-deposition (black line), a) current density vs applied potential and b) XPS spectra. XPS peak with a binding energy of around 62 eV corresponds to Ti 3s and peaks at 71 eV and 74.3 eV to Pt $4f_{7/2}$ and Pt $4f_{5/2}$ respectively.

4

Utilization of all hot-carriers in plasmonic nanostructures for selective deposition of nanomaterials

Hot-electrons generated in metal nanoparticles can drive chemical reactions and selectively deposit cocatalyst materials on the plasmonic hot-spots, the areas where the decay of plasmons takes place and the hot-electrons are created. Herein, the use of hot-holes for deposition of nanomaterials with nanoscale resolution is explored as well as the use of both hot-electrons and hot-holes for simultaneous deposition of more than one cocatalyst. For this purpose, Au plasmonic nano-islands on a thin TiO_2 layer are excited at their surface plasmon resonance first in presence of a manganese precursor in an aqueous electrolyte, in order to use hot-holes for the oxidation of the precursor and the deposition of a cocatalyst (MnO_x). Then a platinum precursor is combined with the manganese one for the simultaneous deposition of more than one cocatalyst through the hot-electron reduction of the former and the hot-hole oxidation of the latter. SEM images and elemental EDX and XPS analysis verified the formation of cocatalysts in both of these two cases on the surface of the plasmonic nanoparticles. Au nanostructures with more confined hot-spots (Au nanotriangles) were also used to explore the correlation of the deposition sites of one of the cocatalysts with the plasmonic hot-spot location, identified with FDTD simulations, and a good overlap was found. These results add more flexibility to the use of hot-carriers and open up the way for the design of complex photocatalytic nanostructures.

4.1 Introduction

Plasmonic nanoparticles are considered good candidates for photocatalysis mostly due to their large and tunable absorption cross sections in the visible spectrum and their ability to generate highly energetic carriers.[20, 127, 195–198] The light-driven resonant collective oscillations of the free electrons (i.e. plasmons) in noble metal nanostructures are responsible for their unique properties. Plasmons can concentrate the light in the vicinity of the nanostructure in sub-wavelength volumes (i.e. "hot"-spots), where the intensity of the electric near-field can be extremely enhanced.[28, 199] The location of these hot-spots can be easily tuned on the same nanostructure by changing the polarization or the wavelength of the incident light. The decay of the plasmons at the hot-spots, via Landau damping, can give rise to the excitation of conduction band electrons to energy states higher than the Fermi level (E_f) of the metal, with maximum energy $E_f + hv$. These initially non-thermal high energy electrons (hot-electrons) and the respective holes (hot-holes) can be extracted from the nanostructure and react with nearby molecules by injection to their unoccupied orbitals.[34, 161, 200, 201] The energy of the photogenerated hot-carriers can be tuned by changing the energy of the incident photons, which can be useful for promoting certain chemical pathways according to their energy requirements and increase the selectivity over specific chemical products.[109, 202, 203] It has also been demonstrated that hot carriers have reaction rates scaling super-linearly under high photon flux and/or in dense particle systems, in contrast to conventional semiconductor photocatalysts (they usually scale with the square root of light intensity), which can open different pathways in light-driven chemical reactions.[160, 204] Hot-carriers have already been used for a plethora of chemical reactions such as water splitting,[167, 168, 205, 206] H_2 dissociation,[207] CO oxidation,[208] NH_3 decomposition [112], reduction of diazonium salts[163] and synthesis of nanomaterials. [209, 210]

Although hot-carriers in plasmonic nanoparticles seem very promising for driving chemical reactions with light, the quantum efficiency of these reactions is still very low ($\sim 1\%$).[111] Hot-electrons and hot-holes thermalize very fast to a Fermi-Dirac distribution through electron-electron (100 fs to 1 ps) and electron-phonon scattering (1 to 10 ps) to finally dissipate heat to the local environment (100 ps to 10 ns).[34, 50, 107] A common way to cope with these short lifetimes is to separate the hot-carriers using a Schottky barrier, by adding a semiconductor (e.g. TiO_2), which can accept the hot-electrons or hot-holes.[177, 211] The timescales of the extraction of the hot-electrons (holes) to the conduction (valence) band of the semiconductor is usually much shorter than the electron-phonon scattering.[107] For highly energy demanding chemical reactions though such as water splitting, the addition of cocatalyst nanoparticles is also necessary to achieve higher photon to electron efficiencies.[212–214] However, cocatalysts are often very expensive materials (e.g. Pt) and they lack good optical properties. So, a smart design of plasmonic/cocatalyst nanostructures is necessary, in order to combine the optical properties of the former and the good catalytic activity of the latter.

This could be achieved by the careful positioning of the cocatalyst on the surface of the plasmonic nanostructures.

The hot-spots of the plasmonic nanostructures are the areas where the hot-electrons and hot-holes are mostly generated, so a cocatalyst at these locations could help the charge separation and increase the fraction of carriers participating in the chemical reactions.[168, 176, 215] Several studies have already shown that the positioning of the cocatalyst on the plasmonic hot-spots can increase the efficiency of the metal nanostructure and at the same time reduce the amount of the material needed, decreasing the cost.[178, 210, 216, 217] In the most of those studies, surfactant chemistry is used to position the cocatalyst at the hot-spots, where ligands bind preferentially to specific sites on the metal nanostructure allowing the deposition of the new material (cocatalyst) at localized free surface site. Such an approach though cannot always ensure a match between the deposition sites.[178, 179] As a result, surfactant chemistry is not able to "engineer" nanostructures in such a way that every time the plasmonic hot-spots coincide with the location of the cocatalyst. Here, we want to use the photogenerated hot-carriers themselves to localize the formation of the cocatalysts on the plasmonic hot-spots. Hot-electrons have already been used for reduction reactions resulting in the deposition of catalytic Pt nanoparticles on plasmonic nanostructures,[162, 190, 210] but to our knowledge the utilization of both hot carriers for the deposition of different cocatalysts has not been demonstrated before.

In this work, gold plasmonic nano-islands are excited at their local surface plasmon resonance to generate hot-electrons and hot-holes, which are used for reduction and oxidation reactions respectively, for the simultaneous formation of 2 different cocatalyst materials. First, the photodeposition of one cocatalyst is investigated using the photogenerated hot-holes. The gold nano-islands prepared on a thin TiO_2 anatase layer are illuminated in the presence of $MnSO_4$ and an electron scavenger ($NaIO_3$). Hot-holes are used for the oxidation of $MnSO_4$ (Mn^{2+}) to MnO_x (cocatalyst 1), while hot-electrons are either injected to the conduction band of the nearby semiconductor layer (TiO_2) or scavenged by the electron acceptor (Figure 4.1a). The simultaneous deposition of two different cocatalysts is also explored by substituting the electron scavenger with a platinum precursor to drive the reduction of the latter to Pt metal nanoparticles (cocatalyst 2) using the photogenerated hot-electrons (Figure 4.1c). This approach of using all the hot-carriers of plasmonic nanoparticles for the selective deposition of cocatalytic materials to synthesize nanostructures, where the optical properties of the plasmonic material are combined with the catalytic properties of the added cocatalysts, can be very promising for photocatalysis. Our results add more flexibility to the design of plasmonic nanocatalysts through the utilization of both hot-electrons and hot-holes, without the need of additional applied potential or extra functionalization of the plasmonic nanostructures.

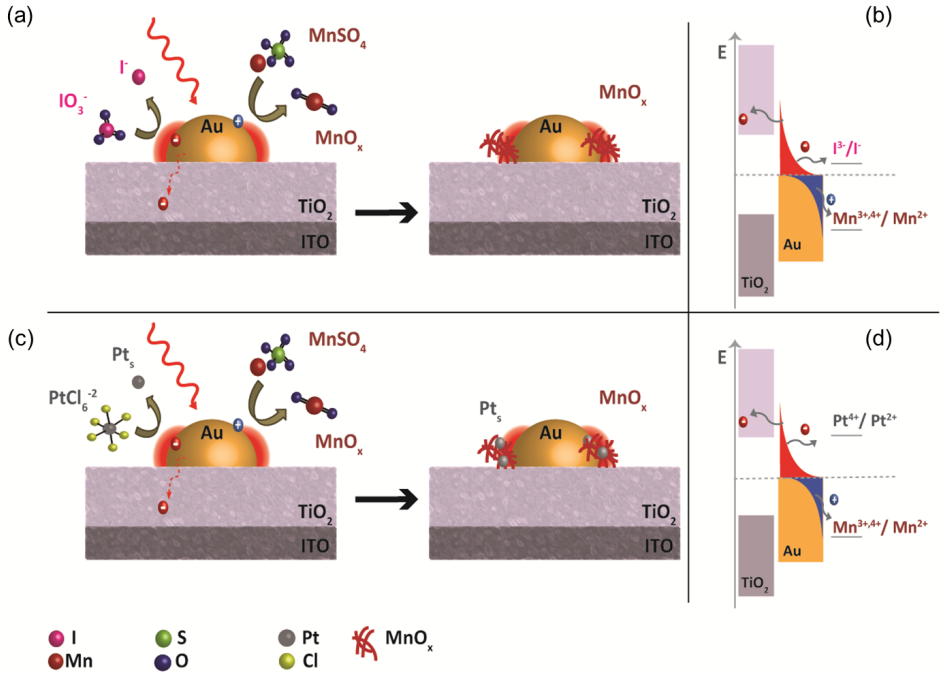

Figure 4.1. Plasmonic Au nano-islands on TiO_2 are excited at their surface plasmon resonance (638 nm) in a (a) $MnSO_4/NaIO_3$ or in a (c) $MnSO_4/H_2PtCl_6$ aqueous solution, hot-electrons and hot-holes are photogenerated at the plasmonic hot-spots, hot-electrons reduce $NaIO_3$ to the soluble NaI (I^{3-} to I^-) in (a)) or H_2PtCl_6 to Pt solid species, (Pt^{4+} to Pt^{2+} in (c)) while hot-holes oxidize Mn^{2+} to solid state MnO_x (Mn^{2+} to Mn^{3+} and/or Mn^{4+}). b) and d) Simplified energy diagrams where the reduction potentials of the redox reactions are depicted together with the energy levels of the Schottky junction and the Fermi-Dirac distribution of the hot-carriers.

4.2 Results and Discussion

Gold plasmonic nano-islands were fabricated on a TiO_2 substrate with the aim of using them for the photogeneration of hot electrons and hot-holes and to drive redox reactions for the deposition of cocatalyst nanoparticles. A thin TiO_2 layer ($\sim$ 22 nm) was deposited on ITO/glass with atomic layer deposition at 100 °C and annealed for 3 h at 350 °C to form the anatase phase, which acts as an efficient hot-electron extraction medium.[218] An 8 nm Au film was sputter-coated on the TiO_2 layer and was converted to Au plasmonic nano-islands after annealing for 1h at 300 °C in air. The prepared Au

nano-islands with mean largest diameter of 67 ± 35 nm (Figure 4.5), have a surface plasmon resonance at ∼ 638 nm (Figure 4.6b). The samples are illuminated at the peak of their surface plasmon resonance with a laser diode (638 nm, 0.5 W/cm^2) to generate hot-electrons and hot-holes. The excitation of the plasmonic nano-islands takes place in presence of an aqueous solution of $MnSO_4$ (0.01 M, pH 5.2, N_2 purged) and $NaIO_3$ (0.02 M) to facilitate the oxidation of $MnSO_4$ (Mn^{2+}) to the cocatalyst MnO_x (possible redox reactions: reaction 4.1 and 4.2) using the photogenerated hot-holes.[135, 219] $NaIO_3$ (IO_3^- in water) acts as a secondary channel for hot-electron scavenging since it can be reduced to I^- (reaction 4.3)[220, 221] by any electrons not immediately injected into TiO_2.

$$Mn^{2+} + 2H_2O + 2h^+_{hot} \rightarrow MnO_2 + 4H^+ \tag{4.1}$$

$$2Mn^{2+} + 3H_2O + 2h^+_{hot} \rightarrow Mn_2O_3 + 6H^+ \tag{4.2}$$

$$IO_3^- + 6e^-_{hot} + 3H_2O \rightarrow I^- + 6OH^- \tag{4.3}$$

SEM images (Figure 4.2c and Figure 4.6a), in two different modes (in-column detector, ICD, and through the lens detector, TLD) for separation of the heavier Au nano-islands, retrieved after 10 min of continuous illumination of the samples reveal the formation of a new material mostly on the Au nano-islands and not on the TiO_2 surface. The morphology of the newly formed material looks very similar to photodeposited MnO_x on semiconductor crystals in the work of Li et al.[135] EDX (Figure 4.2d) and XPS (Figure 4.2g) measurements were conducted for the elemental analysis of the samples after their irradiation. EDX data demonstrate that the deposited compound corresponds to Mn (Mn peak, red solid line, Figure 4.2d) and this is also verified by the XPS spectra. Information for the exact oxidation state of the deposited Mn was recovered from XPS analysis in the Mn 2p region, where several new peaks are detected on illuminated samples (Figure 4.2g, "TiO_2/Au after 10 min in $MnSO_4$/$NaIO_3$") compared to the non-irradiated samples (Figure 4.2g, "TiO_2/Au"). The binding energies of the Mn $2p_{3/2}$ (641.7 and 644.9 eV) and Mn $2p_{1/2}$ (653.4 eV) peaks can be assigned, according to literature, to a mixture of Mn^{3+} (Mn_2O_3) and Mn^{4+} (MnO_2) species.[222–224] Note that the Au $4p_{1/2}$ peak (Figure 4.2g, "TiO_2/Au", green solid line) in principle overlaps with the Mn $2p_{3/2}$ peak, but this does not prohibit the distinction between the two peaks in the illuminated sample; the Au signal is strongly suppressed in the Mn-covered sample (Figure 4.2g, "TiO_2/Au after 10 min in $MnSO_4$/$NaIO_3$") due to the surface sensitivity of XPS measurement. Illumination of the plasmonic nano-islands results in deposition of a cocatalytic material (MnO_x, with $1.5 \leqslant x \leqslant 2$), which is the result of hot-hole oxidized Mn^{2+} (control experiments discussed below).

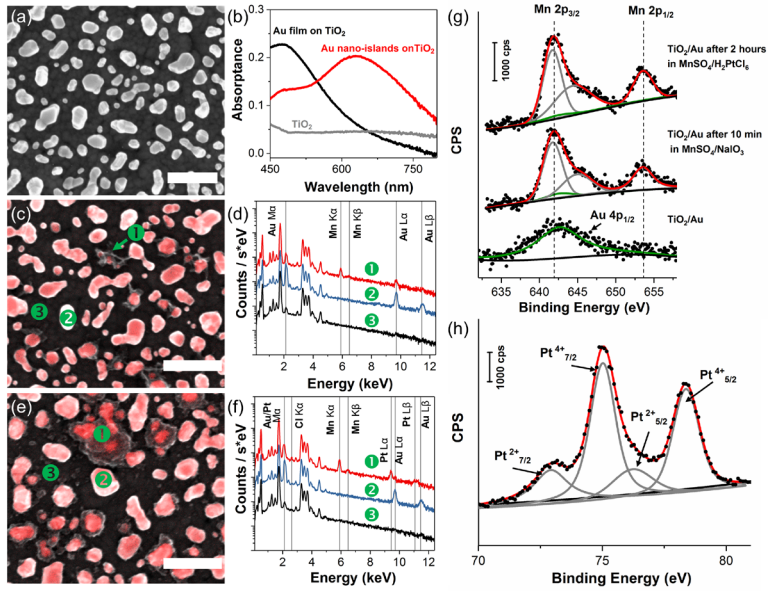

Figure 4.2. a) SEM image of Au nano-islands on TiO_2/ITO/glass substrate (200 nm scale bar). b) Absorptance spectrum of the Au nano-islands on TiO_2 (red solid line, after subtracting the ITO/glass contribution), of the Au film (8 nm) before the annealing to form the Au nano-islands (black solid line) and of 22 nm anatase TiO_2 film (grey solid line). c) SEM images of Au nano-islands after 10 minute and e) 2 hour illumination at 638 nm (0.5 W/cm^2) in $MnSO_4/NaIO_3$ and $MnSO_4/H_2PtCl_6$ respectively. These panels overlay SEM images from two different detectors to help differentiate between the Au (or Pt) and MnO_x (details is SI): the ICD (red-false coloring) which provides mostly z-contrast (Au and Pt) and the in-lens detector (greyscale) which provides mostly topographical contrast (MnO_x, Au and Pt). The scale bar is 200 nm. d) and f) are the EDX spectra of samples c) and e) respectively, where each numbers on the spectrum corresponds to a specific and depicted point on the SEM image. g) XPS spectra (black dots) of the samples shown in panels a), c) and e) in the Mn 2p region. h) XPS spectrum of sample e) in the Pt 4f region. Red lines represent cumulative fitting curves, grey lines represent individual peak fits annotated per element and oxidation state, and green lines in g) represent the Au $4p_{1/2}$ peak. A Shirley-type baseline was used.

Several control experiments were conducted to elucidate the deposition of the cocatalysts on the Au plasmonic nano-islands on TiO_2. The samples were immersed in the $MnSO_4/NaIO_3$ electrolyte and kept in the dark for 30 min, to exclude any spontaneous oxidation of $MnSO_4$ due to the presence of the electron scavenger. SEM images (Figure

4.8) were retrieved and no deposition of MnO_x or any other material was observed on the plasmonic nanostructures. Simple heating experiments, where the temperature of the solution was heated to $\sim$ 40 °C (Figure 4.9a) and kept constant for around 30 min, did not result either in the formation of any material on the surface of the samples (Figure 4.9b), while as mentioned above 10 min of illumination of the samples were enough to form MnO_x (Figure 4.2c). Note that 40 °C is well above the surface temperature measured by a thermal camera during 0.5 W/cm^2 irradiation of the sample (Figure 4.9c). The role of the electron scavenger $NaIO_3$ in the photodeposition of MnO_x was also investigated by running experiments without it. MnO_x formation was observed even in the absence of $NaIO_3$, but at a slower deposition rate, as expected (see SEM image, Figure 4.10). If there is no $NaIO_3$ present in the solution, which acts as an efficient electron acceptor, hot-electrons that are not energetic enough to get injected to the conduction band of TiO_2, recombine with the hot-holes in the plasmonic nanostructure. Naturally, more recombination of hot-carriers leads to less deposited material.

The simultaneous deposition of two different cocatalysts (MnO_x and Pt) driven by hot-carrier chemistry was also investigated. For this experiment all parameters were kept constant, except for replacement of the sacrificial electron scavenger $NaIO_3$ with the Pt nanoparticle precursor hexachloroplatinic acid (H_2PtCl_6), which now takes the role of hot electron acceptor. Now, the role of the electron scavenger is taken by the hexachloroplatinate in the electrolyte, the reduction of which could result in solid Pt species. Indeed, after 20 min of continuous irradiation of the samples, formation of new material was observed by SEM images and its morphology looked different than in absence of H_2PtCl_6 (Figure 4.6b). Subsequently, EDX (Figure 4.2f) and XPS measurements (Figure 4.2g and Figure 4.2h) were conducted for the elemental analysis of the material deposited on the Au nano-islands. Samples illuminated for 2h (Figure 4.2e) were used for the elemental analysis to increase the signal. EDX spectra (Figure 4.2f) showed that both Pt and Mn are present on the surface of the Au nano-islands after the experiment but more information about the oxidation state of the deposited species was retrieved by the XPS analysis. The presence of new peaks in the Mn 2p region in the XPS spectra, in similar binding energies as in the case of only MnO_x deposition (see Table 4.1), showed that the formed Mn is again a mixture of Mn^{3+} and Mn^{4+} species. The analysis of the Pt 4f XPS region (Figure 4.2h) shows that the Pt species presented on the surface of the sample can be assigned to binding energies of the Pt^{2+} and Pt^{4+} doublets. The binding energies of the Pt^{2+} can be associated with $Pt(OH)_2$ formation as the product of the reduction of a hydrolyzed product of hexachloroplatinate (reaction 4.4). The Pt^{4+} binding energies correspond to PtO_2, which can only be the product of an oxidation reaction (reaction 4.5).[225] As a result, the substitution of $NaIO_3$ in the electrolyte with hexachloroplatinate leads to the deposition of a complex combination of metal oxide and hydroxide cocatalysts (MnO_x with $1.5 \leqslant x \leqslant 2$, $Pt(OH)_2$ and PtO_2).

$$Pt(OH)_2Cl_4^{2-} + 2e_{hot}^- \rightarrow Pt(OH)_2 + 4Cl^- \tag{4.4}$$

$$Pt(OH)_4Cl_2^{2-} + 4h_{hot}^+ \rightarrow PtO_2 + 4H^+ + O_2 + 2Cl^- \quad (4.5)$$

The presence of TiO_2 has been also found to be very crucial for driving the oxidation of $MnSO_4$ and the reduction of H_2PtCl_6. No deposition of MnO_x was observed on Au nano-islands on ITO/glass, in $MnSO_4/NaIO_3$ electrolyte, even after 6 h of continuous illumination at 638 nm (Figure 4.11). The fact that TiO_2 alone absorbs 4 times less light compared to the combination of Au nano-islands on TiO_2 (Figure 4.2b) and that no deposition of MnO_x was observed on the TiO_2 surface, shows that the $MnSO_4$ oxidation could not be the result of just light absorption in the TiO_2. Au nano-islands on ITO/glass in $H_2PtCl_6/MnSO_4$ were also illuminated for 1 h and again no deposition of material was noticed. This indicates that TiO_2 has probably a double role in the experiment. TiO_2 promotes the oxidation reaction for the formation of the cocatalysts by either providing energy states to improve hot-electron extraction or contributing to the better binding of the $MnSO_4$ and H_2PtCl_6 molecules on the TiO_2/Au/electrolyte interface.[181, 226] In that way the probability of hot-holes and hot-electrons interacting with $MnSO_4$ and H_2PtCl_6 molecules on the TiO_2/Au/electrolyte interface can be strongly enhanced together with the reaction rate, since the molecules spend more time there.

Photoelectrochemical measurements were conducted to verify that the deposition of the cocatalysts was achieved with hot-carrier chemistry. With that aim, Au nano-islands on TiO_2 were placed in a 3-electrode photoelectrochemical cell (see simplified schematic in Figure 4.3a) to explore any correlation of the generated photocurrent with the optical properties of the nanostructures (absorptance). In our previous work, a direct correlation between hot-electron generation and Pt nanoparticle formation was found.[210] Therefore, the reaction that was mostly investigated here was the oxidation of $MnSO_4$ to MnO_x in absence of the electron scavenger, in order to collect as many hot-electrons as possible through an external electrical circuit. During these experiments, a potential was applied to the sample (working electrode) with respect to a reference electrode (Ag/AgCl), while the current flow to a counter electrode (a platinum wire) was recorded to monitor the electron consumption by the chemical reaction. The Au nano-islands on TiO_2/ITO/glass were excited with a low-intensity supercontinuum laser at different wavelengths in presence of $MnSO_4$ (0.01 M, pH 5.2), at an applied potential of 0.4 V vs RHE (OCV value of the sample tested, i.e. without additional electrical bias to the system). At each excitation wavelength, the photocurrent was measured (Figure 4.12) and used for the calculation of the Incident-Photon-to-Current-Efficiency (IPCE, see SI for more information) of the samples. IPCE values were plotted as a function of the wavelength together with the absorptance spectrum of the same sample (Figure 4.3b). The peak of the IPCE values matches quite well with the LSPR of the gold nano-islands with exception of the short wavelength region, which corresponds to interband transitions of Au. These transitions lead to excited electrons with energy close to the Fermi level and do not have enough energy to get transferred to the conduction band

of TiO_2. In this case, there is no separation of the hot-electrons from the hot-holes, and fast recombination of the hot-carriers could limit the oxidation of Mn^{2+}, since less hot-holes reach the electrolyte.[227] The IPCE peak seems also blueshifted and more narrow compared to the absorptance spectrum of the Au nano-islands. This could be due to the fact that smaller particles on the sample, which absorb light in shorter wavelengths, generate more energetic hot-holes which can drive the redox reaction than bigger nanoparticles.[43]

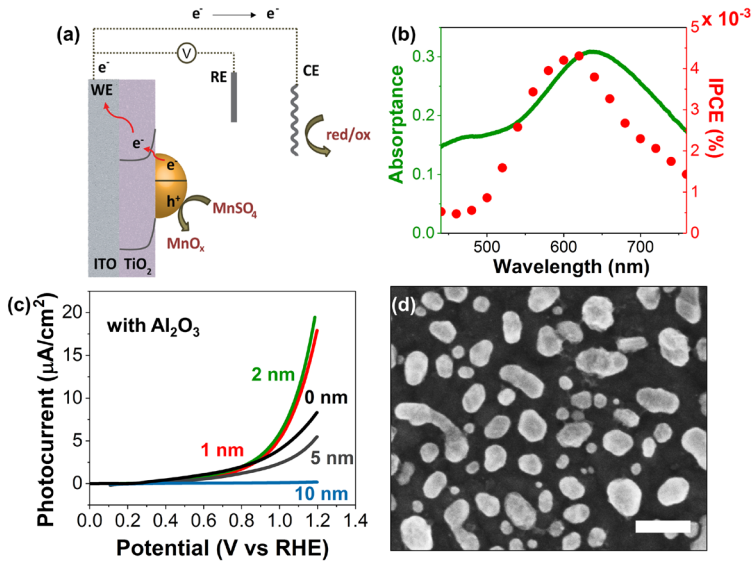

Figure 4.3. a) Simplified schematic of the 3-electrode photoelectrochemical system used for retrieving the data in image (b). WE stands for working electrode (i.e. the sample), CE for counter electrode (platinum wire) and RE for reference electrode (Ag/AgCl). b) Incident photon to current efficiency (IPCE, red circles) of Au nano-islands on TiO_2/ITO/glass substrate in aqueous $MnSO_4$ solution (pH 5.2, 0.01 M) and the respective absorptance spectrum (green solid line) of the same sample. c) Photocurrent density vs potential curves of Au nano-islands on TiO_2/ITO/glass as prepared (black solid line, "0 nm") and coated with 1 (red solid line, "1 nm"), 2 (green solid line, "2 nm"), 5 (grey solid line, "5 nm") and 10 nm (blue solid line, "10 nm") of Al_2O_3 excited at 638 nm (0.5 W/cm^2) in presence of $MnSO_4$ (pH 5.2, 0.01 M). d) SEM image of Au nano-islands on TiO_2/ITO/glass coated with 1 nm of Al_2O_3 after 20 min excitation at 638 nm (0.5 W/cm^2) in presence of $MnSO_4$ aqueous solution (pH 5.2, 0.01 M) without applying any potential.

Au nano-islands on TiO_2 were coated with 1, 2, 5 and 10 nm thick Al_2O_3 layer with atomic layer deposition, to further investigate the photodeposition mechanism and rule out any thermal effects. Coating the plasmonic nanostructures with an insulating

layer can prohibit the injection of the hot-holes to the electrolyte, except in the case where hot-holes are tunneling through the insulating layer, or transferred via pinholes or oxide defects. On the other hand, 10 nm of Al_2O_3 should not substantially change the temperature at the solution interface. Therefore, a decrease in photocurrent with increasing oxide thickness would provide further evidence that hot-carriers rather than thermal effects are responsible for the photodeposition. The photocurrent of samples with different Al_2O_3 thicknesses was recorded as a function of the applied potential (Figure 4.3c), in the same 3-electrode photoelectrochemical cell mentioned above, in presence of $MnSO_4$. The photocurrent of the samples initially increases up to 2 nm and then rapidly decreases with increasing Al_2O_3 thickness. This is consistent with the competing effects of improved adhesion of Au nano-islands to the surface with increasing ALD thickness (Figure 4.13) and decreased photocurrent from inhibited charge transport at larger thicknesses. Already after the addition of few nanometers of an insulating layer, tunneling should be constrained but in our case a thickness of 10 nm of Al_2O_3 is needed to make the photocurrent negligible (i.e. minimize the amount of hot-holes reaching the Al_2O_3/electrolyte interface). Trimethylaluminum oxide (ALD precursor for Al_2O_3 deposition) does not bind well on the Au surface, so probably a deposition of 1-5 nm of Al_2O_3 does not result in full coverage of the Au nano-islands.[228] The addition of thicker layers of ALD Al_2O_3 before current is eliminated has also been observed in halide perovskite solar cells recently.[229] The dependence of the photocurrent on the thickness of the insulating layer provides additional verification that the oxidation of Mn^{2+} to MnO_x is the result of a hot-hole rather than purely thermal or chemical reaction mechanism.

Au nano-islands are a very good system to monitor the hot-hole chemical reaction due to the high coverage of the sample and the easily detectable photocurrent, but do not have well-defined hot-spots.[45] However, plasmonic nano-triangles (Figure 4.4a) with an average side of 112 ± 18 nm and around 30 nm height (Figure 4.14) fabricated with nanosphere lithography, allow us to investigate the location of the deposition sites of one of the cocatalysts (MnO_x) and correlate them with the plasmonic hot-spots. The absorption spectrum of the prepared Au nanotriangles on TiO_2/ITO/glass (Figure 4.4b, green circles and Figure 4.15) was retrieved with integrating sphere microscopy, a technique developed previously in our group.[230] FDTD simulations based on backscattered electron images were used to extract the average fraction of absorbed power (Figure 4.4b, red solid line) of 163 individual Au nano-triangles as well as the location of their plasmonic hot-spots (Figure 4.16d). The samples were illuminated also at 638 nm (0.5 W/cm^2), in one of their surface plasmon resonance peaks, for 10 min in the $MnSO_4$/$NaIO_3$ electrolyte to repeat the MnO_x deposition. SEM images after the illumination of the samples (Figure 4.4c) showed that MnO_x was deposited on the surface of the plasmonic nanostructures. This specific wavelength was chosen due to the higher energy of the photogenerated hot holes compared to the ones generated at the dipolar peak (800-1000 nm), in order to maximize the probability of driving the oxidation of $MnSO_4$ and the comparability with the previous experiment. Illumination of the Au nano-triangles was also conducted at a

different wavelength (808 nm, 0.11 W/cm^2 for 1h), but no deposition of MnO_x was observed (Figure 4.18). This could be explained by the lower energy of the photogenerated holes at this excitation wavelength, which is not enough to drive the chemical reaction in similar time scales as at 638 nm.

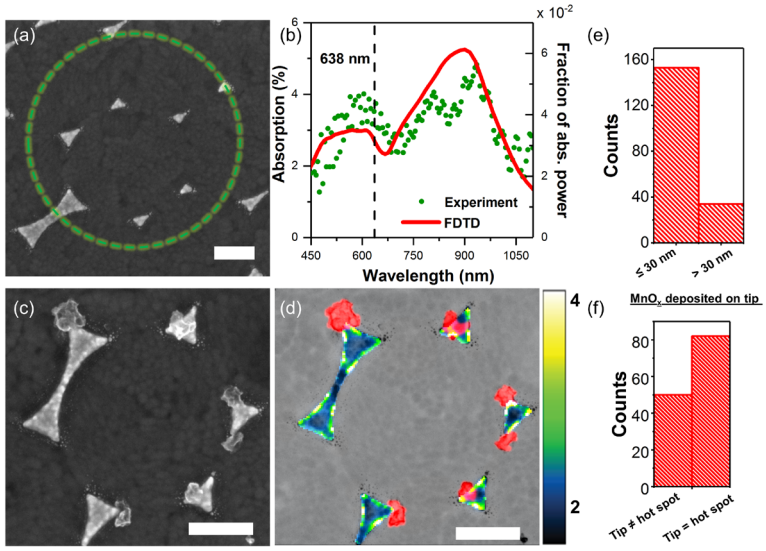

Figure 4.4. a) SEM image of Au nano-triangles on TiO_2/ITO/glass prepared with nanosphere lithography. Green circle corresponds to the illumination spot during absorption measurements. b) Absorption spectra (green dots) of region in the green circle in image (a) retrieved with integrating sphere microscopy and average FDTD simulated fraction of absorbed power spectrum of 163 Au nanotriangles (red solid line) which were imported to the simulation file as SEM images, c) SEM image of Au nano-triangles after illumination for 10 min at 638 nm in $MnSO_4$/$NaIO_3$ (0.01 M / 0.02 M, pH 5.2), d) Overlap of simulated absorbed power map (see color bar) and location of MnO_x deposition sites (red). More data sets can be found in the SI (Figure 4.17) Amount of MnO_x deposits on 163 Au nanotriangles correlated with e) the distance from a plasmonic hot-spot. f) Amount of MnO_x deposits on a nano-triangle's tip and correlation with the nature of the tip as a hot-spot. All scale bars are 200 nm.

SEM images of the Au nano-triangles after the illumination of the samples were compared with the simulated hot-spots to investigate any correlation of the latter with the deposition sites of the cocatalyst. From a population of 163 nano-triangles, with 82 % of them covered with one or two MnO_x deposits, 57 % of the deposited MnO_x was directly overlapping with a plasmonic hotspot from the corresponding FDTD simulation (Figure 4.19a). When we account for a typical hot-hole diffusion length radius of 30 nm in Au,[231] 80 % of the MnO_x deposits are located within this distance (Figure 4.4e).

This may indicate that the initial nucleation site of the catalyst particle may be located within 30 nm of the hotspot, and acts as a hot-hole trap for subsequently created hot holes. Therefore we see only one or two MnO_x deposits per particle. It is also observed that most of the MnO_x deposits are located on an Au nano-triangle tip (Figure 4.19b). However, the majority of the tips with a MnO_x deposit are indeed a plasmonic hot-spot (Figure 4.4f) originating from the optical field enhancement due to the sharp curvature.

4.3 Conclusions

In summary, we showed that both types of hot-carriers generated in plasmonic nanostructures can be utilized for simultaneous reduction and oxidation of different cocatalyst species. Hot-hole assisted deposition of Mn oxides and hot-electron assisted formation of Pt species was conducted on plasmonic Au nano-islands excited at their surface plasmon resonance. Au nano-triangles were also used as a platform to investigate the spatial localization of the deposition of the cocatalyst materials driven by hot-hole oxidation reactions. We showed that deposition sites can be controlled by engineering the location of plasmonic hot-spots, with 80% fidelity. Such solid-state deposition can be used to visualize hot-carrier dynamics, including diffusion and contribute to the light-driven design of hierarchical nanomaterials.

4.4 Supporting information

4.4.1 General

Chemicals were purchased from major chemical suppliers and used as received. Sample characterization was done with scanning electron microscopy (FEI Verios 460, acceleration beam voltage 5 kV, beam current 100 pA) and energy-dispersive x-ray spectrometry (EDS, Oxford Instruments, acceleration beam voltage 25 kV, beam current 100 pA). X-ray photoelectron spectroscopy (XPS) was performed using a Kα setup from Thermo Fisher Scientific that is equipped with a detector at normal incidence. The composition of the top surface was studied in a vacuum environment of $1x10^{-8}$ mbar where monochromatic Al-Kα radiation has been used to investigate the surface. CasaXPS was used for baseline and peak fitting (with a Voigt funtion in a Shirley background). A UV/Vis/NIR spectrophotometer (PerkinElmer, L750) was used for acquiring the absorbance spectra.

4.4.2 Atomic Layer Deposition

ITO/glass substrates (15 x 15 mm) were cleaned with detergent, rinsed with demineralized water, acetone, isopropanol and dried with a N_2 stream. A thin TiO_2 layer was then deposited on the substrates with atomic layer deposition in a home-built system.

The first few millimeters of the sample's surface were covered with a Kapton tape, in order to leave a part of the surface conductive to do the electrical connections during the photoelectrochemical characterization of the samples. The samples were positioned in the chamber on a stainless steel plate, heated up to 100 °C, and and $TiCl_4$ ($\geq$ 99.995 %, Sigma Aldrich) and H_2O (MilliQ) vapor pulses were injected with 18 seconds delay in between each pulse (of a 20 ms duration for both $TiCl_4$ and H_2O). The base pressure of the system was 0.04-0.07 mbar while during the deposition the pressure was kept at 1.1 mbar with an influx of N_2. After the deposition of around 22 nm of TiO_2 which corresponded to 300 cycles (0.07 nm/cycle) the samples were annealed in a tube oven in air for 3 h at 350 °C and a rate of 11 °C/min.

4.4.3 Au nano-islands preparation

The formation of the plasmonic Au nano-islands on the TiO_2 surface was achieved by starting with the sputtering (Leica EM ACE600 sputter coater) of an 8 nm Au film with a 0.33 nm/sec deposition rate. The current of the process was adjusted to make sure that the deposition rate is every time the same and it was varying between 30-100 mA. The thickness of the deposited Au film was monitored through a quartz crystal mounted inside the sputter coater. The annealing of the Au thin film was conducted in a tube oven in air, which was brought to 300 °C with a 9.2 °C/ min heating rate, kept at a constant temperature for 1 h to form the Au nano-islands and then allowed to cool down to room temperature.

4.4.4 Au nano-triangles preparation

The fabrication of Au nanotriangles was achieved by nanosphere lithography on the TiO_2/ITO/glass substrates. A monolayer of carboxylated polystyrene (PS) spheres (bought from microParticles GmbH, Germany) with a diameter of 527 nm was deposited via convective assembly in a hexagonal packing on the aforementioned substrates using a home-build setup. The sample was held by vacuum on a motorized stage while a hydrophobic 0.5 mm microscopy slide was kept $\sim$ 100 μm above it at an angle of 5° with the horizontal. 10 μl of the suspension of PS spheres in aqueous solution (1 wt. %) was dispensed at the interface between the substrate and the glass blade and as a result of the capillary forces it was quickly sucked between them. A Peltier heating element is attached underneath the vacuum stage to control the temperature and it was maintained at 23 °C for the entire process of convective assembly. The motorized stage moved the substrate against the glass blade with a speed of 500 – 600 μm/min which yielded monolayer of PS spheres of the order of mm^2 area. The system is also coupled to a microscope that allows control over the whole process, and the deposition parameters can be controlled by an in-house written software. After the assembly of the PS spheres on the sample, 30 nm of Au was evaporated at a rate of 0.01 nm/s with a thermal evaporator (Angstrom Engineering). Finally, the PS spheres were removed from the substrate

after $\sim$ 4 min of sonication in chloroform ($CHCl_3$) leaving only the Au layer in-between the spheres, which corresponded to Au nanotriangles of around 112 $\pm$ 18 nm edge. The samples were rinsed with H_2O before photodeposition.

4.4.5 Photoelectrochemical measurements

Photoelectrochemical measurements were conducted in a three-electrode photoelectrochemical cell connected to a potentiostat (Biologic, SP-200). The sample was connected electrically to the potentiostat, as the working electrode, with a conductive aluminum tape (Advance Tapes AT521) placed on the first 2 mm of the sample (TiO_2 uncoated). A leakless Ag/AgCl electrode (Mengel Engineering ED-ET072) was used as the reference and a Pt wire acted as the counter electrode. After each photoelectrochemical measurement the samples were rinsed with H_2O and dried with N_2.

4.4.6 Wavelength dependent measurements (IPCE)

For the wavelength dependent measurements, which were used for the calculation of the IPCE values, the same PEC cell was used as before (see photoelectrochemical measurements). The excitation source was a supercontinuum laser (Fianium WL-SC-390-3), which was made monochromatic using an acousto-optical tunable filter (AOTF-Crystal Technologies) and the illumination of the sample was performed from the back side (ITO/glass). The potentiostat was connected with the PEC cell and with a lock-in amplifier (Stanford Research Systems SR830). The current signal detected from the sample was sent through the potentiostat to the lock-in amplifier (100 ms sensitivity, $\pm$ 10 V output) with a DB-9 to 8 BNC multi-coaxial adapter cable. The lock-in amplifier isolated the signal coming from the light, which was chopped with a 70 Hz frequency, far from any other noise of the system. The final signal was sent back to the potentiostat, where the recorded photocurrent was plotted as a function of time. Every 20 seconds the incident beam was blocked and every 40 seconds the excitation wavelength was redshifted by 20 nm, in order for the measurement per wavelength to become more visible.

4.4.7 FDTD simulations and image processing

23 SEM images (1536×1103 pixels) were acquired of Au nanotriangles using detectors sensitive for secondary electrons and backscattered electrons (Figure 4.16b and Figure 4.16c). Comparing both images revealed the accurate location of Mn deposits. The backscattered electron image provided the accurate structural dimensions of the Au nanotriangles for FDTD simulations and were image-processed as followed using ImageJ 2.0 software. The grey-scale images were first converted to binary using an appropriate grey-value threshold, and image noise was removed using the despeckle algorithm (3×3 pixel median value filter). Small Au defects around the triangles were removed using

a 4 pixel Gaussian blur, converting once more to binary values with an appropriate grey-value threshold, and minor manual detailing to remove any remaining artifacts. The binary image was imported in Lumerical (using image import) and the particle height was set to 30 nm, according to AFM-retrieved values. The absorbed power in the structures was simulated using an advanced absorbed power monitor and total field scattered field (TFSF) type source at $\lambda = 638$ nm with the experiment-matching polarization. A 5 nm mesh was used. The absorbed power map was integrated over the height of the particles (Figure 4.16d) and was overlaid with a map of Mn deposition sites (Figure 4.16e). Each individual nanotriangle (163 in total) was manually scored on (i) number of Mn deposits, (ii) Mn deposit location (on tip, side, or top), (iii) Mn deposit size in nm^2, (iv) whether the Mn deposit was attached to the Au nanoparticle, (v) position overlap between Mn deposition site and absorption hotspot, and (vi) distance of Mn deposit to absorption hotspot.

4.4.8 Incident photon to current efficiency (IPCE) calculation

The IPCE values were calculated from the following equation:

$$IPCE(\%) = \frac{j_{\mathrm{ph}}(mA/cm^2) * 1241(V * nm)}{P(mW/cm^2) * \lambda(nm)} * 100$$

, where $j_{\mathrm{ph}}(\mathrm{mA/cm^2})$ is the average photocurrent retrieved from Figure 4.18 for each wavelength, 1241 (V×nm) represents a multiplication of h (Planck's constant) and c (the speed of light) divided by q (the electron charge) , P ($\mathrm{mW/(cm^2)}$) is the power intensity of each wavelength measured with a Si photodiode power sensor (Thorlabs S120C, see Table 3.1 for more information, with surface area of the photoelectrode equal to 0.28 $\mathrm{cm^2}$) and λ (nm) is the wavelength.

4.4.9 Supplementary figures

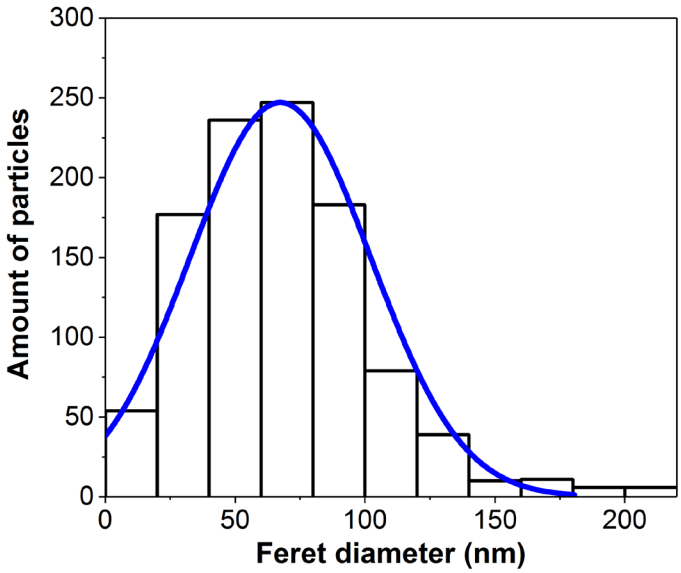

Figure 4.5. Particle distribution curve derived from SEM images of Au nanoislands prepared on TiO_2/ITO/glass substrate, where Feret diameter corresponds to the longest measured distance between any two points for every nanostructure.

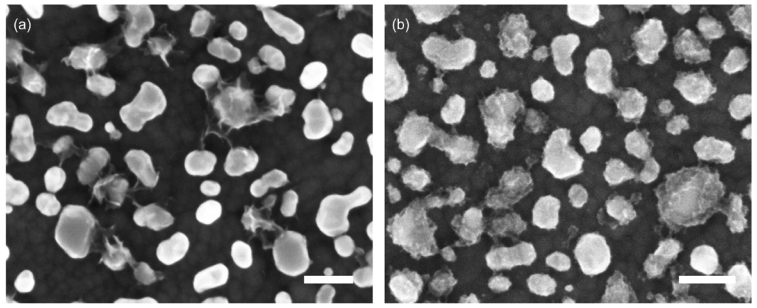

Figure 4.6. SEM image of TiO_2/Au nano-islands after a) 10 min of illumination at 638 nm (0.5 W/cm^2) in $MnSO_4/NaIO_3$ (pH 5.2, 0.01 M/0.02 M, aqueous solution) and b) 20 min) in $MnSO_4/H_2PtCl_6$ (pH 3.8, 0.01 M/0.04 mM, 0.1 M Na_2SO_4 aqueous solution). Scale bars are 200 nm.

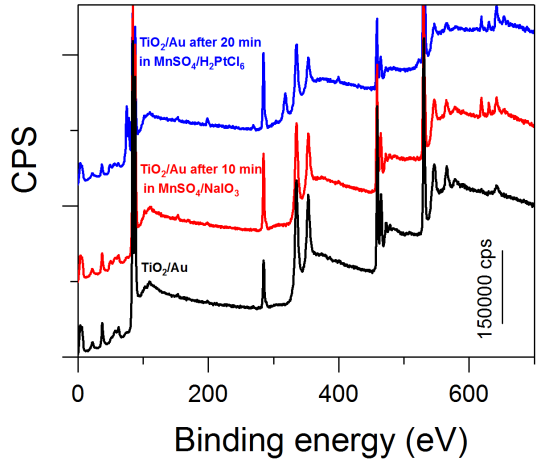

Figure 4.7. XPS survey data for 3 different samples; TiO_2/Au nano-islands as prepared (black curve), TiO_2/Au nano-islands after 10 min of illumination (red curve) at 638 nm (0.5 W/cm^2) in $MnSO_4/NaIO_3$ (pH 5.2, 0.01 M/0.02 M, aqueous solution) and 2h (blue curve) in $MnSO_4/H_2PtCl_6$ (pH 3.8, 0.01 M/0.04 mM, 0.1 M Na_2SO_4 aqueous solution).

Binding Energies (eV)		
XPS region	**Au on TiO_2 after 10 min in $MnSO_4/NaIO_3$**	**Au on TiO_2 after 2 h in $MnSO_4/H_2PtCl_6$**
Mn $2p_{3/2}$	641.7	641.7
	644.9	644.5
Mn $2p_{1/2}$	653.5	653.6
Pt $4f_{7/2}$	-	72.9
	-	75.0
Pt $4f_{5/2}$	-	76.2
	-	78.4
Au $4p_{1/2}$	642.55	642.6

Table 4.1. Binding energies of the Mn 2p, Pt 4f and Au 4p XPS regions of Au nano-islands on TiO_2 after 10 min of illumination at 638 nm (0.5 W/cm^2) in $MnSO_4/NaIO_3$ (pH 5.2, 0.01 M/0.02 M, aqueous solution) and 2h in $MnSO_4/H_2PtCl_6$ (pH 3.8, 0.01 M/0.04 mM, 0.1 M Na_2SO_4 aqueous solution).

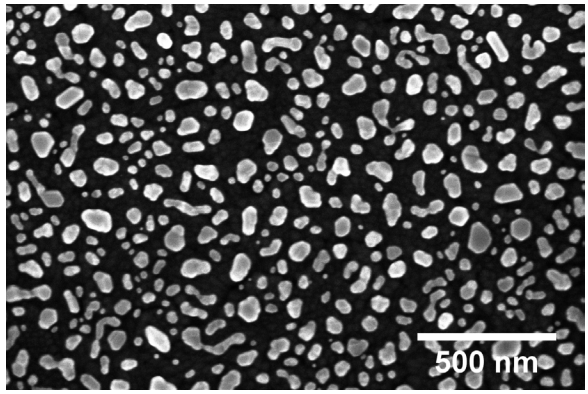

Figure 4.8. SEM image of Au nano-islands on TiO_2 after being in presence of $MnSO_4/NaIO_3$ (pH 5.2, 0.01 M/0.02 M, aqueous solution) for 30 min in the dark.

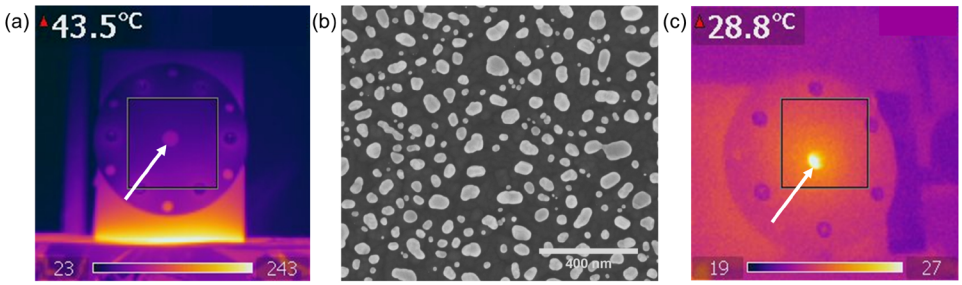

Figure 4.9. a) Temperature profile of the back side of the sample (sample's location is indicated with the arrow) while heated up to 40 °C. b) SEM image of Au nano-islands on TiO_2 after a heat control measurement in $MnSO_4/NaIO_3$ (pH 5.2, 0.01 M/0.02 M, aqueous solution), where the temperature was kept at around 40 °C for 30 min. During the experiment the temperature was controlled with a thermocouple in the solution and the temperature was also verified with an IR camera (temperature within the squared area in (a)). c) Temperature on the surface of the sample during illumination with a 638 nm laser (0.5 W/cm^2).

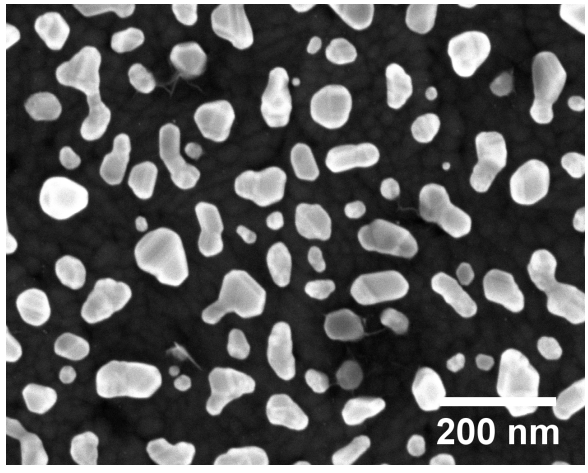

Figure 4.10. SEM image of Au nano-islands after illumination for 10 min at 638 nm (0.5W/cm^2) in $MnSO_4$ (pH 5.2, 0.01 M, aqueous solution) but without an electron scavenger ($NaIO_3$).

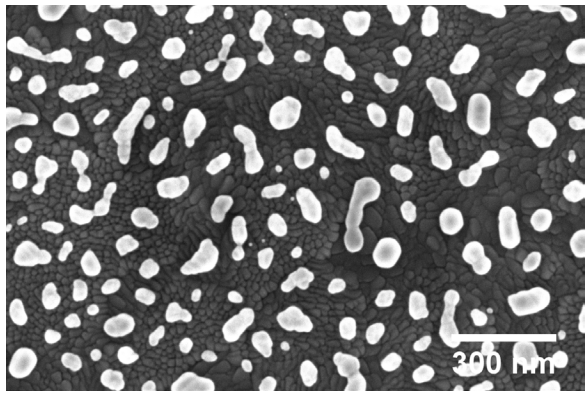

Figure 4.11. SEM image of Au nano-islands on ITO/glass (without TiO_2 this time) after illumination for 6 h at 638 nm ($0.5W/cm^2$) in $MnSO_4$ /$NaIO_3$ (pH 5.2, 0.01 M/0.02 M, aqueous solution). No deposition of MnO_x was observed here which shows the importance of the TiO_2 layer.

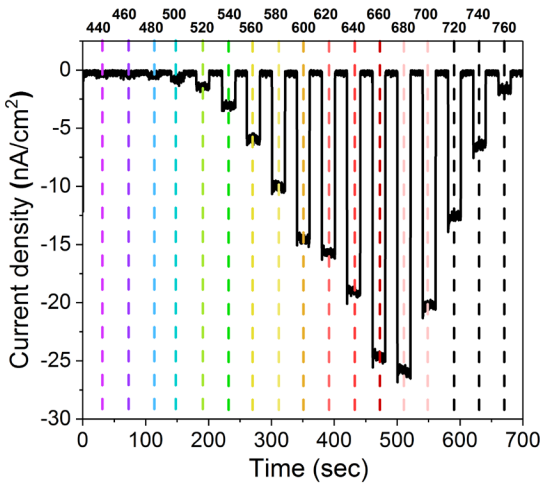

Figure 4.12. Photocurrent density vs time at different excitation wavelengths of Au nano-islands on TiO_2 in presence of $MnSO_4$ (pH 5.2, 0.01 M, aqueous solution) at applied potential 0.2 V vs Ag/AgCl. The dashed lines correspond to a different excitation wavelength, which is noted on the top side of the graph (in nm).

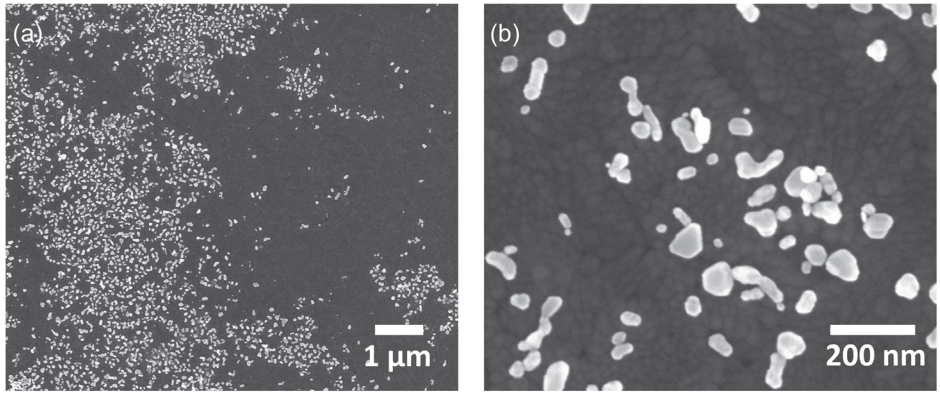

Figure 4.13. a) and b) Au nano-islands on TiO_2 after voltage sweeping measurements in $MnSO_4$ (pH 5.2, 0.01 M, aqueous solution) excited at 638 nm.

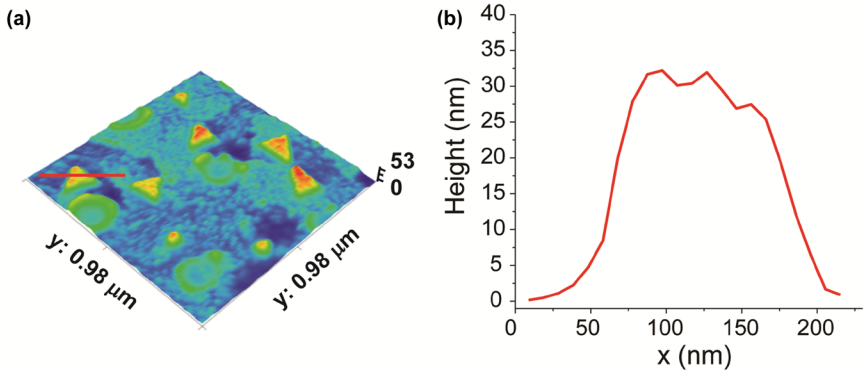

Figure 4.14. a) AFM map of Au nano-triangles on TiO_2 and b) a thickness spectrum of an Au nano-triangle (marked with a red solid line on (a)) retrieved also from the AFM measurements.

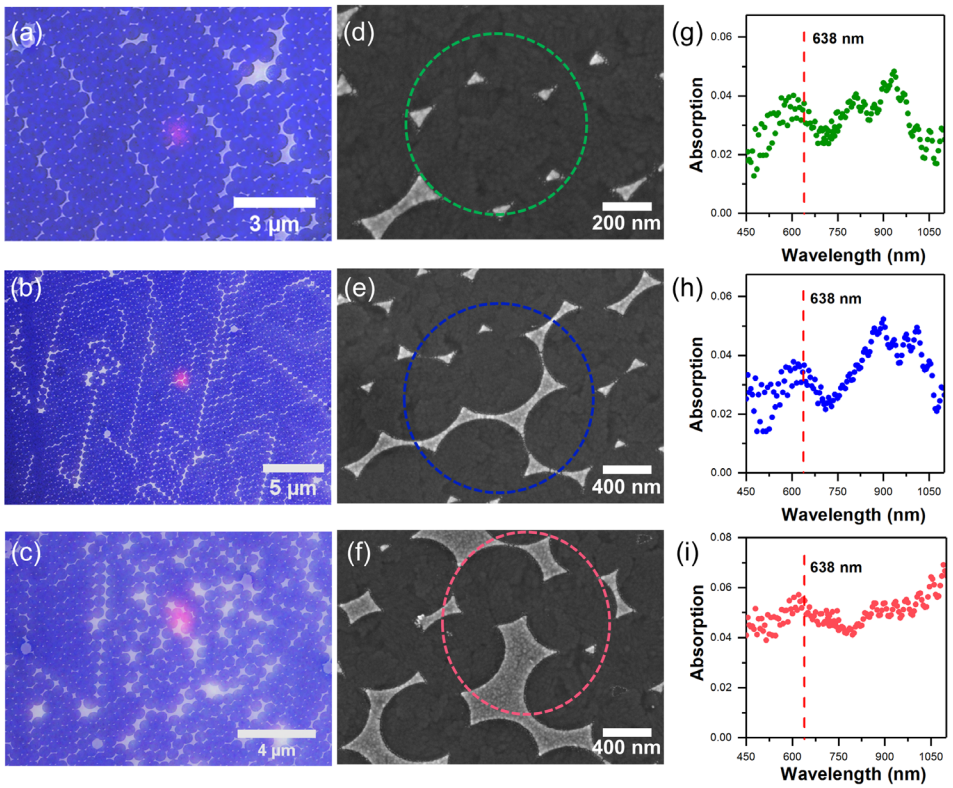

Figure 4.15. a),b) and c) Overlays of SEM images and bright field microscopy camera images of 3 different regions of an Au nanotriangles sample prepared with nanosphere lithography on TiO_2 used for identification of the laser spot (red area). d), e) and f) Higher magnification SEM images of the areas which are illuminated by the laser in a), b) and c) respectively. g), h) and i) the corresponding absorption spectrum of the three different areas d), e) and f) respectively measured with integrating sphere microscopy.

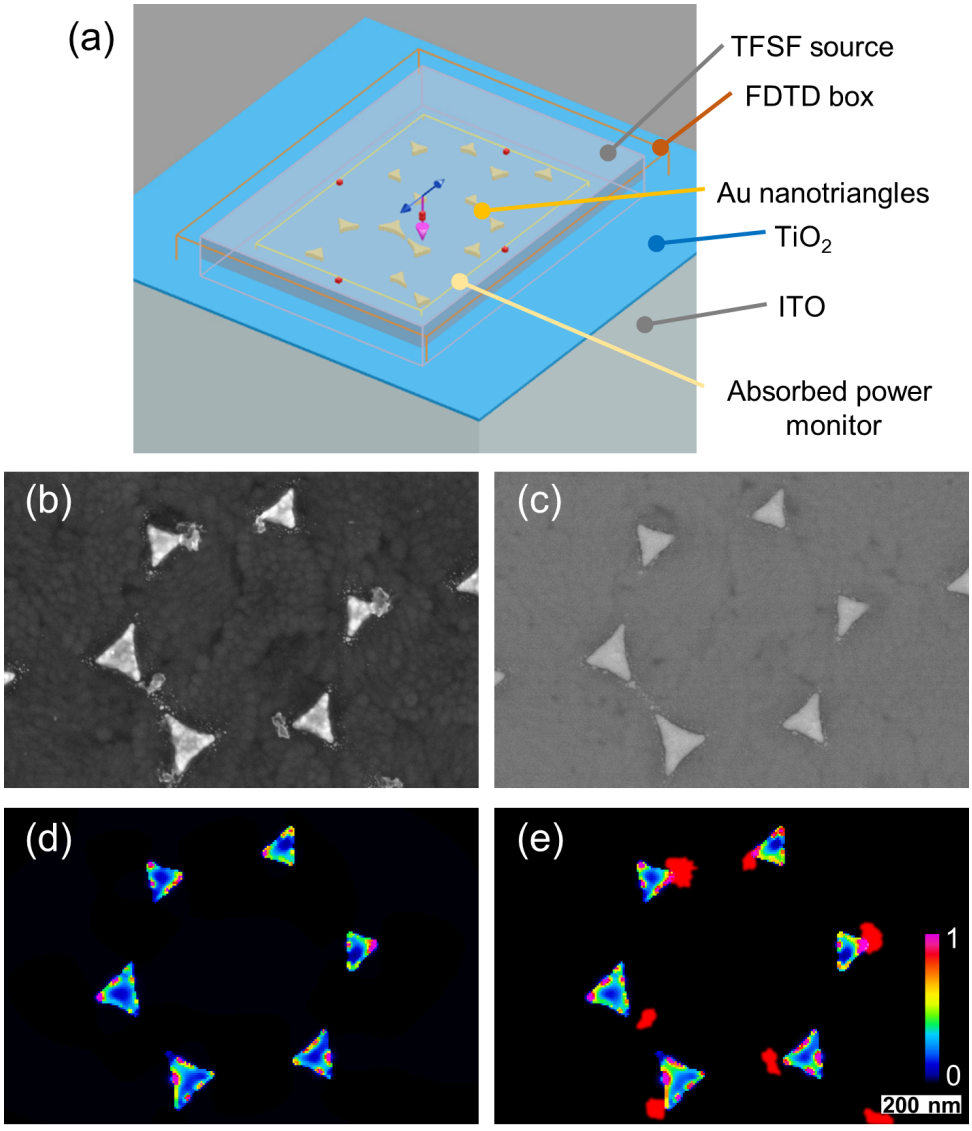

Figure 4.16. a) Simulation space screenshot from Lumerical software with indicated simulation elements. b/c) Secondary electron (b) and backscattered electron (c) SEM images of Au nanotriangles with MnO_x deposits. d) FDTD simulated absorbed power map in Au nanotriangles at 638 nm excitation at horizontal polarization. e) Overlap of simulated absorbed power map (panel d) and location of MnO_x deposition sites (red). Scale bar is 200 nm for panels b-e.

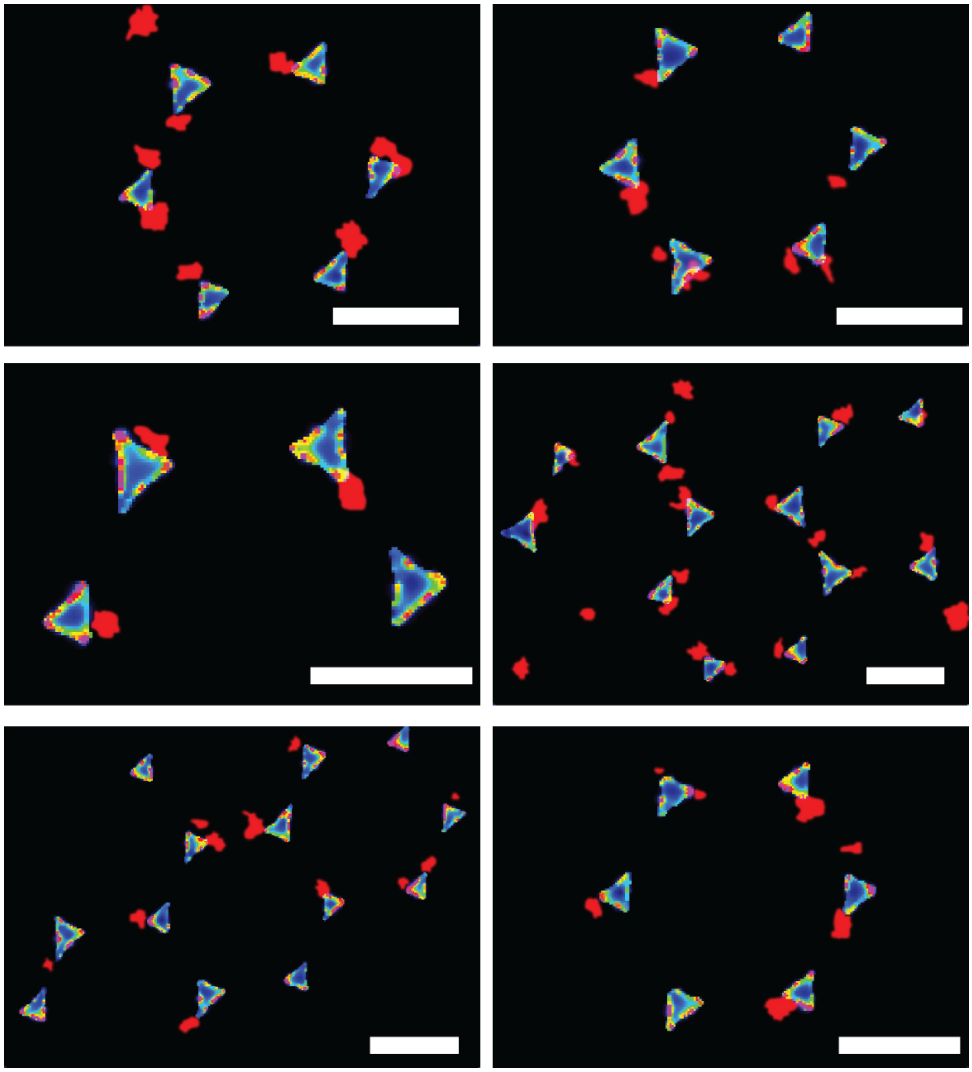

Figure 4.17. More examples of overlaps of simulated absorbed power maps and location of MnO_x deposition sites (red) on Au nano-triangles on TiO_2. Scale bars are 300 nm

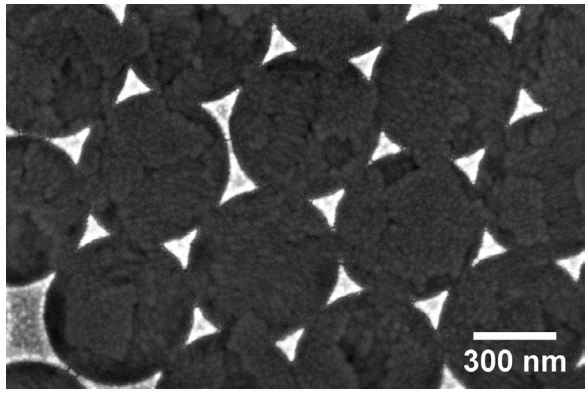

Figure 4.18. Au nano-triangles prepared with nanosphere lithography on TiO_2 after illumination for 1h at 808 nm (0.11 W/cm^2) in $MnSO_4/NaIO_3$ (pH 5.2, 0.01 M/0.02 M, aqueous solution).

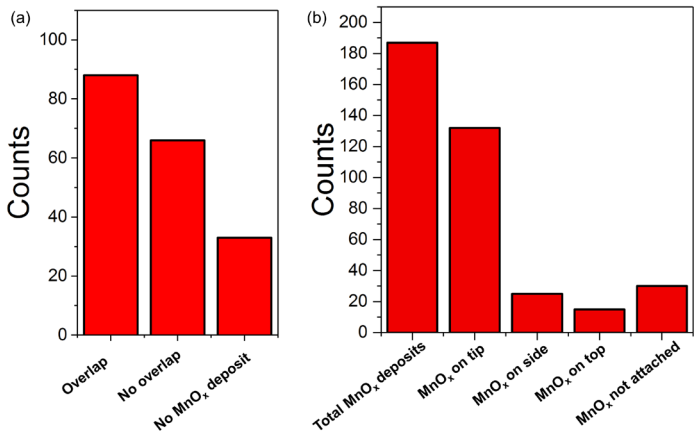

Figure 4.19. Statistical analysis of 163 Au nano-triangles on TiO_2 retrieved from FDTD simulations and SEM image processing (Figure 4.16 and Figure 4.17) to identify the MnO_x deposition sites and correlate them with the plasmonic hot-spots. a) Amount of MnO_x deposits overlapping with a plasmonic hot-spot; not overlapping with a plasmonic hot-spot and amount of nano-triangles without any deposit (some nano-triangles had 2 MnO_x deposits) b) Amount of total MnO_x deposits on the 163 Au nano-triangles, amount of MnO_x deposits only on a tip (MnO_x on tip), a side (Mn on side), the top surface (MnO_x on top) of a nano-triangle and when the deposit was not attached the nanostructure (MnO_x not attached).

References

1. Rayleigh, L. XXXIV. On the transmission of light through an atmosphere containing small particles in suspension, and on the origin of the blue of the sky. *Philosophical Magazine* **47,** 375–384 (1899).
2. Bohren, C. F. & Huffman, D. R. *Absorption and scattering of light by small particles* (John Wiley & Sons, 1983).
3. Lee, K. S. & El-Sayed, M. A. Gold and silver nanoparticles in sensing and imaging: Sensitivity of plasmon response to size, shape, and metal composition. *Journal of Physical Chemistry B* **110,** 19220–19225 (2006).
4. Koenderink, A. F., Alù, A. & Polman, A. Nanophotonics: Shrinking light-based technology. *Science* **348,** 516–521 (2015).
5. Colson, P., Henrist, C. & Cloots, R. Nanosphere lithography: A powerful method for the controlled manufacturing of nanomaterials. *Journal of Nanomaterials* **2013** (2013).
6. Xu, X., Yang, Q., Wattanatorn, N., Zhao, C., Chiang, N., Jonas, S. J. & Weiss, P. S. Multiple-Patterning Nanosphere Lithography for Fabricating Periodic Three-Dimensional Hierarchical Nanostructures. *ACS Nano* **11,** 10384–10391 (2017).
7. Verschuuren, M. A., Megens, M., Ni, Y., Van Sprang, H. & Polman, A. Large area nanoimprint by substrate conformal imprint lithography (SCIL). *Advanced Optical Technologies* **6,** 243–264 (2017).
8. Yin, Y. & Alivisatos, A. P. Colloidal nanocrystal synthesis and the organic-inorganic interface. *Nature* **437,** 664–670 (2005).
9. Shevchenko, E. V., Talapin, D. V., Kotov, N. A., O'Brien, S. & Murray, C. B. Structural diversity in binary nanoparticle superlattices. *Nature* **439,** 55–59 (2006).
10. Tao, A. R., Habas, S. & Yang, P. Shape control of colloidal metal nanocrystals. *Small* **4,** 310–325 (2008).

11. Wall, M. A., Harmsen, S., Pal, S., Zhang, L., Arianna, G., Lombardi, J. R., Drain, C. M. & Kircher, M. F. Surfactant-Free Shape Control of Gold Nanoparticles Enabled by Unified Theoretical Framework of Nanocrystal Synthesis. *Advanced Materials* **29,** 1605622 (2017).
12. Xia, Y., Xiong, Y., Lim, B. & Skrabalak, S. E. Shape-controlled synthesis of metal nanocrystals: Simple chemistry meets complex physics? *Angewandte Chemie - International Edition* **48,** 60–103 (2009).
13. Xia, Y., Xia, X. & Peng, H. C. Shape-Controlled Synthesis of Colloidal Metal Nanocrystals: Thermodynamic versus Kinetic Products. *Journal of the American Chemical Society* **137,** 7947–7966 (2015).
14. Fang, M., Dong, G., Wei, R. & Ho, J. C. Hierarchical nanostructures: Design for sustainable water splitting. *Advanced Energy Materials* **7,** 1700559 (2017).
15. Martin-Martinez, F. J., Jin, K., López Barreiro, D. & Buehler, M. J. The rise of hierarchical nanostructured materials from renewable sources: Learning from nature. *ACS Nano* **12,** 7425–7433 (2018).
16. Hutter, E. & Fendler, J. H. Exploitation of localized surface plasmon resonance. *Advanced Materials* **16,** 1685–1706 (2004).
17. Amendola, V., Pilot, R., Frasconi, M., Maragò, O. M. & Iatì, M. A. Surface plasmon resonance in gold nanoparticles: A review. *Journal of Physics Condensed Matter* **29** (2017).
18. Mayer, K. M. & Hafner, J. H. Localization Surface Plasmon Resonance. *Chemical Society Reviews* **8,** 435–437 (2009).
19. Maier, S. A. & Atwater, H. A. Plasmonics: Localization and guiding of electromagnetic energy in metal/dielectric structures. *Journal of Applied Physics* **98,** 011101 (2005).
20. Boriskina, S. V., Ghasemi, H. & Chen, G. Plasmonic materials for energy: From physics to applications. *Materials Today* **16,** 375–386 (2013).
21. Stockman, M. I. Nanoplasmonics: past, present, and glimpse into future. *Optics Express* **19,** 22029 (2011).
22. Hartland, G. V., Besteiro, L. V., Johns, P. & Govorov, A. O. What's so Hot about Electrons in Metal Nanoparticles? *ACS Energy Letters* **2,** 1641–1653 (2017).
23. Link, S. & El-Sayed, M. A. Shape and size dependence of radiative, non-radiative and photothermal properties of gold nanocrystals. *International Reviews in Physical Chemistry* **19,** 409–453 (2000).
24. Kelly, K. L., Coronado, E., Zhao, L. L. & Schatz, G. C. The optical properties of metal nanoparticles: The influence of size, shape, and dielectric environment. *Journal of Physical Chemistry B* **107,** 668–677 (2003).

25. Barnes, W. L. Particle plasmons: Why shape matters. *American Journal of Physics* **84,** 593–601 (2016).

26. Halas, N. J., Lal, S., Chang, W. S., Link, S. & Nordlander, P. Plasmons in strongly coupled metallic nanostructures. *Chemical Reviews* **111,** 3913–3961 (2011).

27. Huang, Y., Ma, L., Hou, M., Li, J., Xie, Z. & Zhang, Z. Hybridized plasmon modes and near-field enhancement of metallic nanoparticle-dimer on a mirror. *Scientific Reports* **6** (2016).

28. Kelly, K. L., Coronado, E., Zhao, L. L. & Schatz, G. C. The optical properties of metal nanoparticles: The influence of size, shape, and dielectric environment. *Journal of Physical Chemistry B* **107,** 668–677 (2003).

29. Krenn, J. R., Schider, G., Rechberger, W., Lamprecht, B., Leitner, A., Aussenegg, F. R. & Weeber, J. C. Design of multipolar plasmon excitations in silver nanoparticles. *Applied Physics Letters* **77,** 3379–3381 (2000).

30. Raziman, T. V. & Martin, O. J. F. Polarisation charges and scattering behaviour of realistically rounded plasmonic nanostructures. *Optics Express* **21,** 21500 (2013).

31. Hrelescu, C., Sau, T. K., Rogach, A. L., Jäckel, F., Laurent, G., Douillard, L. & Charra, F. Selective excitation of individual plasmonic hotspots at the tips of single gold nanostars. *Nano Letters* **11,** 402–407 (2011).

32. He, Y. & Shi, G. Surface plasmon resonances of silver triangle nanoplates: Graphic assignments of resonance modes and linear fittings of resonance peaks. *Journal of Physical Chemistry B* **109,** 17503–17511 (2005).

33. Fletcher, G., Arnold, M. D., Pedersen, T., Keast, V. J. & Cortie, M. B. Multipolar and dark-mode plasmon resonances on drilled silver nano-triangles. *Optics Express* **23,** 18002 (2015).

34. Brongersma, M. L., Halas, N. J. & Nordlander, P. Plasmon-induced hot carrier science and technology. *Nature Nanotechnology* **10,** 25–34 (2015).

35. Li, W. & Valentine, J. G. Harvesting the loss: Surface plasmon-based hot electron photodetection. *Nanophotonics* **6,** 177–191 (2017).

36. Besteiro, L. V., Kong, X. T., Wang, Z., Hartland, G. & Govorov, A. O. Understanding Hot-Electron Generation and Plasmon Relaxation in Metal Nanocrystals: Quantum and Classical Mechanisms. *ACS Photonics* **4,** 2759–2781 (2017).

37. Hegde, R. S. & Khatua, S. Hot Carrier Generation in Plasmonic Nanostructures. *Nanoelectronics,* 289–315 (2019).

38. Brown, A. M., Sundararaman, R., Narang, P., Goddard, W. A. & Atwater, H. A. Nonradiative plasmon decay and hot carrier dynamics: Effects of phonons, surfaces, and geometry. *ACS Nano* **10,** 957–966 (2016).

39. Liu, T., Besteiro, L. V., Wang, Z. & Govorov, A. O. Generation of hot electrons in nanostructures incorporating conventional and unconventional plasmonic materials. *Faraday Discussions* **214,** 199–213 (2019).

40. Knoesel, E., Hotzel, A. & Wolf, M. Ultrafast dynamics of hot electrons and holes in copper: Excitation, energy relaxation, and transport effects. *Physical Review B - Condensed Matter and Materials Physics* **57,** 12812–12824 (1998).

41. Besteiro, L. V. & Govorov, A. O. Amplified Generation of Hot Electrons and Quantum Surface Effects in Nanoparticle Dimers with Plasmonic Hot Spots. *Journal of Physical Chemistry C* **120,** 19329–19339 (2016).

42. Harutyunyan, H., Martinson, A. B., Rosenmann, D., Khorashad, L. K., Besteiro, L. V., Govorov, A. O. & Wiederrecht, G. P. Anomalous ultrafast dynamics of hot plasmonic electrons in nanostructures with hot spots. *Nature Nanotechnology* **10,** 770–774 (2015).

43. Manjavacas, A., Liu, J. G., Kulkarni, V. & Nordlander, P. Plasmon-induced hot carriers in metallic nanoparticles. *ACS Nano* **8,** 7630–7638 (2014).

44. Urbieta, M., Barbry, M., Zhang, Y., Koval, P., Sánchez-Portal, D., Zabala, N. & Aizpurua, J. Atomic-Scale Lightning Rod Effect in Plasmonic Picocavities: A Classical View to a Quantum Effect. *ACS Nano* **12,** 585–595 (2018).

45. Pavaskar, P., Theiss, J. & Cronin, S. B. Plasmonic hot spots: nanogap enhancement vs focusing effects from surrounding nanoparticles. *Optics Express* **20,** 14656 (2012).

46. Kang, M., Park, S. G. & Jeong, K. H. Repeated Solid-state Dewetting of Thin Gold Films for Nanogap-rich Plasmonic Nanoislands. *Scientific Reports* **5,** 14790 (2015).

47. Liu, J. G., Zhang, H., Link, S. & Nordlander, P. Relaxation of Plasmon-Induced Hot Carriers. *ACS Photonics* **5,** 2584–2595 (2018).

48. Sundararaman, R., Narang, P., Jermyn, A. S., Goddard, W. A. & Atwater, H. A. Theoretical predictions for hot-carrier generation from surface plasmon decay. *Nature Communications* **5** (2014).

49. Kumarasinghe, C. S., Premaratne, M., Bao, Q. & Agrawal, G. P. Theoretical analysis of hot electron dynamics in nanorods. *Scientific Reports* **5,** 12140 (2015).

50. Saavedra, J. R., Asenjo-Garcia, A. & García De Abajo, F. J. Hot-Electron Dynamics and Thermalization in Small Metallic Nanoparticles. *ACS Photonics* **3,** 1637–1646 (2016).

51. Clavero, C. Plasmon-induced hot-electron generation at nanoparticle/metal-oxide interfaces for photovoltaic and photocatalytic devices. *Nature Photonics* **8,** 95–103 (2014).

52. Mubeen, S., Hernandez-Sosa, G., Moses, D., Lee, J. & Moskovits, M. Plasmonic photosensitization of a wide band gap semiconductor: Converting plasmons to charge carriers. *Nano Letters* **11,** 5548–5552 (2011).

53. Govorov, A. O., Zhang, H. & Gun'Ko, Y. K. Theory of photoinjection of hot plasmonic carriers from metal nanostructures into semiconductors and surface molecules. *Journal of Physical Chemistry C* **117,** 16616–16631 (2013).

54. Yamada, Y. & Kanemitsu, Y. Determination of electron and hole lifetimes of rutile and anatase TiO 2 single crystals. *Applied Physics Letters* **101,** 133907 (2012).

55. Tagliabue, G., Jermyn, A. S., Sundararaman, R., Welch, A. J., DuChene, J. S., Pala, R., Davoyan, A. R., Narang, P. & Atwater, H. A. Quantifying the role of surface plasmon excitation and hot carrier transport in plasmonic devices. *Nature Communications* **9** (2018).

56. Wu, K., Rodríguez-Córdoba, W. E., Yang, Y. & Lian, T. Plasmon-induced hot electron transfer from the Au tip to CdS rod in CdS-Au nanoheterostructures. *Nano Letters* **13,** 5255–5263 (2013).

57. Cushing, S. K., Li, J., Bright, J., Yost, B. T., Zheng, P., Bristow, A. D. & Wu, N. Controlling Plasmon-Induced Resonance Energy Transfer and Hot Electron Injection Processes in Metal@TiO2 Core-Shell Nanoparticles. *Journal of Physical Chemistry C* **119,** 16239–16244 (2015).

58. Shan, H., Yu, Y., Wang, X., Luo, Y., Zu, S., Du, B., Han, T., Li, B., Li, Y., Wu, J., Lin, F., Shi, K., Tay, B. K., Liu, Z., Zhu, X. & Fang, Z. Direct observation of ultrafast plasmonic hot electron transfer in the strong coupling regime. *Light: Science and Applications* **8,** 2047–7538 (2019).

59. Knight, M. W., Wang, Y., Urban, A. S., Sobhani, A., Zheng, B. Y., Nordlander, P. & Halas, N. J. Embedding plasmonic nanostructure diodes enhances hot electron emission. *Nano Letters* **13,** 1687–1692 (2013).

60. Leenheer, A. J., Narang, P., Lewis, N. S. & Atwater, H. A. Solar energy conversion via hot electron internal photoemission in metallic nanostructures: Efficiency estimates. *Journal of Applied Physics* **115,** 134301 (2014).

61. Zhang, Y., Yam, C. & Schatz, G. C. Fundamental Limitations to Plasmonic Hot-Carrier Solar Cells. *Journal of Physical Chemistry Letters* **7,** 1852–1858 (2016).

62. Ng, C., Cadusch, J. J., Dligatch, S., Roberts, A., Davis, T. J., Mulvaney, P. & Gómez, D. E. Hot Carrier Extraction with Plasmonic Broadband Absorbers. *ACS Nano* **10,** 4704–4711 (2016).

63. Furube, A., Du, L., Hara, K., Katoh, R. & Tachiya, M. Ultrafast plasmon-induced electron transfer from gold nanodots into TiO2 nanoparticles. *Journal of the American Chemical Society* **129,** 14852–14853 (2007).

64. Shiraishi, Y., Yasumoto, N., Imai, J., Sakamoto, H., Tanaka, S., Ichikawa, S., Ohtani, B. & Hirai, T. Quantum tunneling injection of hot electrons in Au/TiO2 plasmonic photocatalysts. *Nanoscale* **9,** 8349–8361 (2017).

65. Tian, Y. & Tatsuma, T. Mechanisms and applications of plasmon-induced charge separation at TiO2 films loaded with gold nanoparticles. *Journal of the American Chemical Society* **127,** 7632–7637 (2005).

66. Fountaine, K. T., Whitney, W. S. & Atwater, H. A. Resonant absorption in semiconductor nanowires and nanowire arrays: Relating leaky waveguide modes to Bloch photonic crystal modes. *Journal of Applied Physics* **116** (2014).

67. Abujetas, D. R., Paniagua-Domínguez, R. & Sánchez-Gil, J. A. Unraveling the Janus Role of Mie Resonances and Leaky/Guided Modes in Semiconductor Nanowire Absorption for Enhanced Light Harvesting. *ACS Photonics* **2,** 921–929 (2015).

68. Mokkapati, S., Saxena, D., Tan, H. H. & Jagadish, C. Optical design of nanowire absorbers for wavelength selective photodetectors. *Scientific Reports* **5,** 1–7 (2015).

69. Wu, D., Tang, X., Wang, K. & Li, X. An Analytic Approach for Optimal Geometrical Design of GaAs Nanowires for Maximal Light Harvesting in Photovoltaic Cells. *Scientific Reports* **7** (2017).

70. Wang, B. & Leu, P. W. Tunable and selective resonant absorption in vertical nanowires. *Optics Letters* **37,** 3756 (2012).

71. Seo, K., Wober, M., Steinvurzel, P., Schonbrun, E., Dan, Y., Ellenbogen, T. & Crozier, K. B. Multicolored vertical silicon nanowires. *Nano Letters* **11,** 1851–1856 (2011).

72. Yu, Y. & Cao, L. Leaky mode engineering: A general design principle for dielectric optical antenna solar absorbers. *Optics Communications* **314,** 79–85 (2014).

73. Anttu, N. & Xu, H. Q. Efficient light management in vertical nanowire arrays for photovoltaics. *Optics Express* **21,** A558 (2013).

74. Frederiksen, R., Tutuncuoglu, G., Matteini, F., Martinez, K. L., Fontcuberta, A. & Alarcon-Llado, E. Visual understanding of light absorption and waveguiding in standing nanowires with 3D fluorescence confocal microscopy. *ACS Photonics* **4,** 2235–2241 (2017).

75. Fountaine, K. T., Kendall, C. G. & Atwater, H. A. Near-unity broadband absorption designs for semiconducting nanowire arrays via localized radial mode excitation. *Optics Express* **22,** A930 (2014).

76. Wang, Z. Y., Zhang, R. J., Wang, S. Y., Lu, M., Chen, X., Zheng, Y. X., Chen, L. Y., Ye, Z., Wang, C. Z. & Ho, K. M. Broadband optical absorption by tunable Mie resonances in silicon nanocone arrays. *Scientific Reports* **5** (2015).

77. Landreman, P. E., Chalabi, H., Park, J. & Brongersma, M. L. Fabry-Perot description for Mie resonances of rectangular dielectric nanowire optical resonators. *Optics Express* **24,** 29760 (2016).

78. Grzela, G., Paniagua-Domínguez, R., Barten, T., Van Dam, D., Sánchez-Gil, J. A. & Rivas, J. G. Nanowire antenna absorption probed with time-reversed fourier microscopy. *Nano Letters* **14,** 3227–3234 (2014).

79. Brongersma, M. L., Cui, Y. & Fan, S. Light management for photovoltaics using high-index nanostructures. *Nature Materials* **13,** 451–460 (2014).

80. Garnett, E. & Yang, P. Light trapping in silicon nanowire solar cells. *Nano Letters* **10,** 1082–1087 (2010).

81. Campbell, P. & Green, M. A. Light trapping properties of pyramidally textured surfaces. *Journal of Applied Physics* **62,** 243–249 (1987).

82. Bhattacharya, J., Chakravarty, N., Pattnaik, S., Dennis Slafer, W., Biswas, R. & Dalal, V. L. A photonic-plasmonic structure for enhancing light absorption in thin film solar cells. *Applied Physics Letters* **99,** 131114 (2011).

83. Bermel, P., Luo, C., Zeng, L., Kimerling, L. C. & Joannopoulos, J. D. Improving thin-film crystalline silicon solar cell efficiencies with photonic crystals. *Optics Express* **15,** 16986 (2007).

84. Saleh, B. E. A., Teich, M. C. & Wiley, C. J. in *Fundamentals of Photonics* (1991).

85. Blankenship, R. E., Tiede, D. M., Barber, J., Brudvig, G. W., Fleming, G., Ghirardi, M., Gunner, M. R., Junge, W., Kramer, D. M., Melis, A., Moore, T. A., Moser, C. C., Nocera, D. G., Nozik, A. J., Ort, D. R., Parson, W. W., Prince, R. C. & Sayre, R. T. Comparing photosynthetic and photovoltaic efficiencies and recognizing the potential for improvement. *Science* **332,** 805–809 (2011).

86. Takeda, Y., Ito, T., Motohiro, T., König, D., Shrestha, S. & Conibeer, G. Hot carrier solar cells operating under practical conditions. *Journal of Applied Physics* **105,** 074905 (2009).

87. Schwede, J. W., Bargatin, I., Riley, D. C., Hardin, B. E., Rosenthal, S. J., Sun, Y., Schmitt, F., Pianetta, P., Howe, R. T., Shen, Z. X. & Melosh, N. A. Photon-enhanced thermionic emission for solar concentrator systems. *Nature Materials* **9,** 762–767 (2010).

88. Tisdale, W. A., Williams, K. J., Timp, B. A., Norris, D. J., Aydil, E. S. & Zhu, X. Y. Hot-electron transfer from semiconductor nanocrystals. *Science* **328,** 1543–1547 (2010).

89. Brett, C. in *Piezoelectric Transducers and Applications* 223–239 (Springer Berlin Heidelberg, Berlin, Heidelberg, 2008).

90. Wenderich, K. & Mul, G. Methods, Mechanism, and Applications of Photodeposition in Photocatalysis: A Review. *Chemical Reviews* **116,** 14587–14619 (2016).

91. Cendula, P., David Tilley, S., Gimenez, S., Bisquert, J., Schmid, M., Grätzel, M. & Schumacher, J. O. Calculation of the energy band diagram of a photoelectrochemical water splitting cell. *Journal of Physical Chemistry C* **118,** 29599–29607 (2014).

92. Jiang, C., Moniz, S. J., Wang, A., Zhang, T. & Tang, J. Photoelectrochemical devices for solar water splitting-materials and challenges. *Chemical Society Reviews* **46,** 4645–4660 (2017).

93. Krol, R. in *Photoelectrochemical Hydrogen Production* 13–67 (2012).

94. Hellman, A. & Wang, B. First-principles view on photoelectrochemistry: Water-splitting as case study. *Inorganics* **5,** 37 (2017).

95. Li, J. & Wu, N. *Semiconductor-based photocatalysts and photoelectrochemical cells for solar fuel generation: A review* 2015.

96. Liu, D., Ma, J., Long, R., Gao, C. & Xiong, Y. Silicon nanostructures for solar-driven catalytic applications. *Nano Today* **17,** 96–116 (2017).

97. Joya, K. S., Joya, Y. F., Ocakoglu, K. & Van De Krol, R. Water-splitting catalysis and solar fuel devices: Artificial leaves on the move. *Angewandte Chemie - International Edition* **52,** 10426–10437 (2013).

98. Pinaud, B. A., Benck, J. D., Seitz, L. C., Forman, A. J., Chen, Z., Deutsch, T. G., James, B. D., Baum, K. N., Baum, G. N., Ardo, S., Wang, H., Miller, E. & Jaramillo, T. F. Technical and economic feasibility of centralized facilities for solar hydrogen production via photocatalysis and photoelectrochemistry. *Energy and Environmental Science* **6,** 1983–2002 (2013).

99. Wu, J., Huang, Y., Ye, W. & Li, Y. CO2 Reduction: From the Electrochemical to Photochemical Approach. *Advanced Science* **4,** 1700194 (2017).

100. Opoku, F., Govender, K. K., van Sittert, C. G. C. E. & Govender, P. P. Recent Progress in the Development of Semiconductor-Based Photocatalyst Materials for Applications in Photocatalytic Water Splitting and Degradation of Pollutants. *Advanced Sustainable Systems* **1,** 1700006 (2017).

101. Li, R., Zhang, F., Wang, D., Yang, J., Li, M., Zhu, J., Zhou, X., Han, H. & Li, C. Spatial separation of photogenerated electrons and holes among {010} and {110} crystal facets of BiVO 4. *Nature Communications* **4** (2013).

102. Linic, S., Christopher, P. & Ingram, D. B. Plasmonic-metal nanostructures for efficient conversion of solar to chemical energy. *Nature Materials* **10,** 911–921 (2011).

103. Zhang, Z., Zhang, C., Zheng, H. & Xu, H. Plasmon-Driven Catalysis on Molecules and Nanomaterials. *Accounts of Chemical Research* **52** (2019).

104. Nedrygailov, I. I., Moon, S. Y. & Park, J. Y. Hot electron-driven electrocatalytic hydrogen evolution reaction on metal–semiconductor nanodiode electrodes. *Scientific Reports* **9** (2019).

105. Li, J., Cushing, S. K., Meng, F., Senty, T. R., Bristow, A. D. & Wu, N. Plasmon-induced resonance energy transfer for solar energy conversion. *Nature Photonics* **9,** 601–607 (2015).

106. Hartland, G. V., Besteiro, L. V., Johns, P. & Govorov, A. O. What's so Hot about Electrons in Metal Nanoparticles? *ACS Energy Letters* **2,** 1641–1653 (2017).

107. Zhang, Y., He, S., Guo, W., Hu, Y., Huang, J., Mulcahy, J. R. & Wei, W. D. Surface-Plasmon-Driven Hot Electron Photochemistry. *Chemical Reviews* **118,** 2927–2954 (2018).

108. Kim, S. M., Lee, S. W., Moon, S. Y. & Park, J. Y. The effect of hot electrons and surface plasmons on heterogeneous catalysis. *Journal of Physics Condensed Matter* **28,** 254002 (2016).

109. Zhang, X., Li, X., Zhang, D., Su, N. Q., Yang, W., Everitt, H. O. & Liu, J. Product selectivity in plasmonic photocatalysis for carbon dioxide hydrogenation. *Nature Communications* **8,** 14542 (2017).

110. Gargiulo, J., Berté, R., Li, Y., Maier, S. A. & Cortés, E. From Optical to Chemical Hot Spots in Plasmonics. *Accounts of Chemical Research* **52** (2019).

111. Cortés, E. Efficiency and Bond Selectivity in Plasmon-Induced Photochemistry. *Advanced Optical Materials* **5,** 1700191 (2017).

112. Zhou, L., Swearer, D. F., Zhang, C., Robatjazi, H., Zhao, H., Henderson, L., Dong, L., Christopher, P., Carter, E. A., Nordlander, P. & Halas, N. J. Quantifying hot carrier and thermal contributions in plasmonic photocatalysis. *Science* **362,** 69–72 (2018).

113. Landman, A., Dotan, H., Shter, G. E., Wullenkord, M., Houaijia, A., Maljusch, A., Grader, G. S. & Rothschild, A. Photoelectrochemical water splitting in separate oxygen and hydrogen cells. *Nature Materials* **16,** 646–651 (2017).

114. Shi, Z., Wen, X., Guan, Z., Cao, D., Luo, W. & Zou, Z. Recent progress in photoelectrochemical water splitting for solar hydrogen production. *Annals of Physics* **358,** 236–247 (2015).

115. Benson, E. E., Kubiak, C. P., Sathrum, A. J. & Smieja, J. M. Electrocatalytic and homogeneous approaches to conversion of CO_2 to liquid fuels. *Chemical Society Reviews* **38,** 89–99 (2009).

116. Bak, T., Nowotny, J., Rekas, M. & Sorrell, C. C. *Photo-electrochemical hydrogen generation from water using solar energy. Materials-related aspects* 2002.

117. Li, Z., Feng, J., Yan, S. & Zou, Z. Solar fuel production: Strategies and new opportunities with nanostructures. *Nano Today* **10,** 468–486 (2015).

118. Kamat, P. V. Meeting the clean energy demand: Nanostructure architectures for solar energy conversion. *Journal of Physical Chemistry C* **111,** 2834–2860 (2007).

119. Brongersma, M. L., Cui, Y. & Fan, S. Light management for photovoltaics using high-index nanostructures. *Nature Materials* **13,** 451–460 (2014).

120. Atwater, H. A. & Polman, A. Plasmonics for improved photovoltaic devices. *Materials for Sustainable Energy: A Collection of Peer-Reviewed Research and Review Articles from Nature Publishing Group* **9,** 3–11 (2010).

121. Wang, W., Ramezani, M., Väkeväinen, A. I., Törmä, P., Rivas, J. G. & Odom, T. W. The rich photonic world of plasmonic nanoparticle arrays. *Materials Today* **21,** 303–314 (2018).

122. Cao, L., Fan, P., Vasudev, A. P., White, J. S., Yu, Z., Cai, W., Schuller, J. A., Fan, S. & Brongersma, M. L. Semiconductor nanowire optical antenna solar absorbers. *Nano Letters* **10,** 439–445 (2010).

123. Cao, L., White, J. S., Park, J. S., Schuller, J. A., Clemens, B. M. & Brongersma, M. L. Engineering light absorption in semiconductor nanowire devices. *Nature Materials* **8,** 643–647 (2009).

124. Wells, S. M., Merkulov, I. A., Kravchenko, I. I., Lavrik, N. V. & Sepaniak, M. J. Silicon nanopillars for field-enhanced surface spectroscopy. *ACS Nano* **6,** 2948–2959 (2012).

125. Zheng, X. & Zhang, L. Photonic nanostructures for solar energy conversion. *Energy and Environmental Science* **9,** 2511–2532 (2016).

126. Zhang, X., Li, X., Zhang, D., Su, N. Q., Yang, W., Everitt, H. O. & Liu, J. Product selectivity in plasmonic photocatalysis for carbon dioxide hydrogenation. *Nature Communications* **8** (2017).

127. Wang, P., Huang, B., Dai, Y. & Whangbo, M. H. Plasmonic photocatalysts: Harvesting visible light with noble metal nanoparticles. *Physical Chemistry Chemical Physics* **14,** 9813–9825 (2012).

128. Zhang, Z., Wang, Z., Cao, S. W. & Xue, C. Au/Pt nanoparticle-decorated TiO_2 nanofibers with plasmon-enhanced photocatalytic activities for solar-to-fuel conversion. *Journal of Physical Chemistry C* **117,** 25939–25947 (2013).

129. Lu, Y. C., Xu, Z., Gasteiger, H. A., Chen, S., Hamad-Schifferli, K. & Shao-Horn, Y. Platinum-gold nanoparticles: A highly active bifunctional electrocatalyst for rechargeable lithium-air batteries. *Journal of the American Chemical Society* **132,** 12170–12171 (2010).

130. Kim, H. J., Kearney, K. L., Le, L. H., Haber, Z. J., Rockett, A. A. & Rose, M. J. Charge-transfer through ultrathin film TiO_2 on n-Si(111) photoelectrodes: Experimental and theoretical investigation of electric field-enhanced transport with a nonaqueous redox couple. *Journal of Physical Chemistry C* **120,** 25697–25708 (2016).

131. Zhou, L., Zhang, C., McClain, M. J., Manjavacas, A., Krauter, C. M., Tian, S., Berg, F., Everitt, H. O., Carter, E. A., Nordlander, P. & Halas, N. J. Aluminum Nanocrystals as a Plasmonic Photocatalyst for Hydrogen Dissociation. *Nano Letters* **16,** 1478–1484 (2016).

132. Jiang, Z., Zhang, Z. Y., Shangguan, W., Isaacs, M. A., Durndell, L. J., Parlett, C. M. & Lee, A. F. Photodeposition as a facile route to tunable Pt photocatalysts for hydrogen production: On the role of methanol. *Catalysis Science and Technology* **6,** 81–88 (2016).

133. Zhong, Z., Ho, J., Teo, J., Shen, S. & Gedanken, A. Synthesis of porous α-Fe_2O_3 nanorods and deposition of very small gold particles in the pores for catalytic oxidation of CO. *Chemistry of Materials* **19,** 4776–4782 (2007).

134. Han, K. N., Li, C. A., Bui, M. P. N., Pham, X. H., Kim, B. S., Choa, Y. H. & Seong, G. H. Development of Pt/TiO_2 nanohybrids-modified SWCNT electrode for sensitive hydrogen peroxide detection. *Sensors and Actuators, B: Chemical* **174,** 406–413 (2012).

135. Li, R., Zhang, F., Wang, D., Yang, J., Li, M., Zhu, J., Zhou, X., Han, H. & Li, C. Spatial separation of photogenerated electrons and holes among {010} and {110} crystal facets of BiVO4. *Nature communications* **4,** 1432 (2013).

136. McDonald, K. J. & Choi, K. S. Photodeposition of co-based oxygen evolution catalysts on α-Fe_2O_3 photoanodes. *Chemistry of Materials* **23,** 1686–1693 (2011).

137. Zhong, D. K., Cornuz, M., Sivula, K., Grätzel, M. & Gamelin, D. R. Photo-assisted electrodeposition of cobalt-phosphate (Co-Pi) catalyst on hematite photoanodes for solar water oxidation. *Energy and Environmental Science* **4,** 1759–1764 (2011).

138. Taing, J., Cheng, M. H. & Hemminger, J. C. Photodeposition of Ag or Pt onto TiO_2 nanoparticles decorated on step edges of HOPG. *ACS Nano* **5,** 6325–6333 (2011).

139. Fernando, J. F., Shortell, M. P., Noble, C. J., Harmer, J. R., Jaatinen, E. A. & Waclawik, E. R. Controlling Au Photodeposition on Large ZnO Nanoparticles. *ACS Applied Materials and Interfaces* **8,** 14271–14283 (2016).

140. Dasog, M., Carim, A. I., Yalamanchili, S., Atwater, H. A. & Lewis, N. S. Profiling Photoinduced Carrier Generation in Semiconductor Microwire Arrays via Photoelectrochemical Metal Deposition. *Nano Letters* **16,** 5015–5021 (2016).

141. Krogstrup, P., Jørgensen, H. I., Heiss, M., Demichel, O., Holm, J. V., Aagesen, M., Nygard, J. & Fontcuberta I Morral, A. Single-nanowire solar cells beyond the Shockley-Queisser limit. *Nature Photonics* **7,** 306–310 (2013).

142. Schmitt, S. W., Sarau, G. & Christiansen, S. Observation of strongly enhanced photoluminescence from inverted cone-shaped silicon nanostuctures. *Scientific Reports* **5** (2015).

143. Coenen, T., Van De Groep, J. & Polman, A. Resonant modes of single silicon nanocavities excited by electron irradiation. *ACS Nano* **7,** 1689–1698 (2013).

144. Lin, C. & Povinelli, M. L. Optical absorption enhancement in silicon nanowire arrays with a large lattice constant for photovoltaic applications. *Optics Express* **17,** 19371 (2009).

145. Wang, Z. Y., Zhang, R. J., Wang, S. Y., Lu, M., Chen, X., Zheng, Y. X., Chen, L. Y., Ye, Z., Wang, C. Z. & Ho, K. M. Broadband optical absorption by tunable Mie resonances in silicon nanocone arrays. *Scientific Reports* **5** (2015).

146. Scheuermann, A. G., Prange, J. D., Gunji, M., Chidsey, C. E. & McIntyre, P. C. Effects of catalyst material and atomic layer deposited TiO_2 oxide thickness on the water oxidation performance of metal-insulator-silicon anodes. *Energy and Environmental Science* **6,** 2487–2496 (2013).

147. Shaner, M. R., Hu, S., Sun, K. & Lewis, N. S. Stabilization of Si microwire arrays for solar-driven H_2O oxidation to O_2(g) in 1.0 M KOH(aq) using conformal coatings of amorphous TiO_2. *Energy and Environmental Science* **8,** 203–207 (2015).

148. Hu, S., Shaner, M. R., Beardslee, J. A., Lichterman, M., Brunschwig, B. S. & Lewis, N. S. Amorphous TiO_2 coatings stabilize Si, GaAs, and GaP photoanodes for efficient water oxidation. *Science* **344,** 1005–1009 (2014).

149. Bezares, F. J., Long, J. P., Glembocki, O. J., Guo, J., Rendell, R. W., Kasica, R., Shirey, L., Owrutsky, J. C. & Caldwell, J. D. Mie resonance-enhanced light absorption in periodic silicon nanopillar arrays. *Optics Express* **21,** 27587 (2013).

150. Siefke, T., Kroker, S., Pfeiffer, K., Puffky, O., Dietrich, K., Franta, D., Ohlídal, I., Szeghalmi, A., Kley, E. B. & Tünnermann, A. Materials Pushing the Application Limits of Wire Grid Polarizers further into the Deep Ultraviolet Spectral Range. *Advanced Optical Materials* **4,** 1780–1786 (2016).

151. Lyon, L. A. & Hupp, J. T. Energetics of the nanocrystalline titanium dioxide/aqueous solution interface: Approximate conduction band edge variations between H0 = -10 and H- = +26. *Journal of Physical Chemistry B* **103,** 4623–4628 (1999).

152. Kohtani, S., Yoshida, K., Maekawa, T., Iwase, A., Kudo, A., Miyabe, H. & Nakagaki, R. Loading effects of silver oxides upon generation of reactive oxygen species in semiconductor photocatalysis. *Physical Chemistry Chemical Physics* **10,** 2986–2992 (2008).

153. Jiao, J., Wei, Y., Chi, K., Zhao, Z., Duan, A., Liu, J., Jiang, G., Wang, Y., Wang, X., Han, C. & Zheng, P. Platinum Nanoparticles Supported on TiO_2 Photonic Crystals as Highly Active Photocatalyst for the Reduction of CO_2 in the Presence of Water. *Energy Technology* **5,** 877–883 (2017).

154. Shuang, S., Lv, R., Xie, Z. & Zhang, Z. Surface plasmon enhanced photocatalysis of Au/Pt-decorated TiO_2 nanopillar arrays. *Scientific Reports* **6,** 26670 (2016).

155. Hodes, G. & Kamat, P. V. Understanding the Implication of Carrier Diffusion Length in Photovoltaic Cells. *Journal of Physical Chemistry Letters* **6,** 4090–4092 (2015).

156. Chi, J. Y. & Gatos, H. C. Determination of dopant-concentration diffusion length and lifetime variations in silicon by scanning electron microscopy. *Journal of Applied Physics* **50,** 3433–3440 (1979).

157. Linic, S., Aslam, U., Boerigter, C. & Morabito, M. Photochemical transformations on plasmonic metal nanoparticles. *Nature Materials* **14,** 567–576 (2015).

158. Marimuthu, A., Zhang, J. & Linic, S. Tuning Selectivity in Propylene Epoxidation by Plasmon Mediated. *Science* **339,** 1590–1593 (2013).

159. Quiroz, J., Barbosa, E. C., Araujo, T. P., Fiorio, J. L., Wang, Y. C., Zou, Y. C., Mou, T., Alves, T. V., De Oliveira, D. C., Wang, B., Haigh, S. J., Rossi, L. M. & Camargo, P. H. Controlling Reaction Selectivity over Hybrid Plasmonic Nanocatalysts. *Nano Letters* **18,** 7289–7297 (2018).

160. Christopher, P., Xin, H., Marimuthu, A. & Linic, S. Singular characteristics and unique chemical bond activation mechanisms of photocatalytic reactions on plasmonic nanostructures. *Nature Materials* **11,** 1044–1050 (2012).

161. Cortés, E., Xie, W., Cambiasso, J., Jermyn, A. S., Sundararaman, R., Narang, P., Schlücker, S. & Maier, S. A. Plasmonic hot electron transport drives nanolocalized chemistry. *Nature Communications* **8,** 14880 (2017).

162. Forcherio, G. T., Baker, D. R., Boltersdorf, J., Leff, A. C., McClure, J. P., Grew, K. N. & Lundgren, C. A. Targeted Deposition of Platinum onto Gold Nanorods by Plasmonic Hot Electrons. *Journal of Physical Chemistry C* **122,** 28901–28909 (2018).

163. Nguyen, V. Q., Ai, Y., Martin, P. & Lacroix, J. C. Plasmon-Induced Nanolocalized Reduction of Diazonium Salts. *ACS Omega* **2,** 1947–1955 (2017).

164. Schlather, A. E., Manjavacas, A., Lauchner, A., Marangoni, V. S., DeSantis, C. J., Nordlander, P. & Halas, N. J. Hot Hole Photoelectrochemistry on Au@SiO_2@Au Nanoparticles. *Journal of Physical Chemistry Letters* **8,** 2060–2067 (2017).

165. Wang, F., Wong, R. J., Ho, J. H., Jiang, Y. & Amal, R. Sensitization of Pt/TiO_2 Using Plasmonic Au Nanoparticles for Hydrogen Evolution under Visible-Light Irradiation. *ACS Applied Materials and Interfaces* **9,** 30575–30582 (2017).

166. Wan, D. Y., Zhao, Y. L., Cai, Y., Asmara, T. C., Huang, Z., Chen, J. Q., Hong, J., Yin, S. M., Nelson, C. T., Motapothula, M. R., Yan, B. X., Xiang, D., Chi, X., Zheng, H., Chen, W., Xu, R., Ariando, Rusydi, A., Minor, A. M., Breese, M. B., Sherburne, M., Asta, M., Xu, Q. H. & Venkatesan, T. Electron transport and visible light absorption in a plasmonic photocatalyst based on strontium niobate. *Nature Communications* **8** (2017).

167. Robatjazi, H., Bahauddin, S. M., Doiron, C. & Thomann, I. Direct Plasmon-Driven Photoelectrocatalysis. *Nano Letters* **15,** 6155–6161 (2015).

168. Mubeen, S., Lee, J., Singh, N., Krämer, S., Stucky, G. D. & Moskovits, M. An autonomous photosynthetic device in which all charge carriers derive from surface plasmons. *Nature Nanotechnology* **8,** 247–251 (2013).

169. Kumar, D., Lee, A., Lee, T., Lim, M. & Lim, D. K. Ultrafast and Efficient Transport of Hot Plasmonic Electrons by Graphene for Pt Free, Highly Efficient Visible-Light Responsive Photocatalyst. *Nano Letters* **16,** 1760–1767 (2016).

170. Ahmadi, T. S., Logunov, S. L. & El-Sayed, M. A. Picosecond dynamics of colloidal gold nanoparticles. *Journal of Physical Chemistry* **100,** 8053–8056 (1996).

171. Brongersma, M. L., Halas, N. J. & Nordlander, P. Plasmon-induced hot carrier science and technology. *Nature Nanotechnology* **10,** 25–34 (2015).

172. Valenti, M., Venugopal, A., Tordera, D., Jonsson, M. P., Biskos, G., Schmidt-Ott, A. & Smith, W. A. Hot Carrier Generation and Extraction of Plasmonic Alloy Nanoparticles. *ACS Photonics* **4,** 1146–1152 (2017).

173. Ma, X. C., Dai, Y., Yu, L. & Huang, B. B. Energy transfer in plasmonic photocatalytic composites. *Light: Science and Applications* **5,** e16017 (2016).

174. Giugni, A., Torre, B., Toma, A., Francardi, M., Malerba, M., Alabastri, A., Proietti Zaccaria, R., Stockman, M. I. & Di Fabrizio, E. Hot-electron nanoscopy using adiabatic compression of surface plasmons. *Nature Nanotechnology* **8,** 845–852 (2013).

175. Yu, Y., Ji, Z., Zu, S., Du, B., Kang, Y., Li, Z., Zhou, Z., Shi, K. & Fang, Z. Ultrafast Plasmonic Hot Electron Transfer in Au Nanoantenna/MoS_2 Heterostructures. *Advanced Functional Materials* **26,** 6394–6401 (2016).

176. Sousa-Castillo, A., Comesaña-Hermo, M., Rodríguez-González, B., Pérez-Lorenzo, M., Wang, Z., Kong, X. T., Govorov, A. O. & Correa-Duarte, M. A. Boosting Hot Electron-Driven Photocatalysis through Anisotropic Plasmonic Nanoparticles with Hot Spots in Au-TiO_2 Nanoarchitectures. *Journal of Physical Chemistry C* **120,** 11690–11699 (2016).

177. Wu, B., Liu, D., Mubeen, S., Chuong, T. T., Moskovits, M. & Stucky, G. D. Anisotropic Growth of TiO_2 onto Gold Nanorods for Plasmon-Enhanced Hydrogen Production from Water Reduction. *Journal of the American Chemical Society* **138,** 1114–1117 (2016).

178. Zheng, Z., Tachikawa, T. & Majima, T. Single-particle study of Pt-modified Au nanorods for plasmon-enhanced hydrogen generation in visible to near-infrared region. *Journal of the American Chemical Society* **136,** 6870–6873 (2014).

179. Ortiz, N., Zoellner, B., Hong, S. J., Ji, Y., Wang, T., Liu, Y., Maggard, P. A. & Wang, G. Harnessing Hot Electrons from Near IR Light for Hydrogen Production Using Pt-End-Capped-AuNRs. *ACS Applied Materials and Interfaces* **9,** 25962–25969 (2017).

180. Lee, Y. K., Lee, H., Lee, C., Hwang, E. & Park, J. Y. Hot-electron-based solar energy conversion with metal-semiconductor nanodiodes. *Journal of Physics Condensed Matter* **28,** 254006 (2016).

181. Macyk, W., Burgeth, G. & Kisch, H. Photoelectrochemical properties of platinum(IV) chloride surface modified TiO_2. *Photochemical and Photobiological Sciences* **2,** 322–328 (2003).

182. Lord, H. L., Zhan, W. & Pawliszyn, J. Fundamentals and applications of needle trap devices. A critical review. *Analytica Chimica Acta* **677,** 3–18 (2010).

183. Kong, X. T., Wang, Z. & Govorov, A. O. Plasmonic Nanostars with Hot Spots for Efficient Generation of Hot Electrons under Solar Illumination. *Advanced Optical Materials* **5,** 1–10 (2017).

184. Yu, Y., Wen, W., Qian, X. Y., Liu, J. B. & Wu, J. M. UV and visible light photocatalytic activity of Au/TiO_2 nanoforests with Anatase/Rutile phase junctions and controlled Au locations. *Scientific Reports* **7,** 41253 (2017).

185. Zilio, P., Dipalo, M., Tantussi, F., Messina, G. C. & De Angelis, F. Hot electrons in water: Injection and ponderomotive acceleration by means of plasmonic nanoelectrodes. *Light: Science and Applications* **6,** e17002 (2017).

186. Lee, H., Lee, H. & Park, J. Y. Direct Imaging of Surface Plasmon-Driven Hot Electron Flux on the Au Nanoprism/TiO_2. *Nano Letters* **19,** 891–896 (2019).

187. Yu, W., Porosoff, M. D. & Chen, J. G. Review of Pt-based bimetallic catalysis: From model surfaces to supported catalysts. *Chemical Reviews* **112,** 5780–5817 (2012).

188. Chanjuan Xi, Zhengshi Chen, Qinglin Li & Zhensheng Jin. Effects of H+, Cl- and CH_3COOH on the photocatalytic conversion of $PtCl_6^{2-}$ in aqueous TiO_2 dispersion. *Journal of Photochemistry and Photobiology, A: Chemistry* **87,** 249–255 (1995).

189. Radecka, M., Wierzbicka, M., Komornicki, S. & Rekas, M. Influence of Cr on photoelectrochemical properties of TiO_2 thin films. *Physica B: Condensed Matter* **348,** 160–168 (2004).

190. Kim, N. H., Meinhart, C. D. & Moskovits, M. Plasmon-Mediated Reduction of Aqueous Platinum Ions: The Competing Roles of Field Enhancement and Hot Charge Carriers. *Journal of Physical Chemistry C* **120,** 6750–6755 (2016).

191. Santiago, D., Rodríguez-Calero, G. G., Palkar, A., Barraza-Jimenez, D., Galvan, D. H., Casillas, G., Mayoral, A., Jose-Yacamán, M., Echegoyen, L. & Cabrera, C. R. Platinum electrodeposition on unsupported carbon nano-onions. *Langmuir* **28,** 17202–17210 (2012).

192. Scanlon, M. D., Peljo, P., Méndez, M. A., Smirnov, E. & Girault, H. H. Charging and discharging at the nanoscale: Fermi level equilibration of metallic nanoparticles. *Chemical Science* **6,** 2705–2720 (2015).

193. Liu, Y., Gokcen, D., Bertocci, U. & Moffat, T. P. Self-terminating growth of platinum films by electrochemical deposition. *Science* **338,** 1327–1330 (2012).

194. Djerdj, I. & Tonejc, A. M. Structural investigations of nanocrystalline TiO_2 samples. *Journal of Alloys and Compounds* **413,** 159–174 (2006).

195. Cushing, S. K. & Wu, N. Progress and Perspectives of Plasmon-Enhanced Solar Energy Conversion. *Journal of Physical Chemistry Letters* **7,** 666–675 (2016).

196. Leong, K. H., Aziz, A. A., Sim, L. C., Saravanan, P., Jang, M. & Bahnemann, D. Mechanistic insights into plasmonic photocatalysts in utilizing visible light. *Beilstein Journal of Nanotechnology* **9,** 628–648 (2018).

197. Cheng, H., Fuku, K., Kuwahara, Y., Mori, K. & Yamashita, H. Harnessing single-active plasmonic nanostructures for enhanced photocatalysis under visible light. *Journal of Materials Chemistry A* **3,** 5244–5258 (2015).

198. Linic, S., Christopher, P. & Ingram, D. B. Plasmonic-metal nanostructures for efficient conversion of solar to chemical energy. *Nature Materials* **10,** 911–921 (2011).

199. Schuller, J. A., Barnard, E. S., Cai, W., Jun, Y. C., White, J. S. & Brongersma, M. L. Plasmonics for extreme light concentration and manipulation. *Nature Materials* **9,** 193–204 (2010).

200. Govorov, A. O., Zhang, H., Demir, H. V. & Gun'Ko, Y. K. Photogeneration of hot plasmonic electrons with metal nanocrystals: Quantum description and potential applications. *Nano Today* **9,** 85–101 (2014).

201. Park, J. Y., Kim, S. M., Lee, H. & Nedrygailov, I. I. Hot-Electron-Mediated Surface Chemistry: Toward Electronic Control of Catalytic Activity. *Accounts of Chemical Research* **48,** 2475–2483 (2015).

202. Xiao, Q., Sarina, S., Waclawik, E. R., Jia, J., Chang, J., Riches, J. D., Wu, H., Zheng, Z. & Zhu, H. Alloying Gold with Copper Makes for a Highly Selective Visible-Light Photocatalyst for the Reduction of Nitroaromatics to Anilines. *ACS Catalysis* **6,** 1744–1753 (2016).

203. Kale, M. J., Avanesian, T., Xin, H., Yan, J. & Christopher, P. Controlling catalytic selectivity on metal nanoparticles by direct photoexcitation of adsorbate-metal bonds. *Nano Letters* **14,** 5405–5412 (2014).

204. Olsen, T. & Schiøtz, J. Origin of Power Laws for Reactions at Metal Surfaces Mediated by Hot Electrons. *Physical Review Letters* **103** (2009).

205. Qian, K., Sweeny, B. C., Johnston-Peck, A. C., Niu, W., Graham, J. O., Duchene, J. S., Qiu, J., Wang, Y. C., Engelhard, M. H., Su, D., Stach, E. A. & Wei, W. D. Surface plasmon-driven water reduction: Gold nanoparticle size matters. *Journal of the American Chemical Society* **136,** 9842–9845 (2014).

206. Hou, B., Shen, L., Shi, H., Kapadia, R. & Cronin, S. B. Hot electron-driven photocatalytic water splitting. *Physical Chemistry Chemical Physics* **19,** 2877–2881 (2017).

207. Mukherjee, S., Libisch, F., Large, N., Neumann, O., Brown, L. V., Cheng, J., Lassiter, J. B., Carter, E. A., Nordlander, P. & Halas, N. J. Hot electrons do the impossible: Plasmon-induced dissociation of H_2 on Au. *Nano Letters* **13,** 240–247 (2013).

208. Kim, S. M., Lee, S. J., Kim, S. H., Kwon, S., Yee, K. J., Song, H., Somorjai, G. A. & Park, J. Y. Hot carrier-driven catalytic reactions on Pt-CdSe-Pt nanodumbbells and Pt/GaN under light irradiation. *Nano Letters* **13,** 1352–1358 (2013).

209. Zhai, Y., DuChene, J. S., Wang, Y. C., Qiu, J., Johnston-Peck, A. C., You, B., Guo, W., Diciaccio, B., Qian, K., Zhao, E. W., Ooi, F., Hu, D., Su, D., Stach, E. A., Zhu, Z. & Wei, W. D. Polyvinylpyrrolidone-induced anisotropic growth of gold nanoprisms in plasmon-driven synthesis. *Nature Materials* **15,** 889–895 (2016).

210. Kontoleta, E., Askes, S. H. C. & Garnett, E. C. Self-Optimized Catalysts: Hot-Electron Driven Photosynthesis of Catalytic Photocathodes. *ACS Applied Materials & Interfaces,* acsami.9b10913 (2019).

211. Tatsuma, T., Nishi, H. & Ishida, T. Plasmon-induced charge separation: Chemistry and wide applications. *Chemical Science* **8,** 3325–3337 (2017).

212. Tanaka, A., Nakanishi, K., Hamada, R., Hashimoto, K. & Kominami, H. Simultaneous and stoichiometric water oxidation and Cr(VI) reduction in aqueous suspensions of functionalized plasmonic photocatalyst Au/TiO 2-Pt under irradiation of green light. *ACS Catalysis* **3,** 1886–1891 (2013).

213. Swearer, D. F., Zhao, H., Zhou, L., Zhang, C., Robatjazi, H., Martirez, J. M. P., Krauter, C. M., Yazdi, S., McClain, M. J., Ringe, E., Carter, E. A., Nordlander, P. & Halas, N. J. Heterometallic antenna-reactor complexes for photocatalysis. *Proceedings of the National Academy of Sciences of the United States of America* **113,** 8916–8920 (2016).

214. Aslam, U., Chavez, S. & Linic, S. Controlling energy flow in multimetallic nanostructures for plasmonic catalysis. *Nature Nanotechnology* **12,** 1000–1005 (2017).

215. Sambur, J. B., Chen, T. Y., Choudhary, E., Chen, G., Nissen, E. J., Thomas, E. M., Zou, N. & Chen, P. Sub-particle reaction and photocurrent mapping to optimize catalyst-modified photoanodes. *Nature* **530,** 77–80 (2016).

216. Zou, N., Chen, G., Mao, X., Shen, H., Choudhary, E., Zhou, X. & Chen, P. Imaging Catalytic Hotspots on Single Plasmonic Nanostructures via Correlated Super-Resolution and Electron Microscopy. *ACS Nano* **12,** 5570–5579 (2018).

217. Michaels, A. M., Jiang, J. & Brus, L. Ag Nanocrystal Junctions as the Site for Surface-Enhanced Raman Scattering of Single Rhodamine 6G Molecules. *Journal of Physical Chemistry B* **104,** 11965–11971 (2000).

218. Zhu, L., Lu, Q., Lv, L., Wang, Y., Hu, Y., Deng, Z., Lou, Z., Hou, Y. & Teng, F. Ligand-free rutile and anatase TiO 2 nanocrystals as electron extraction layers for high performance inverted polymer solar cells. *RSC Advances* **7,** 20084–20092 (2017).

219. Busch, M., Wang, R. B., Hellman, A., Rossmeisl, J. & Grönbeck, H. The Influence of Inert Ions on the Reactivity of Manganese Oxides. *Journal of Physical Chemistry C* **122,** 216–226 (2018).

220. Tian, Y., Shi, X., Lu, C., Wang, X. & Wang, S. Charge separation in solid-state gold nanoparticles-sensitized photovoltaic cell. *Electrochemistry Communications* **11,** 1603–1605 (2009).

221. Maeda, K. Z-scheme water splitting using two different semiconductor photocatalysts. *ACS Catalysis* **3,** 1486–1503 (2013).

222. Kumar, S. R., Hedhili, M. N., Alshareef, H. N. & Kasiviswanathan, S. Correlation of Mn charge state with the electrical resistivity of Mn doped indium tin oxide thin films. *Applied Physics Letters* **97,** 111909 (2010).

223. Ilton, E. S., Post, J. E., Heaney, P. J., Ling, F. T. & Kerisit, S. N. XPS determination of Mn oxidation states in Mn (hydr)oxides. *Applied Surface Science* **366,** 475–485 (2016).

224. Nesbitt, H. W. & Banerjee, D. Interpretation of XPS Mn(2p) spectra of Mn oxyhydroxides and constraints on the mechanism of MnO2 precipitation. *American Mineralogist* **83,** 305–315 (1998).

225. Zhang, F., Chen, J., Zhang, X., Gao, W., Jin, R., Guan, N. & Li, Y. Synthesis of titania-supported platinum catalyst: The effect of pH on morphology control and valence state during photodeposition. *Langmuir* **20,** 9329–9334 (2004).

226. Wang, S., Gao, Y., Miao, S., Liu, T., Mu, L., Li, R., Fan, F. & Li, C. Positioning the Water Oxidation Reaction Sites in Plasmonic Photocatalysts. *Journal of the American Chemical Society* **139,** 11771–11778 (2017).

227. Khurgin, J. B. How to deal with the loss in plasmonics and metamaterials. *Nature Nanotechnology* **10,** 2–6 (2015).

228. Weimer, A. W. Particle atomic layer deposition. *Journal of Nanoparticle Research* **21** (2019).

229. Koushik, D., Verhees, W. J., Kuang, Y., Veenstra, S., Zhang, D., Verheijen, M. A., Creatore, M. & Schropp, R. E. High-efficiency humidity-stable planar perovskite solar cells based on atomic layer architecture. *Energy and Environmental Science* **10,** 91–100 (2017).

230. Mann, S. A., Sciacca, B., Zhang, Y., Wang, J., Kontoleta, E., Liu, H. & Garnett, E. C. Integrating Sphere Microscopy for Direct Absorption Measurements of Single Nanostructures. *ACS Nano* **11,** 1412–1418 (2017).

231. Narang, P., Sundararaman, R. & Atwater, H. A. Plasmonic hot carrier dynamics in solid-state and chemical systems for energy conversion. *Nanophotonics* **5,** 96–111 (2016).

Summary

Light-matter interactions at the nanoscale have found great applications in photovoltaics and photocatalysis. Semiconductors and metals are two groups of materials where nanostructuring has opened new pathways in the development of light-matter interactions. Both of them have the ability to absorb light efficiently and confine it to very small volumes (hot-spots) through the appearance of optical resonances. Optical resonances of semiconductor and metal nanostructures as well as the location of the hot-spots are highly tunable with the geometry of the nanostructure and the nature of the material. These resonant nanomaterials can be used as platforms for localized generation of carriers, as the result of enhanced light absorption at the hot-spots. The photogenerated carriers can be used to drive chemical reactions at the nanoscale confined close to the hot-spots of the nanostructures. As a result, light can be used as a tool for the spatially controlled occurrence of chemical reactions. In this thesis, we fabricate and investigate how optical resonances of both semiconductor and metal nanostructures can be used for selective deposition of new nanomaterials at the hot-spots with the aim of designing hierarchical nanostructures which could play a role in photocatalysis.

In Chapter 2 we use optical resonances in silicon nanostructures and specifically in vertical nanowires to drive localized chemical reactions along their height. For this purpose, we fabricate three different vertical silicon nanostructures having control over their tapering angle, height and diameter. Numerical simulations are used to verify the optical resonances and the absorption profile along the height of the fabricated nanowires, nanocones and inverted nanocones. We show that indeed by changing the wavelength of the incident light or the tapering angle of the nanostructure we can tune the absorption profile of the nanostructures in the visible spectrum. We continue by using the three different nanostructures for driving a chemical reaction for the deposition of metallic Pt nanoparticles. After illumination of the silicon nanostructures in presence of a Pt precursor, we observe the deposition of metallic Pt attributing it to the injection and participation of the photogenerated electrons in the reduction of the Pt precursor. The

deposition sites of the Pt nanoparticles are then compared with the location of the absorption maxima per nanostructure, retrieved from the numerical simulations, and a fair correlation is found.

In Chapter 3 we turn our focus on driving localized chemical reactions with the optical resonances in plasmonic metal nanostructures. In this case the decay of the plasmons leads to the generation of hot-carriers, the lifetime of which is much shorter than excitons in semiconductors, which we use for selective deposition of Pt cocatalyst nanoparticles. For this purpose, we fabricate photoelectrodes with Au nano-islands coated with a thin TiO_2 layer, which promotes the charge separation of hot-carriers. We show that illumination of the nano-islands at their surface plasmon resonance results in the formation of Pt nanoparticles with a minimum applied bias. We verify that hot-electrons are responsible for the Pt deposition on the plasmonic nanostructrues and that they are able to change *in situ* the oxidation state of the material deposited. Then we compare the photocatalytic activity of photoelectrodes with hot-electron positioned Pt cocatalyst, with Au nano-islands with randomly electrodeposited Pt of the same morphology, amount and oxidation state. The results of the comparison show that localization of the cocatalyst on the plasmonic Au nano-islands by hot-electrons can increase the photocatalytic activity of the photoelectrodes compared to a random system. As a result, plasmonic photoelectrodes can self-optimize the location of the cocatalyst on their surface and position it exactly where the hot-electrons are generated and extracted to the electrolyte.

In chapter 4 we explore the deposition of more than one nanomaterial with both the hot-carriers generated in the same Au plasmonic nano-islands in a slightly different configuration than in Chapter 3. Now, instead of coating the plasmonic nanostructrues with a TiO_2 layer we fabricate them on top of it, in order to promote the extraction of hot-holes in the electrolyte. We first show that hot-holes can also drive a chemical reaction for deposition of a cocatalyst (MnO_x) through the oxidation of a manganese precursor without applying any bias. After that, the simultaneous deposition of more than one nanomaterial is investigated by combining two different precursors: a manganese and a platinum precursor. Indeed we show that illumination of Au nano-islands in presence of these two precursors results in deposition of a combination of Mn and Pt oxides. We attribute the formation of these nanomaterials to the hot-hole assisted oxidation of the Mn precursor and hot-electron reduction of the Pt precursor. The role of TiO_2 in these reactions is very crucial, since we believe that not only can it enhance the hot-carrier separation but also improve the binding of the precursors at the TiO_2/Au/electrolyte interface. We also investigate the spatial resolution of the hot-hole driven reaction on Au nanostructures (nanotriangles) with more confined hot-spots. Photodeposition of manganese oxides is repeated on the Au nanotriangles and the deposition sites are correlated with the simulated plasmonic hot-spots. We argue that the deposition sites of manganese oxides on these nanostructures can be controlled with an 80% fidelity.

Overall, our findings provide more insight in light-driven chemical reactions confined at the nanoscale, by using both semiconductor and metal nanostructures. The photosyn-

thesis of nanomaterials using optical resonances could lead to the design of complicated photocatalysts, where efficient charge separation can be achieved by the light-driven spatial formation and separation of cocatalyst materials.

Samenvatting

De interacties tussen licht en materie op de nanometerschaal bieden vele mogelijkheden voor toepassingen in de fotovoltaica en de fotokatalyse. Halfgeleiders en metalen zijn twee klassen materialen waarbij structurering op de nanoschaal heeft geleid tot nieuwe routes in de ontwikkeling van licht-materie interacties. Beiden hebben de mogelijkheid tot het efficiënt absorberen van het licht en het opsluiten ervan in hele kleine volumes (zogenaamde hotspots) door het ontstaan van optische resonanties in de nanostructuren. Zulke optische resonanties kunnen nauwkeurig worden afgestemd door het geometrische ontwerp van de structuur en materiaalkeuze. Deze resonante nanomaterialen kunnen gebruikt worden als platform voor de gelokaliseerde opwekking van ladingsdragers (elektronen en gaten), door de grote toename in de absorptie van licht in de resonantie-hotspots. Deze licht-gegeneerde ladingsdragers kunnen worden gebruikt voor het aandrijven van chemische reacties op de nanoschaal dichtbij de hotspots van de nanostructuur. Daardoor kan licht gebruikt worden als gereedschap om chemische reacties heel lokaal uit te voeren met grote precisie. In dit proefschrift fabriceren we halfgeleider en metalen nanostructuren en onderzoeken wij hoe de optische resonanties in beide structuren kunnen worden gebruikt voor de lokale synthese van een nieuw materiaal, selectief op de hotspots, met als doel het ontwerpen van geordende nanostructuren die gebruikt kunnen worden in fotokatalyse.

In Hoofdstuk 2 gebruiken we optische resonanties in rechtopstaande silicium nanostructuren om de gelokaliseerde chemische reacties aan te drijven langs de verticale as van de structuur. Hiervoor fabriceren we drie verschillende rechtopstaande silicium nanostructuren waarbij we de hoogte, diameter, en spitsheid variëren. Met numerieke simulaties identificeren we de optische resonanties en het absorptieprofiel langs de hoogte van de gefabriceerde nanodraden, nanokegels en omgekeerde nanokegels. Inderdaad laten we zien dat we door zowel de golflengte van het inkomende licht als de spitsheid van de structuur te variëren het absorptieprofiel van de nanostructuren kunnen aanpassen in het zichtbare spectrum. Vervolgens gebruiken we de drie verschillende nanostructuren

om de chemische reactie uit te voeren die leidt tot de afzetting van metallische platina nanodeeltjes. Na beschijning van de silicium nanostructuren in aanwezigheid van een platina precursor in water observeren we de afzetting van metallisch platina. Dit kennen we toe aan de injectie en deelname van de licht-gegeneerde elektronen aan de elektrochemische reductie van de platina precursor. Daarna vergelijken we de afzettingsplaatsen van de platina nanodeeltjes met de absorptiemaxima per nanostructuur die we verkregen uit de numerieke simulaties, en een redelijke correlatie tussen afzetting en absorptie werd gevonden.

In Hoofdstuk 3 verleggen we onze aandacht naar het aandrijven van gelokaliseerde chemische reacties met optische resonanties in metalen nanostructuren. In dit geval leidt het verval van aangeslagen plasmon-resonanties tot de opwekking van "hete" ladingsdragers, die een veel kortere levensduur hebben dan de aangeslagen ladingsdragers in halfgeleiders, en gebruiken deze voor de selectieve afzetting van platina nanodeeltjes als co-katalysator voor licht-aangedreven wateropsplitsing. Tevens laten we zien dat we hete elektronen kunnen gebruiken voor het veranderen van de oxidatietoestand van het platina. Hiervoor fabriceren we licht-elektrodes met gouden nano-eilandjes die bedekt zijn met een dunne TiO_2 laag, die de ladingscheiding van de hete ladingsdragers bewerkstelligt. We laten zien dat beschijning van de nano-eilandjes met licht dat hun resonantie effectief aanslaat resulteert in de afzetting van platina nanodeeltjes. Slechts een minimaal extern elektrisch veld is toegepast om de reactie enigszins te versnellen. Vervolgens vergelijken we de fotokatalytische activiteit van deze licht-elektrodes, die met hete elektronen zijn gefabriceerd, met die van licht-elektrodes die met enkel elektriciteit, zonder beschijning met licht, zijn gefabriceerd. Hierbij zijn de vorm, hoeveelheid, en oxidatietoestand van de platinadeeltjes in beide synthesemethodes zorgvuldig identiek gemaakt. De resultaten laten zien dat de gelokaliseerde afzetting van de co-katalysator door middel van hete elektronen de fotokatalytische activiteit kan verhogen ten opzichte van een systeem met een willekeurige plaatsing van de co-katalysator nanodeeltjes. Dit betekent dat de plasmonische licht-elektrodes zichzelf kunnen optimaliseren en de co-katalysator precies daar kunnen positioneren waar de hete elektronen gemaakt worden en gebruikt worden voor reductie-reacties in het elektrolyt.

In Hoofdstuk 4 verkennen we de afzetting van meer dan één nanomateriaal met behulp van beide hete ladingsdragers (elektronen én gaten) die worden gegenereerd in dezelfde gouden nano-eilandjes, maar in een andere ruimtelijke configuratie dan in Hoofdstuk 3. In plaats van de nano-eilandjes te bedekken met titaandioxide, fabriceren we nu de eilandjes bovenop de titaandioxide zodat beide ladingsdragers beschikbaar zijn voor chemische reacties in het elektrolyt. We laten eerst zien dat hete gaten kunnen worden gebruikt voor de afzetting van een co-katalysator materiaal (MnO_x) door de oxidatiereactie van een mangaan precursor zonder een extern voltage aan te brengen. Daarna onderzoeken we de gelijktijdige afzetting van twee materialen door twee chemische precursors te combineren in hetzelfde elektrolyt, namelijk een mangaan en een platina precursorzout. Inderdaad laten de resultaten zien dat beschijning van de gouden nano-eilandjes in aanwezigheid van beide precursorzouten leidt tot afzetting van een combinatie van Mn en

Pt oxides. We schrijven de synthese van deze oxides toe aan enerzijds de oxidatie van de Mn precursor door middel van hete gaten en de reductie van de Pt precursor door middel van hete elektronen. De rol van TiO_2 is zeer cruciaal in deze reacties, omdat het niet alleen zorgt voor ladingscheiding van hete gaten en elektronen, maar ook voor de binding van precursorzouten dichtbij het scheidingsvlak van TiO_2, Au en elektrolyt. We onderzoeken ook de ruimtelijke resolutie van de oxidatiereactie die door hete gaten wordt aangedreven in Au nanostructuren met meer gelokaliseerde hot-spots, zijnde Au nanodriehoeken. Licht-afzetting van mangaanoxides wordt herhaald op de nanodriehoeken en de afzettingslocaties worden gecorreleerd met de gesimuleerde plasmonische absorptie-hotspots. We betogen dat de afzettingslocaties van mangaanoxide op deze nanostructuren gecontroleerd kan worden met 80% betrouwbaarheid. Onze bevindingen verschaffen meer inzicht in de licht-aangedreven chemische reacties met behulp van optische resonanties in halfgeleider en metalen nanostructuren. Deze licht-synthese van nanomaterialen kan in de toekomst leiden tot het ontwerp van gecompliceerde fotokatalysatoren, waarbij efficiënte ladingscheiding kan worden gerealiseerd door de licht-gedreven ruimtelijke formatie en scheiding van co-katalysator materialen.

List of publications

This thesis is based on the following publications:

- *Localized photodeposition of catalysts using nanophotonic resonances in silicon photocathodes*, E. Kontoleta, S. H. C. Askes, L. Lai, E. C. Garnett, Beilstein J. Nanotechnol. **9**, 2097-2105 (2018). (**Chapter 2**)
- *Self-Optimized Catalysts: Hot-Electron Driven Photosynthesis of Catalytic Photocathodes*, E. Kontoleta, S. H. C. Askes, E. C. Garnett, ACS Appl. Mater. Interfaces **11**, 35713-35719 (2019). (**Chapter 3**)
- *Utilization of all hot-carriers in plasmonic nanostructures for selective deposition of nanomaterials*, E. Kontoleta, A. Tsoukala, S.H. C. Askes, E. Zoethout, H. Agrawal, E. C. Garnett., In preparation (2019). (**Chapter 4**)

Other publications by the author:

- *Over 70 % broadband integrated solar power in 1 μm Si cell with hyperuniform disorder nanostructuring*, N. Tavakoli, R. J. Spalding, G. Gkantzounis, C. Wan, Ruslan Röhrich, E. Kontoleta, M. Florescu, R. Sapienza, A. F. Koenderink, E. Alarcon-Llado, In preparation (2019).

- *Integrating Sphere Microscopy for Direct Absorption Measurements of Single Nanostructures*, S. A. Mann, B. Sciacca, Y. Zhang, J. Wang, E. Kontoleta, H. Liu, E. C. Garnett, ACS Nano **11** (2), 1412-1418, (2017).

- *The Role of Size and Dimerization of Decorating Plasmonic Silver Nanoparticles on the Photoelectrochemical Solar Water Splitting Performance of $BiVO_4$ Photoanodes*, M. Valenti, E. Kontoleta, I. Digdaya, M. P. Jonsson, G. Biskos, A. Schmidt-Ott, W. Smith, ChemNanoMat **2** (7), 739-747 (2016).

Acknowledgements

AMOLF is indeed a unique place to do science and I feel very lucky I had the chance to work here. I met brilliant scientists, who are very passionate with what they are doing but most importantly I met a lot of very nice people, who were always there to help and support each other. I would like to start with saying a big thank you to my supervisor Erik. I am very grateful you gave me the chance to do a PhD at AMOLF and to get to know you as a person. Working with you was always a learning path. You really taught me how to communicate better my thoughts and how not to be afraid to ask questions in front of all these "hardcore" physicists. I also feel very lucky that I met a person like you, who always wants to learn and improve himself, who is so open to criticism and admits when he has been wrong. I really appreciate the kindness, the support and understanding you showed when I was really disappointed with the progress of my PhD. You knew exactly what to say to make me keep going and through these years I feel that I became stronger through your supervision. I hope one day I can also be as good as you are in my job, have a beautiful family like yours and finish some 7a routes (or higher ?)! Thank you for everything.

I would like to thank all the group leaders of the Nanophotonics department of AMOLF, who were always showing interest in my research and giving useful feedback to move on further. I really learned a lot attending Nanophotonics colloquia, but also presenting my work there. They were the best practice for every conference. Thank you Erik, Albert, Bruno, Femius, Esther, Ewold and Said for organizing them, keeping the scientific level so high and most importantly for your down to earth attitude. It was also my pleasure meeting Andrea Baldi, who I consider as an amazing researcher, great person and very fun to work with. I will be waiting to see you, Valentina and Lorenzo at the restaurant of my parents one day! Thank you Andrea for all the nice and fun discussions. I really enjoyed the AMOLF-DIFFER meetings and they would not be the same without the Italian gang of DIFFER; Matteo and Ruben (you are also Italian, I think it's time to accept it), Rifat and Gayatri. I had a lot of fun with all of you guys!

Ciaaao and betalen! I also owe a big thanks to Wilson Smith, the person who introduced me to AMOLF and with whom I feel I have a great connection and discussions every time we meet.

The next person I want to thank is my actual second supervisor, "my" postdoc and most of all my friend and paranymph, Sven. Collega, I am very happy you came to the group and to my life! I hope you find me less chaotic by now (I know I am still a chaos but a bit less maybe?) and a better scientist. You are an excellent scientist and an amazing person. You were always supporting me and listening to my complaints and making me feel better. I will also miss our fights in the lab around stupid things that in the end we were agreeing on. Thank you for everything, I am sure you will have a very successful career and I wish you all the best in and out of the lab. I hope at some point I will come to visit your own lab to make sure your students understand how lucky they are. PS. I am very proud of you that you learned some very important Greek phrases!

I would also like to thank my group, Nanoscale Solar Cells, for all the fun lunches, the interesting political (or not) discussions/arguments and their help in and out of the lab. Thank you Eitan (for the Israeli temperament you added in the group), Julia (for motivating me act greener and translating/correcting my thesis summary), Harshal (for our great trip in Sicily), Biplab (for being yourself at any circumstance), Jian-Yao (for your relentless need for learning) and Hong-Yu (for your strong life decisions and the independent mentality). I want also to thank the ex-NSC group members: Sander, Parisa, Lai-Hung, Sebastian, Beniamino, Sarah, Gede and Eric who had the patience to transfer some of their knowledge to me and also share some more personal moments with me. Special thanks to Marc, who is the best technician our group could have ever wished for! Thank you for all the hard work and that you are always there to fix problems, which for us do not seem trivial at all.

I would like to say a huge thank you to all my friends at AMOLF and also the ones I met through AMOLF. Sander! I extremely admire your intelligence and the fact that you are not afraid to open up to me. Thank you for all your support and all the moments that you made me believe I was not doing everything wrong. Parisita, my persian friend! I think my first really good day at AMOLF was when you asked me to share an office. Thank you for bringing me to your beautiful country, for meeting your amazing family, for giving me a hug when I needed it, for working together at 12 at night listening to danceable music in the lab, for being there as a friend, for your great temperament and the genuine interest you show to people. My pleasure meeting you and still having you around. Ela mbare! it's your turn. My dear Giorgio, friend and paranymph, thank you for sharing thoughts for our life problems and concerns and for all the laughable moments you gave me. Your support especially during the writing of my thesis was extremely valuable. You managed to pump me up when I was down, to feel I was working for a reason and even solve few electrical problems of my experimental setup. You are very creative, smart, hard-working, an amazing person and I am sure your unique business plans will become a reality one day. I am looking forward to that. Javi! I only know you for almost a year but it was enough to understand what a great person you are and how

supportive you can be. Thank you for completing this amazing Mediterranean office. I wish you every success, which is undoubtable since you are super smart, dedicated and most of all a lovely person. I want also to thank Amy, for giving a scent of an order to our south office and making the best brownies and tacos. Lai-Hung, I also owe you a big thank you! I learned a lot from you, we faced a lot of difficulties in the lab together in the beginning of my PhD and I still remember the amazing dumplings you made for us. I hope you are happy to whatever you are doing. Agustin, you are considered as our 4th officemate, your treatment made many of my days at the office and I will miss all the special conversations we had. Andrea and Bruna thank you also for your contributions to our office, I loved all the Central and South American delicacies you were sending and the supporting notes you were leaving behind!

Agata you are an inspiration! I wish I can be as strong as you are and manage to deal with work so calmly as you do. I love your humor, your excitement about weapons and your efficiency on doing things putting always your (mental) health first! I believe there will be no obstacle between you and any goal you set and even if a poor obstacle appear I am sure you know how to vanish it. Great pleasure meeting you our colonel. My dear Cristina! You were the first person that included me in outside-AMOLF activities and I still remember how happy I was when I was going to your first house party. Thank you for listening to me and for giving me the opportunity to get to know you and realizing what a beautiful person you are in and out. I am impressed by how you face things with grace and charm and I am sure you will find the way in life to spread your magic. Alexandra mou, you were my favorite MSc student (even if you were the only one). Thank you for your hard work, for cheering me up, for some very Greek moments in the lab, for the awkwardness you spread around you (which I love) and for the very interesting conversions (you know which).

Ragazzi! Guuuuuys, AMOLF and Amsterdam life wouldn't be the same without you. MicheleMonti, my dear friend, I cannot thank you enough for all the laughter you gave me, for the poems that everytime I was receiving them I was risking my spot at AMOLF, for the moments like the "Jungle", for Freyr, for Levankade nights, for swimming coast to coast with an outside temperature of 10 °C and for the marciume in the "too perfect" Amsterdam. Be always this amazing yourself and be proud of it because it is great. Copo Solari, your life we all know was and is a safari. My friend, thank you for the sincere hugs, for the great music I listened to you playing, for the incredible stay in Tuscany when the Cottoleti met the Solaris (madooonna this could be a title for a movie), for all the "useful" Italian phrases, for being there whenever I was freaking out. I want also to thank TittaMarghetitta (ciiiiiiaaaooo) and TomassoTarquinious. My dear Titta thank you for all the amazing moments we shared, for your incredible cooking skills, for putting me back on track, for being the best tour guide in my favorite city in the world (Roma!) and for your sarcasm that it made me wish I knew how to speak Roman. Tark you are one of the sweetest people I know and you have the gift of making people feel comfortable. I am also still amazed that my whole village is still talking about you and your Greek dancing skills. Francesca (Fralaaav) you are the most powerful person

I know, you are a fighter and your positive attitude is out of this planet! I admire you for many things but mostly for how light you can make people (and me) feel and your kindness! Thank you for being an amazing friend. Diego, I am always surprised with how many things you can be great at! You are a person that does not afraid of trying new things and manages to become a proficient in them. You will always motivate me doing my best and being strong and lovable as you are. Flore, you are Greek my Dutch friend and you don't know it yet. Thanks for all the nice time we spent, listening to amazing music, dance on it and sharing our thoughts and concerns. Barto! What a person, what an energy and what an amazing time we had in San Diego with Jessie Lippert. Shanti it was always fun to have you around adding some freshness in the group and the Levantkade family. Giovanni, I am happy for the sapila you brought at AMOLF and for all the funny and angry moments we shared.

Lucie, uh lala! What a situatie you make around you my dear French friend with the not so French accent! Thank you for being so sweet, happy, optimistic and being such an honest and sincere person. I am sure that you will make a difference to whatever you decide to do. Susan, you are my other favorite mevrouw around here and I am very happy I have met such a strong (slightly softer after the interaction with me and Lucie), smart, kind and incredible person like you. Thank you also for all the sugary stuff you were feeding me, increasing the level of happiness around. Chris and Rob thank you for our recent but great climbing/sauna sessions and the diluted German wine! Christian thanks for your calm personality handling 3 southern ladies in the Arizona trip and the great music in the lab! Loreta/Lady, thanks for the fun moments and your impressive GoPro photography skills. Hans thank you for being so sweet with me and even giving me some more strength. Thank you also for initiating the AmolfJam sessions, where I had great moments and managed to get my head out of work. Mark, Christian, Jose, Julia, Weiyi, Ben, Cesare and Stivell, it was my pleasure "making" some music together and thanks for handling and not judging my poor music skills. My dear Nick, I am glad I met you and I shared with you some very interesting conversations. I find your excitement about science impressive and I was always learning something new from you. Tom, even if we never managed to start these dance lessons, I am happy that we spend some very nice time together and that I found out more about you. Lukas, you are a very generous person and I am always impressed by your cooking and carpentry skills and the fact that you really know how to make a place special and cozy. I am glad I met you! Lorenzo, Ale, Marco, Nicola and Mario you made every party special and you made sure that I will learn all the Italian and Hispanic songs, even if I wish sometimes you did not. Thank you guys for dancing with me, enjoying some very funny moments and bringing a more "relaxing" air around. Isabelle, you are great, very sweet and I am amazed by your dancing skills and unique medieval activities. Keep on being yourself. Marco (Valenti), you are the person that you passion about science made me choose to do a PhD. I want you to know that I do not regret it and I thank you for that. Roberto, you were always bringing the nice Mexican spirit at work and by doing this you were making the cactus feel a bit less painful. Thanks chiquitin! Federica, thank you for

understanding me and sharing some serious (or not) personal experiences with me. You are the calm power around here and you made me feel great, especially during our yearly romantic dinners. Gulia, my dear, thank you for the hearts on the window! I hope I will be around to pay you back when you will need it.

There were many more people at AMOLF and ARCNL that I interacted with, laughed with, had a drink, shared a dance, talked about different things, helped me (experimentally) and in general people who made my mood. So, thanks Andrea (for explaining Temptation Island in Italian, together with Loreta, and understanding my work through related references), Carolyn (for being a great neighbor and great example of a strong person, who doesn't give up), Kevin (for the hugs in the corridor, the writing support and the Bordeaux wine festival), Moritz (for the example you give as a great and calm scientist and a very sweet person), John (for the long Irish talks), Stephen (for the incredible person you are and for not complaining about my noisy room), Olga (for showing me that getting a PhD and being a mother is possible!), Nasim (for the fun moments we spend in the dark optical lab and the time I spend with Luna), Alexander I and Alexander II (for the Eastern European metal songs you made me listen to), Iarik (for sharing our common concerns for few things and keeping me strong, priviet Iaroslav), Stefan (for the interesting discussions and your SCIL skills), Marloes (for our disco moves at the stairs, the amazing tea and for being a sweetheart), Clyde (for the power you have and give to AMOLF), Wiebe (for all the Caribbean memories you shared with me), Grace (for your grace and the kindness you showed me) and Marko Kamp (for the sweet person you are and that you could always make my mood). Tom Brouwer, Wessel, Bob, Dimitry, Andries, Hans (Zeijlemaker), Jan (van der Linden), Mark (Willemse) and Niels (Winkelaar) thanks for helping me out doing my research and making the mechanical workshop and the NanoLab the places anyone would love to work at. Jan (Zomerdijk), your help and your interest in my electrical measurements/problems was indeed priceless! Reinout thank you for your technical assistance with the XPS. Ad and Juliette thanks for making my day, from the beginning of it. Linda thanks for all the help, I really enjoyed talking to you and sharing few thoughts. I also feel lucky that I met so many nice people who contributing to a great working environment. Thanks for that Verena, Simone, Bela, Wim, Jesse, Jente, Rene, Vanessa, Zoi, Lucas, Hugo, Juha, Jorick, Joris, Falco, Silvia, Fotis, Arno, Dominique, Eliane, Henk-Jan, Annemarie, Ruslan, Hinco, Benjamin, Benjamin B., Magda, Robin, Matthias, Sevda, Danai, Kelly, Florian, Mathijs, Nikhil and John.

During my stay in Amsterdam I met several people who contributed on bringing some sun in the cloudy Dutch days. I want to say a big thank you for that to: Steven, Bertus, Fabian, Ben, PepeFederico, Honey, Andrea T., Sunil, Taraneh, Giota, Abel, Mauro and Paul. I want also to thank Karin for the amazing music lessons and all our chats on music and life.

Next, I would like to thank my "Delft" friends, Timi, Teresa, Ifigeneia, Niko, Taso, Adwait, Yash, Rucheet, Punit and Eas. You are my extended family abroad, you made me feel like home, you travelled with me around the world and every time I see you I

feel 100% myself. Billy, it's nice that life made us follow similar paths and I still have you around! Marina, Eftihia and Elli, thank you for many lovely and funny moments. Tommaso, I always enjoy our deep conversations about human behaviors. Bartek and Eline, I really appreciate the support you have showed me.

My friends back in Greece are a big part of me. I wouldn't be here if they hadn't set the level so high as people, giving me motivation to become a better person and always aim for bigger things in my life. Afroditi, Niko, Vasili, Louka, Polina, Konstantina, Loreta, Eirini and Evgenia, I really appreciate your support all these years and I love the craziness you carry and transmit every time we meet.

Last but definitely not least I owe a huge thank you to my family. There are no other people in my life that I admire and I am proud of more than my parents. They are the most hardworking people I have ever met, they are smart, kind and always next to me. Μπαμπά και μαμά θέλω να σας ευχαριστήσω για όλα όσα έχετε κάνει για μένα, για όλη τη στήριξη και την εμπιστοσύνη που μου δείχνετε, για το ότι πάντα θα πείτε τη γνώμη σας χωρίς να κατακρίνετε την τελική επιλογή μου. I want also to thank my brother Dimitris, who is always there for me, who makes me laugh, who I admire for his strength, his amazing kindness and for being always himself without being ashamed of that. Ευχαριστώ μικρέ που είσαι πάντα εκεί όταν σε χρειάζομαι! I want also to thank the new member of our family my sister in law Eleni, my partner in crime when dancing is on (together with my grandma). Ελενάκι σε ευχαριστώ που αγαπάς τον αδερφό μου, που είσαι στήριγμα δικό του αλλά και δικό μου και που κρατάς της ισορροπίες στην τρελό-φαμίλια μας. Tzaneto thank you for the inspiration behind my cover, I loved it! I want also to thank my aunt and my uncle, Lia and Manos, and my cousins, Eirini and Alexandros, for all the support and the fun they are adding to the family. I also owe a huge thank you to the people that they actually raised me, my grandparents! Γιαγιά Ακριβή, παππού Αλέξη, γιαγιά Τζένη και παππού Δημήτρη σας ευχαριστώ για όλα και ελπίζω κάποια στιγμή να μπορώ να γυρίσω πίσω και να πω ότι αγωνίστηκα όσο και εσείς στη ζωή μου και τα κατάφερα!